University of São Paulo

The Institute of Astronomy, Geophysics and Atmospheric Sciences

Department of Atmospheric Sciences

Vannia Jaqueline Aliaga Nestares

# LORENZ ENERGETIC APPLIED TO UNDERSTANDING OF SQUALL LINES PROPAGATION OVER THE AMAZON BASIN

(ENERGÉTICA DE LORENZ APLICADA AO ENTENDIMENTO DA PROPAGAÇÃO DE LINHAS DE INSTABILIDADE NA AMAZÔNIA)

São Paulo

2017

Vannia Jaqueline Aliaga Nestares

# LORENZ ENERGETIC APPLIED TO UNDERSTANDING OF SQUALL LINES PROPAGATION OVER THE AMAZON BASIN

## (ENERGÉTICA DE LORENZ APLICADA AO ENTENDIMENTO DA PROPAGAÇÃO DE LINHAS DE INSTABILIDADE NA AMAZÔNIA)

Dissertation presented at the Institute of Astronomy, Geophysics and Atmospheric Sciences at the University of São Paulo as a partial requirement for obtaining the title of Master of Sciences.

Area of Concentration: Meteorology

Advisor: PhD. Rosmeri Porfirio da Rocha

"Corrected version. The original is available at the Unity"

São Paulo

2017

*To my mother and grandmother, who I love.*

*To my grandfather, who I know you takes care of me from above.*

## ACKNOWLEDGMENTS

In the emotional, the most important part for the development of this work, I thank to:

- Diego, this time was better with his company and daily support. He helped me a lot.

- To my mother, for her unconditional support and to my family and extended family, for their constant concern despite the distance.

- My friends at the student residence Afrânio 180, mainly Mario, Ana Maria, Daniela, Yuugo, Franky, Fernanda, Yui, Mei, Kana, Marcos, Yeny and Valeria, sharing meals and laughs with you made us feel like siblings.

- To Dona Claudia, for being like a mother.

- To Cristina and Eleazar, for their support at the beginning of my journey at Brazil.

# ABSTRACT

Squall lines (SL) represent an important precipitation system in the Amazon basin, especially during the dry season. To improve the understanding and forecasting of these SL, the main objective of this work was, through the Lorenz Energetic Cycle (LEC) to evaluate the mechanisms favoring the propagation of SL, or not. For this, the LEC was analyzed in two SL episodes. The analyses of Global Forecast System (GFS) model, with 0.5° of horizontal grid, were used for synoptic analysis and calculation of Lorenz energetic in the quasi-Lagrangian and Eulerian approaches. Between April and August 2014 and 2015 were identified 21 episodes of SL using GOES-13 imagery in the infrared channel. These episodes were classified as Coastal Squall Lines (CSL), when the SL has remained near to South America's (SA) coast and moved less than 10° westward from the start point, and Amazonian Squall Lines (ASL), when the SL originated over northern coast of SA and propagated over the Amazon basin (more of 10°). The mean features of these CSL and ASL were, respectively, 12 and 18 ms$^{-1}$ of propagation speed, 15 and 23 hours of lifetime, 630 and 1400 km of inland propagation, 175 and 250 km of width, 1450 and 1980 km of length. The majority of them started between 15:00 and 18:00 UTC.

In the synoptic analysis, at upper levels were observed two anticyclonic systems configuring more intense winds over ASL than in CSL, thus favoring the westward displacement of ASL. At 850 hPa, the wind and moisture convergence were more intense in ASL than in CSL. The vertical profiles of wind showed a low-level jet during the formation of the SL and displacement the ASL over the Amazon. It was also observed: the occurrence of vertical wind speed shear at low-levels during the ASL and vertical directional shear at upper levels during CSL, contributing to inhibit their westward movement.

In energetic terms, it was obtained larger intensity of the zonal kinetic energy term ($K_Z$) compared to the other terms of the LEC and the values were higher in ASL than in CSL. The second most intense term was the eddy kinetic energy ($K_E$), which increased during the squall lines occurrence, with higher values in ASL (in all the troposphere) than in CSL (only above 500 hPa). The baroclinic term prevailed in all troposphere during the ASL occurrence, while in CSL it was active only in 200-400 hPa layer. The barotropic term reached values similar of the baroclinic term, emphasizing the importance of this term in Amazon SLs. The boundary energy fluxes had higher values in ASL than in CSL. Due to the predominance of kinetic energy rather than available potential in both events, the equation of local change in kinetic energy for a fixed volume was used. It was obtained greater and positive values of kinetic energy in ASL than in CSL (as with the terms of LEC) resulted from the horizontal flux divergence term.

**Key Words:** Lorenz Energy Cycle, Amazon squall lines, GFS analysis.

# RESUMO

As linhas de instabilidade (LI) representam um importante sistema de precipitação na Amazônia, principalmente durante a estação seca. Buscando melhorar o entendimento e a previsão deste tipo de sistema, o objetivo deste estudo foi através do ciclo de energia de Lorenz avaliar os mecanismos que favorecem ou não a propagação das LI. Para tanto, o ciclo de energia de Lorenz foi analisado em dois episódios de LI. As análises de *Global Forecast System* (GFS), com resolução horizontal de 0.5°, foram utilizadas para análise sinótica e cálculo de energia de Lorenz usando os esquemas quase-Lagrangiano e Euleriano. Entre Abril e Agosto de 2014 e 2015 se identificaram 21 episódios de LI usando imagens do canal infra-vermelho do GOES-13. Estes episódios foram classificados em LI Costeira (LIC), quando permanecem perto da costa do América do Sul (AS) deslocando-se menos de 10° para o oeste, e LI Amazônica (LIA), se originam na costa de AS e se propagam pela Amazônia (mais de 10°). As características médias das LIC e LIA foram, respectivamente, 12 e 18 m s$^{-1}$ de velocidade de propagação, 15 e 23 horas de tempo de vida, 630 e 1400 km de distância percorrida para oeste, 175 e 250 km de largura, 1450 e 1980 km de comprimento. A maioria das LI iniciaram entre 15:00 e 18:00 UTC.

Na análise sinótica, dois sistemas anticiclônicos em altos níveis configuraram ventos mais intensos durante a LIA que LIC, favorecendo assim o deslocamento para o oeste da LIA. Em 850 hPa, a convergência do fluxo de umidade e os ventos foram mais intensos na LIA do que na LIC. Os perfis verticais de vento mostraram a presença de um jato de baixos níveis durante a formação das linhas e também durante o deslocamento pela Amazônia da LIA. Foi observado ainda a ocorrência de cisalhamento vertical de velocidade em níveis baixos durante a LIA e de cisalhamento direcional em níveis altos durante a LIC, contribuindo para inibir seu movimento para o oeste.

Em termos energéticos, obteve-se maior intensidade do termo de energia cinética zonal ($K_Z$) comparado com os outros termos da energética e com valores superiores durante a LIA do que a LIC. O segundo termo de maior intensidade foi o da energia cinética dos distúrbios ($K_E$) que aumentou durante a ocorrência dos dois eventos, com valores maiores na LIA (em toda troposfera) que na LIC (apenas acima de 500 hPa). O termo baroclínico atuou em todas as camadas troposféricas durante a LIA, enquanto que durante a LIC esteve ativo na camada de 200-400 hPa. O termo barotrópico apresentou valores similares aos do termo baroclínico, indicando também sua importância para as LI na Amazônia. Valores maiores do fluxo de energia pelas fronteiras foram observados na LIA do que na LIC. Devido à predominância da energia cinética em ambos os eventos, utilizou-se equação de balanço de energia cinética num volume fixo. Basicamente, os valores positivos e maiores de energia cinética (como também obtido para os termos do ciclo de energia de Lorenz) na LIA que na LIC resultaram principalmente do termo de divergência do fluxo horizontal da energia cinética.

**Palavras Chave:** Energética de Lorenz, linhas de instabilidade amazônicas, análises de GFS.

# CONTENTS

# LIST OF FIGURES

# LIST OF TABLES

# 1. CHAPTER 1: INTRODUCTION

## 1.1. INITIAL CONSIDERATIONS

The Amazon squall lines (SLs) are a very important precipitation system for the Amazon basin. According to Greco et al. (1990) four squall line events were responsible for at least 38% of the total precipitation over the central part of Amazon basin during April 1 and May 14 1987 (period of Amazon Boundary Layer Experiment – ABLE 2B).

There are several investigations about this SL type, mainly about its structure, wind profiles during the formation and displacement, synoptic conditions, and some investigations regarding the heat and moisture budgets during SL. However, there are no studies related to the energetic of Amazon SLs.

In the present work, the Lorenz Energy Cycle (LEC) is used to understand the energy terms of the synoptic environment favoring or not the inland displacement of Amazon SL, which are initially develop over northeastern coast of South America.

The forecast of the formation and propagation of Amazon SL is a complicated task because these systems have mesoescale dimensions and they are not very well represented by operational numerical models due both little observational data availability in the Amazon basin and coarse resolution. However, since SL contributes to the precipitation in the Amazon basin, mainly during dry season, its forecasting is a crucial task.

In that sense, the knowledge and characterization of the energy contained in the SL will be applied as a tool in the forecast of their propagation. Thus, to anticipate whether the SL formed in northeastern coast of South America will remain near the coast or propagate toward the center of the Amazon basin and, in several cases, if it will reach the westernmost side of the Amazon (Peruvian Amazon).

## 1.2. OBJECTIVES

The principal objective in this study is to evaluate the related mechanisms of the synoptic environments favoring or not the propagation of SL over the Amazonia using the

Lorenz energy cycle.

The specific objectives are to:

- Classify as CSL or ASL the SLs occurred during the dry season of 2014-2015;

- Characterize the energetic of two SL events, contributing thus to their prediction;

- Describe the synoptic conditions during the occurrence of these two SL events;

- Calculate and analyze the terms of the kinetic energy and thermodynamic budgets in the two SL events.

# 2. CHAPTER 2: LITERATURE REVIEW

## 2.1. SQUALL LINES

Following the Glossary of Meteorology (2016), a SL is a line of active deep moist convection frequently associated with thunders, either continuous or with breaks, including contiguous precipitation areas. SLs are classified as a type of mesoescale convective system distinguished from other types by a larger length-to-width ratio.

Following Asnani (2005), a SL is a line of strong winds resulting from the downdraft emanating from a line of thunderclouds. Generally, a SL is associated with some low-pressure system of synoptic scale and can have several hundred kilometers long. Each of the thunderclouds contains one or more cells that follow the life-cycle common in thunderstorms. The width of a SL has the size of an individual thunderstorm.

### 2.1.1. CHARACTERISTICS

The conceptual characteristics of SLs structure are summarized in the next figure made by Markowski and Richardson (2010):
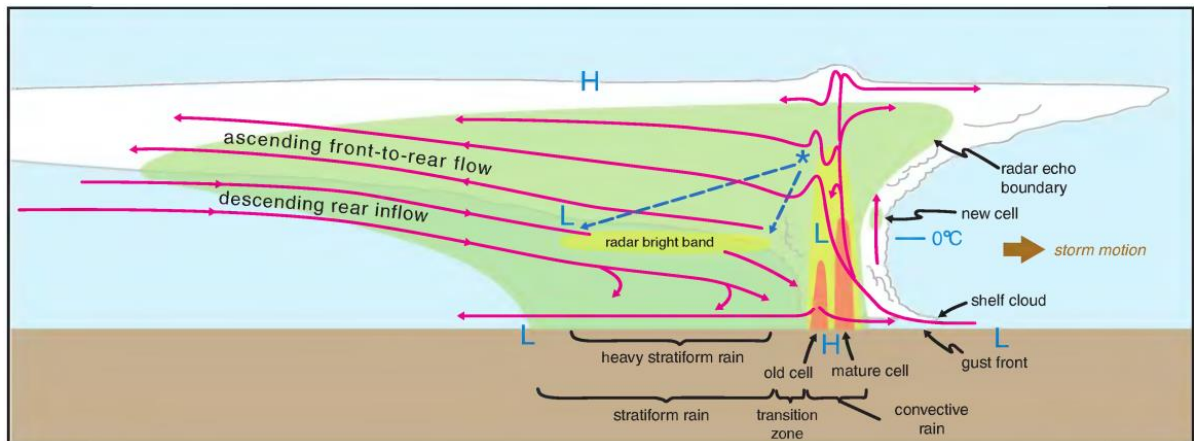


Figure 2.1 - Conceptual model of a SL with trailing stratiform area viewed in a vertical cross-section oriented perpendicular to the convective line. The green shading indicates the region of precipitation-sized hydrometeors. The yellow and orange shading indicates more intense radar echoes. Pressure maxima and minima are also indicated (with H and L letters), as is the height of the melting level, which is located just above the height at which a radar bright band is observed (Source: adapted from Houze et al. (1989) by Markowski and Richardson (2010)).

According to Markowski and Richardson (2010), in the Figure 2.1. the most convective area in the SL is confined to the leading edge of the system, and a second region, associated with a trailing stratiform precipitation, is greater and commonly located at the rear of the convective cells. Naturally, SLs are normal oriented to the low-level shear and hydrometeors are deposited at the rear by a front-to-rear flow through the system. The front flow is forced to lift to the level of free convection (LFC) by the gust front, and descends a little behind the leading convection region before entering completely to the *trailing stratiform* region, when there is a slight rise again and it is associated with upward vertical velocities generally less than 0.5 m s$^{-1}$. It is below of the ascending front-to-rear flow that the stratiform rain occurs.

Although the majority (60-80%) of SLs organization implies in the stratiform region located at the rear of the line, there are other types of SLs configuration. In such cases, the precipitation may not fall at the rear of the leading region. Two other cases were described. In one of them, the deep-layer shear has a strong rear-to-front component and the hydrometeors fall ahead of the convective towers, or into a *leading stratiform* region. In the other, the deep-layer shear has a strong along-line component and the hydrometeors precipitate parallel to the orientation of the updrafts, or into a *parallel stratiform* region (Markowski and Richardson, 2010). Figure 2.2 provides the visualization of these types of organization of SLs according to Parker and Johnson (2000).
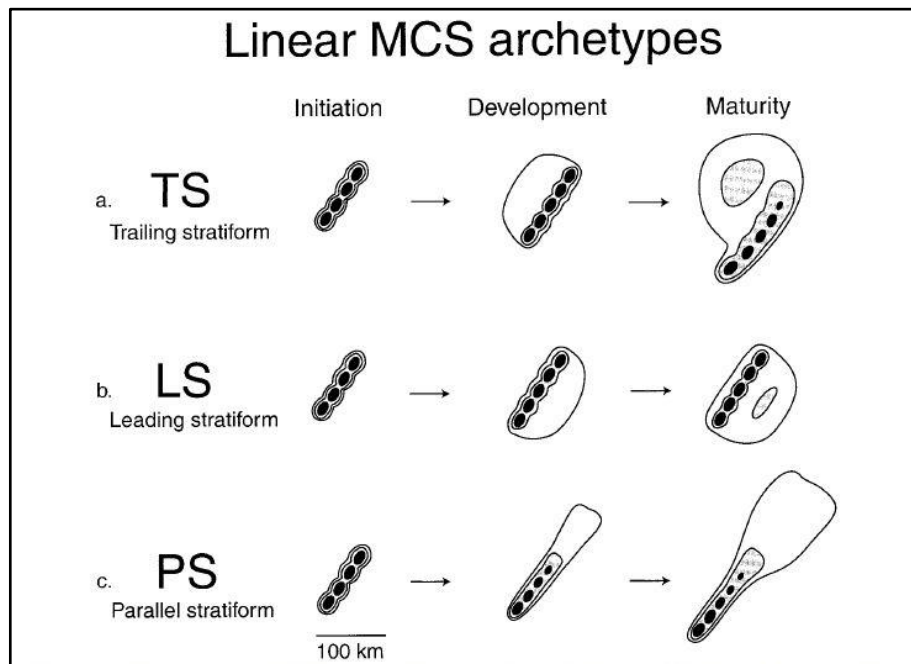


Figure 2.2 - Schematic reflectivity drawing of idealized life cycles for three linear MCS archetypes. Approximate time intervals between phases: for TS 3-4 h; for LS 2-3 h; for PS 2-3 h. Levels of color shading roughly correspond to 20, 40, and 50dBZ (Source: Parker and Johnson, 2000).

SL is also known as pressure-jump line because when the line is crossing an area there is a pressure increase, and after that there is a pressure decrease (Asnani, 2005). In the Figure 2.3 can be observed a profile of a pressure disturbance for a SL.
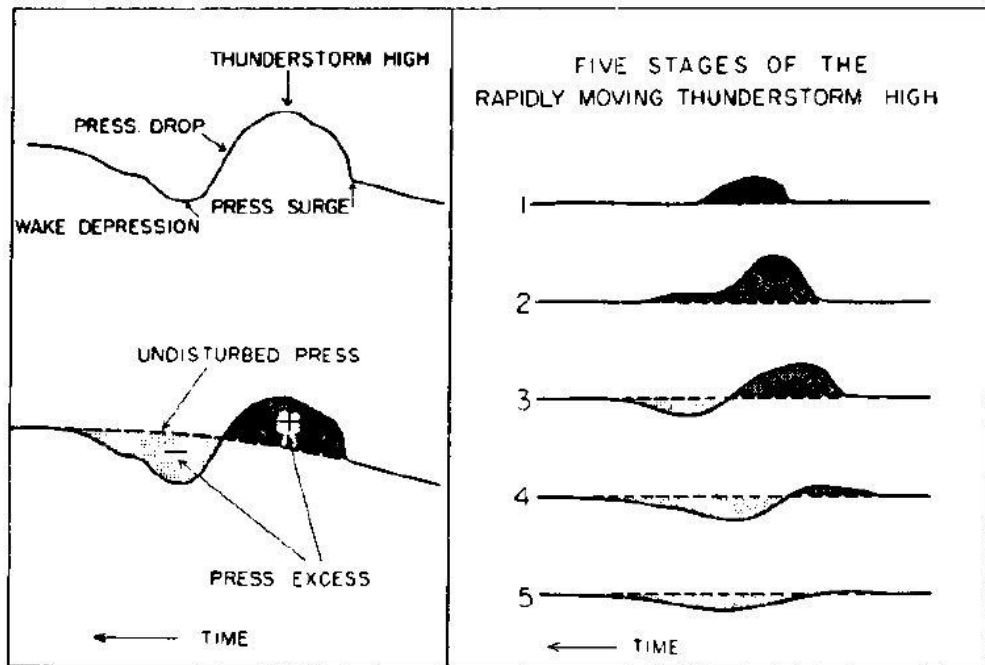


Figure 2.3 - Schematic diagram of barograph trace for a SL thunderstorm. Time runs from right to left. The five stages are: 1) Initiation stage, 2) Development stage, 3) Mature stage, 4) Dissipation stage, and 5) Remnant stage (Source: Fujita, 1955).

Before the work of Rotunno et al. (1988), many works about the longevity of SLs have emphasized in some way the importance of the vertical wind shear, the cold air outflow or the combination of both for the existence of long-lived SLs. In addition, there was the theoretical issue of whether a SL is a system of special, long-lived convective cells, or whether it is a long-lived system of ordinary short-lived convective cells.

Thorpe et al. (1982) simulated the convection in a single long-lived cell. They have concluded that in an environment with no vertical wind shear would have a precipitating cell with surface outflow moving rapidly away from the cell (Fig. 2.4a). Nevertheless, if the low-levels wind shear was strong enough, the outflow would be prevented from moving away from the cell (Fig. 2.4b), which is a favorable condition for intense and long-lived convection.

In the study of Rotunno et al. (1988; known as RKW theory, because the authors are Rotunno, Klemp and Weisman), they proposed that a majority of SLs is a long-lived system formed by short-lived cells with continuous regeneration ahead of the squall line. The

regeneration gives the impression of a line of clouds moving forward and persisting for many hours (Asnani, 2005). RKW theory concluded that the longevity of the intense convection in a SL might be explained by the change of the circulation of the cold outflow due to the presence of low-level wind shear. Basically, without wind shear a cold outflow induces a circulation that inhibits deep vertical penetration of the displaced air (Fig. 2.4c). On the other hand, with sufficient low-level wind shear, the cold outflow spreads ahead of the convection, but has circulation opposed (due to shear) which prevents much displacement and promotes deep lifting triggering new cells produced by the rainy downdraft of prior cell (Fig. 2.4d).
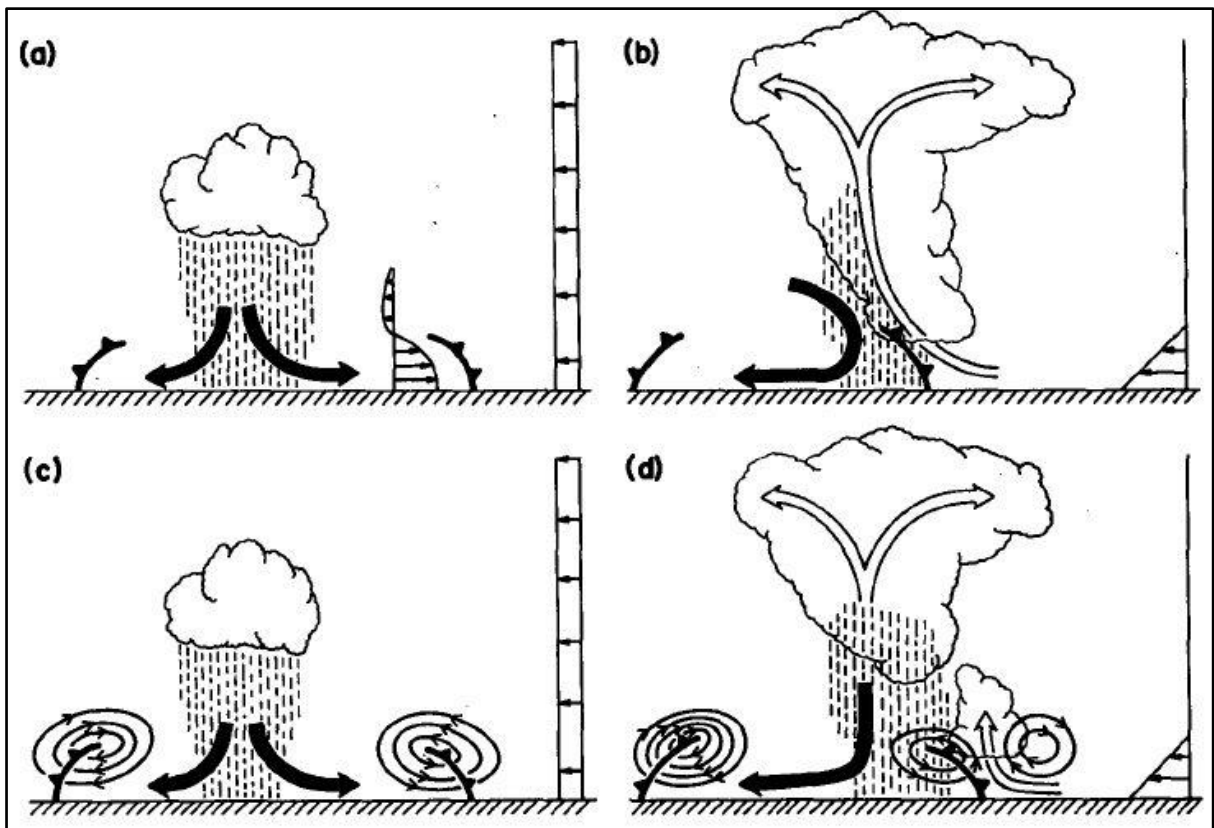


Figure 2.4 - Schematic drawings of the presence of low-level wind shear and/or cold outflow (cold pool). Thorpe et al. (1982) argue that (a) without low-level shear, the rain-produced cold pool propagates away from the cloud above and that the shear at the top of the pool dissipates new cells triggered by the cold pool, whereas (b) with low-level shear, the cold pool remains beneath the cloud and produces a long-lived cell. Here Rotunno et al. argue that (c) without low-level shear, the circulation of a spreading cold pool inhibits deep lifting and so cannot trigger a cell. (d) The presence of low-level shear counteracts the circulation of the cold pool and promotes deep lifting that triggers new cells (Source: Rotunno et al., 1988).

On the other hand, the relationship between thunderstorm upward tilt with the low-levels wind shear was also studied through the balance between the horizontal vorticity produced by the buoyancy gradient across the gust front generated by the cold pool and the

horizontal vorticity associated with environmental low-level vertical wind shear. In the Figure 2.5a can be observed that in the absence of both wind shear and cold pool, the axis of the updraft produced by the thermally created, symmetric vorticity distribution is vertical. In the absence of environmental wind shear but with an evaporative driven cold pool, the distribution is biased by the negative vorticity of the underlying cold pool and updraft tilts rearward over the cold pool (Fig. 2.5b). In the absence of an evaporative driven cold pool, such as early in the lifecycle of a cumulonimbus cloud, environmental wind shear tilts an updraft downshear or toward positive vorticity, which produces an updraft leaned back over the cold pool (Fig. 2.5c). In the presence of both environmental shear and evaporative driven cold pool, a balanced state may exist allowing an erect updraft (Fig. 2.5d) (Rotunno et al., 1988).
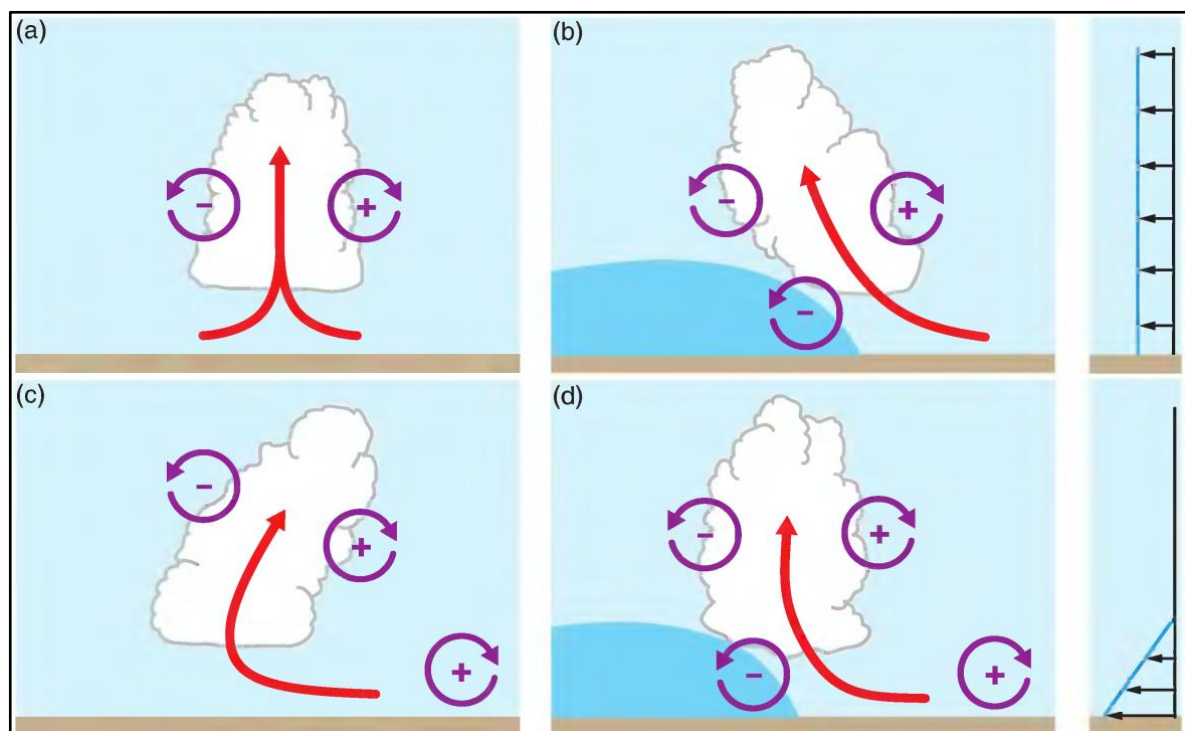


Figure 2.5 - Schematic diagram showing how wind shear and/or a cold pool may influence a buoyant updraft. (a) With no shear and no cold pool. (b) With a cold pool but without wind shear. (c) With shear, but without cold pool. (d) With both a cold pool and shear (Source: adapted from Rotunno et al. (1988) by Markowski and Richardson (2010)).

Rotunno et al. (1988) summarized SLs cases that can develop with less-than-optimal wind shear or otherwise. When the circulation of the cold pool is not countered by a comparable wind shear (a less-than-optimal wind shear), the rear-to-front flow above the cold pool is intensified, the updrafts are weakened and the circulation is highly slanted, but how

the low-level air lifted over the cold pool continue to rise, the SL produce precipitation for long periods. On the other hand, when the circulation of the cold pool is too weak for the low-level wind shear related (a more-than-optimal wind shear), then the SL may be long lived but weak.

Qualitatively, the structure of the cloud systems and the wind and pressure patterns during tropical SL do not present fundamental differences of the mid-latitudes SL (Rotunno et al. 1988). However, the former are much less spectacular than the latter since the perturbation pressure in tropical SL is generally weaker (~ of 2 hPa or are not detected), and tornadoes are much less frequent than in mid-latitudes SL (Asnani, 2005).

Figure 2.6 shows the main features of the structure of a tropical SL synthetized by Zipser (1977) as follow:
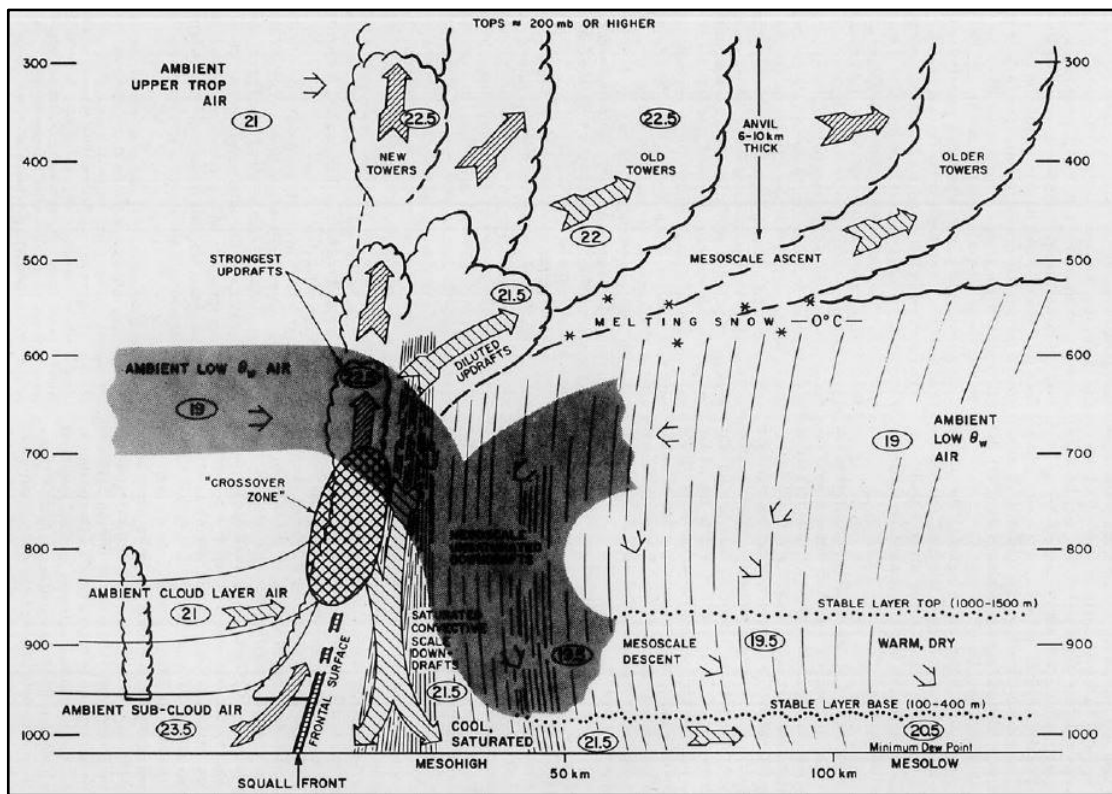


Figure 2.6 - Schematic cross section through a class of squall system. All flow is relative to the SL that is moving from right to left. Circled numbers are typical values of $\theta_w$ in °C. See text for detailed discussion (Source: Zipser, 1977).

In all vertical levels, in the front the relative winds are directed toward SL, but with a minimum flow often above 600-700 hPa. The flow is strongly outward behind SL, from 900 hPa to the surface. Above the squall front along the leading edge, new cumulonimbus cloud

8

growth, and older towers joining the anvil mass trailing behind. The deep of the anvil is 6-10 km, and rains from the anvil base (4-5 km) for 100 km or more in the rear;

From 10 to 30 km behind the squall front, where there are many active cumulonimbus clouds, is very cool and has near-saturated air. In the remainder of the system to the rear the air has $\theta_w$ and relative humidity varying widely. There are two layers in the anvil region, one of intermediate $\theta_w$ (near-saturated air) near the surface, and the other just above the first with relatively warm air and low relative humidity and $\theta_w$. The base of the stable layer, which separates these two layers, marks the top of the mixed layer.

The dew point at the surface drops when the SL passes, but often drops still further in the anvil rainy area. Sometimes reaches the minimum value about 100-200 km behind the SL. In some tropical SLs a mesoescale high-pressure region at the surface tends to accompany the SL itself, followed by a mesoescale low-pressure region about 100-200 km behind.

**Comparison between Tropical and Extra-Tropical Squall Lines**

About the anvil orientation, Ludlam (1963)[1] *apud* Asnani (2005) suggested that the major difference is that, ahead of the travelling tropical SL, the airflow is directed toward the SL at all levels. Therefore, the anvil region is behind the tropical SLs. Otherwise, in the mid-latitudes, the speed of cumulonimbus clouds is close the mean wind of the layer in which is the SL, and so there are SLs with the anvil region in front of it.

According to Ogura and Liou (1980), the anvil in tropical SLs is thicker and larger than in the mid-latitudes SLs. Therefore, the duration of light rain from anvil is longer in tropical SLs. They also suggested that into the anvil of a tropical SL would exist upward motion, product of a mesoescale circulation in the rear. Otherwise, in a mid-latitude SL, the anvil is mainly a result of simple detrainment from the cumulonimbus clouds. Houze (1977) observed that the stratiform rain from the anvil cloud accounted for 40% of the total rainfall from the tropical SL system.

According to Asnani (2005) and Houze (1977), in tropical SLs there are two types of downdrafts. An intense convective-scale downdraft, 10-20 km wide in the narrow zone of

---

[1] Ludlam, F.H., 1963. Severe local storms; A review. Meteor. Monogr., Amer. Meteor. Soc., Vol. 5, No. 27, pp. 1-30.

heavy precipitation of the SL, which spread out at low-levels and one portion of this cold air spread toward the front of the system and produce the squall front just ahead of the heavy rain region. The other downdraft area, lighter but wider (100-500 km wide or of mesoescale dimensions) localized below the anvil precipitation. Otherwise, in mid-latitude SL the downdraft from the anvil is generally smaller and with weak organization.

Asnani (2005) showed that in the tropical SL, the low-level airflow entering presents higher convective instability than in the mid-latitude SL, and concluded that in spite of the differences in some aspects, the basic structure in both SLs is similar.


## 2.1.2. AMAZON SQUALL LINES

Amazon Squall Lines (AmSL) are one of the main mesoescale systems producing rain in the region, mainly between April and August (Cavalcanti, 1982; Cohen et al., 1989[2] *apud* Cohen et al. 1995), and are responsible for the export of large amounts of energy to the atmosphere (Alcântara et al., 2011; Garstang et al., 1994). The average features of AmSL are 700-1900 km length, 100-220 km wide, between 12 and 16 m/s propagation speed, between 9 and 16 hours lifetime (Cohen et al., 1989 *apud* Cohen et al. 1995) and start at afternoon or early night (Garstang et al., 1994). AmSL propagation is in general from northeast to southwest and some events may move for long distances reaching the Andes Mountain (Kousky, 1980; Rickenbach, 2004).

As first approximation, there are two main types of AmSLs considering their formation: the coastal squall lines (CoaSL), which formed over the northeast of South America associated with the sea breeze effect (Kousky, 1980; Cohen et al., 1995; Garstang et al., 1994), and the continental squall lines (ConSL) formed by topographic effect (Cohen et al., 2004). Garstang et al. (1994) identified six possible stages in CoaSL propagating long distances in Amazon basin:

1) coastal genesis, when the first thunderstorm cells form during the afternoon in the sea-breeze convergence zone;

2) intensification, which occurs during late afternoon and evening, with new thunderstorm

---

[2] Cohen, J. C. P., M. A. F. Silva Dias, and C. A. Nobre, 1989: Aspectos climatológicos das linhas de instabilidade na Amazônia. Climanalise. Boletim de monitoramento e Análise Climática. Vol. 4. INPE/CPTEC, 34-40.

cells oriented from northwest to southeast;

3) maturation, when the system achieves maximum length and width;

4) weakening, when the cumulonimbus clusters diminish in size;

5) regeneration that occur in several systems, which regenerate and propagate to the west of Manaus during the period of maximum diurnal heating; and 6) dissipation, when the cumulonimbus clusters disappear.

Cohen et al. (1989 and 1995) divided CoaSLs in three main types according to their inland propagation. The first as Coastal Line of Convection, or CLC, which move no more than 170 km inland; Squall Line type 1 or SL1, which move between 170 and 400 km inland; and Squall Line type 2 or SL2, which displace by more than 400 km inland.

The synoptic analysis of the AmSLs is important since these mesoescale systems are influenced by synoptic circulation.  For example, the SLs follow the north-south displacement of the Intertropical Convergence Zone (ITCZ), developing mainly southward of the ITCZ (Cavalcanti, 1982). Cohen et al. (1989) *apud* Cohen et al. (1995) observed that the majority of AmSLs propagating inland was more frequent when the ITCZ is well established.

Cohen et al. (1995) concluded that the magnitude of the easterly low-level jet was stronger in the days with SLs due possibly to easterly waves and tropical heat sources. Alcântara et al. (2011 and 2014) found direct relationship between the easterly low-level jet depth and the AmSLs propagation. For deeper low-level jet, there is longer propagation of AmSL probably due to supply mid-level inflow into the cloud system that will intensify cloud-scale downdrafts and thus form continually intense cold pools at the surface.

Alcântara (2011) and Garstang et al. (1994) found that the low-level wind shear in AmSLs has the similar behavior of the mid-latitude or tropical SL. Intense wind shear in the low-level inflow may play an important role in the longevity of the SLs. Without wind shear, only unicellular, short-lived, slightly rainy and stationary thunderstorms are produced. Otherwise, the wind directional and speed shears are decisive for the organization and development of a multicellular convective system, as AmSLs. Therefore, the ideal situation for formation of AmSLs is a moderate low-level jet, intense high-level jet, and the presence of both weak directional and moderate speed wind shears at low and medium levels (Alcântara, 2011).

During AmSL in the presence of the colder pools provides higher thermal contrast between the front and the rear of the SL, which promotes cumulus convection development and new cells ahead (Alcântara et al., 2014).

## 2.2. ENERGY IN THE ATMOSPHERE

Solar radiation is the main source of energy for the Earth's atmosphere and as its most prominent effect is to heat the atmosphere-ocean-earth system, the energy produced is internal energy (IE). The atmosphere motions convert IE to kinetic energy (KE), which in turn is dissipated by friction, in order to keep energy balance the process mention above need to continue in loop (Lorenz, 1967).
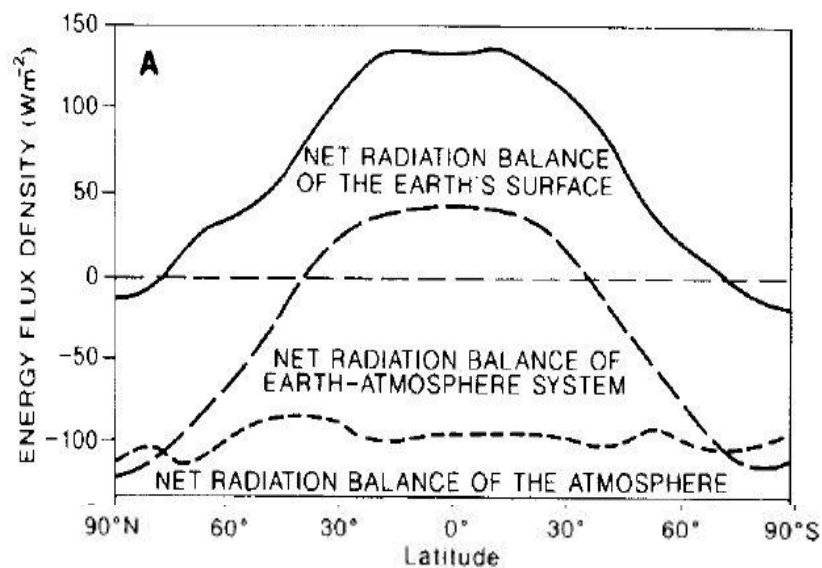


Figure 2.7 - The middle line represents net radiation balance for the earth-atmosphere system (long dashed line). Source: given by Sellers (1965) and adapted by Barry and Chorley (2003).

Differential heating produces the motions in the atmosphere, which makes tropical latitudes warmer than the polar ones, promoting movements to the inter-latitudinal exchanges of heat (Asnani, 2005). For different latitudes, Figure 2.7 shows the observed net radiation energy gain or loss by the atmospheric column.

The principal energy types in the atmosphere are kinetic energy (KE), internal energy (IE) (thermodynamically, the thermal energy and the latent energy of water condensation/fusion

are forms of IE) and potential energy (PE). The last two energy types are the only sources for KE, while the environment may act as a sink (Lorenz, 1955). Because the IE is expressed as $c_v T$, and the PE, as $gz$, (where $c_v$=specific heat at constant volume, $T$=temperature, $g$= acceleration of gravity and $z$=geopotencial height), IE and PE increase or decrease together since both depend on the temperature. Therefore, following Margules (1903)* these energies are jointed as one same type of energy, the total potential energy (TPE) or simply potential energy (Lorenz, 1955; Lorenz, 1967; Asnani, 2005).

Under adiabatic flow, since the total potential energy (TPE) cannot be a good measure of the amount of energy available for conversion into kinetic energy it was developed the concept of the atmospheric available potential energy (APE). Conceptually, the APE of the whole atmosphere is defined as: the difference between the total potential energy at a given moment (can be the current moment) and the minimum total potential energy resulting from any adiabatic redistribution of mass (Lorenz, 1955). Therefore, the APE is a measure of the portion of the TPE available for conversion into KE, hence its name (Lorenz, 1967).

Following Lorenz (1955), the APE has the important properties:

- APE plus the $K_E$ is conserved under adiabatic flow;

- APE is completely determined by the distribution of mass;

- APE is zero if the stratification is horizontal and statically stable and positive otherwise;

- APE is the only source for KE, but it is not the only sink.


The general circulation of the atmosphere may be approximated as compositing of the mean zonal motion and eddies superposed upon it. This permits to divide the kinetic energy of the atmosphere in two types, zonal kinetic energy ($K_Z$) and eddy kinetic energy ($K_E$). Likewise, the available potential energy can be divided in zonal available potential energy ($A_Z$) and eddy available potential energy ($A_E$). The zonal component of energy arises due to variance of zonally averaged temperature, while the eddy component of energy is associated with the variance of temperature within the latitude circles. Each type of energy there is as source or sink for the other type (Lorenz, 1955).

## 2.2.1. LORENZ ENERGY CYCLE

Applying the equations of the continuity, thermodynamic and motion, Lorenz (1955) expressed the local variation of $K_Z$, $K_E$, $A_Z$ and $A_E$ as:

$$\frac{\partial A_Z}{\partial t} = C_Z(K_Z, A_Z) - C_A(A_Z, A_E) + G_Z \quad \dots \quad \textbf{2.1}$$

$$\frac{\partial A_E}{\partial t} = C_A(A_Z, A_E) - C_E(A_E, K_E) + G_E \quad \dots \quad \textbf{2.2}$$

$$\frac{\partial K_Z}{\partial t} = -C_Z(K_Z, A_Z) + C_K(K_E, K_Z) - D_Z \quad \dots \quad \textbf{2.3}$$

$$\frac{\partial K_E}{\partial t} = C_E(A_E, K_E) - C_K(K_E, K_Z) - D_E \quad \dots \quad \textbf{2.4}$$

These terms are part of the Lorenz Energy Cycle and can be expressed in the form of a diagram shown in Figure 2.8.
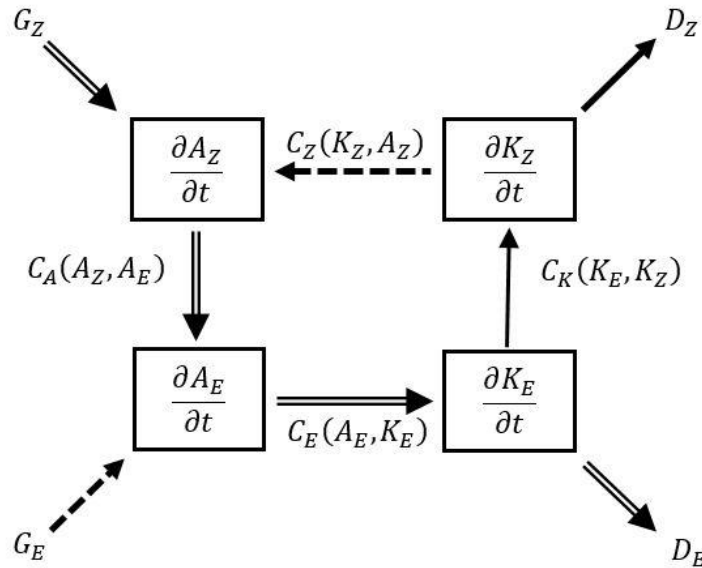


Figure 2.8 - Schematic energy and energy conversions diagram of the atmospheric system. Arrows denote the most likely direction of the conversion between energy components for a large-scale mid-latitude region averaged over the passage of many disturbances. Bold-faced arrows denote a generally large rate of conversion, thin arrows a small rate of conversions and broken arrows a very small rate of conversion or one that is not consistently in one direction. Source: adapted of Carlson (1998).

where $G_Z$ represents generation of zonal available potential energy ($A_Z$) through the latitudinal differential heating produced by the diabatic heat sources (Asnani,1993 and 2005).

$G_E$ represents generation of eddy potential energy ($A_E$) along the same latitude, heating the warm regions and cooling the cold regions, generating gradients of temperature in the same latitude. Physically, the latent heat release due to convection should be an important source of heating and, consequently, of eddy available potential energy ($G_E$) (Dias Pinto, 2010). $C_A$ ($A_Z$, $A_E$) represents the conversion of the available potential energy between zonal and eddy forms, and it is related to the movement of warm tropical air to polar latitudes and cold polar air to warm latitudes through meridional motions. This process decreases the thermal gradient between latitudes diminishing $A_Z$ and increases the thermal gradient at the same latitude resulting in $A_E$ increases, which is related to wave motion (troughs and ridges) and it is an intermediate process in the baroclinic chain. $C_Z$ ($K_Z$, $A_Z$) indicates the conversion of zonal available potential ($A_Z$) into zonal kinetic energy ($K_Z$) through upward movements of warm air in low latitudes and downward movements of cold air in high latitudes. According to Asnani (2005), the Hadley and Ferrel circulations are manifestations of this conversion. Meanwhile, $C_E$ ($A_E$, $K_E$) represents the conversion of eddy available potential ($A_E$) into eddy kinetic energy ($K_E$) through upward motions of warm air and downward movements of cold air along the same latitude circle. The equatorial Walker circulation would be a manifestation of this process. $C_K$ ($K_E$, $K_Z$) represents the conversion of the kinetic energy between zonal and eddy types. According Lorenz (1967), there is no process that converts $A_Z$ into $K_E$ or $A_E$ into $K_Z$. $D_Z$ and $D_E$, represent the effects of friction by zonal and eddy motions, respectively.

Since baroclinic instability is associated with vertical shear of the mean flow and grows by converting potential energy associated with the mean horizontal temperature gradient in kinetic energy (Holton, 2004); in terms of physical processes in the atmosphere, $C_Z$ ($K_Z$, $A_Z$) and $C_E$ ($A_E$, $K_E$) are denominated baroclinic terms because they are strongly related to the processes that present baroclinic instability (Dias Pinto, 2010) or thermal gradients. On the other hand, since barotropic instability is a wave instability associated with the horizontal shear in a jet-like current, and grows by extracting kinetic energy from the mean-flow field (Holton, 2004), $C_K$ ($K_E$, $K_Z$) is called barotropic term. Positive values of $C_K$ ($K_E$, $K_Z$) indicates the conversion of $K_E$ to $K_Z$, and negative otherwise related to the processes where the perturbation extracts kinetic energy from the zonal flow (Asnani, 1993 and 2005; Dias Pinto, 2010).

The energy cycle of the whole atmosphere obtained by Oort (1964) is outlined in Figure 2.9, where f the arrows indicate the directions in which the different processes or conversions occur.
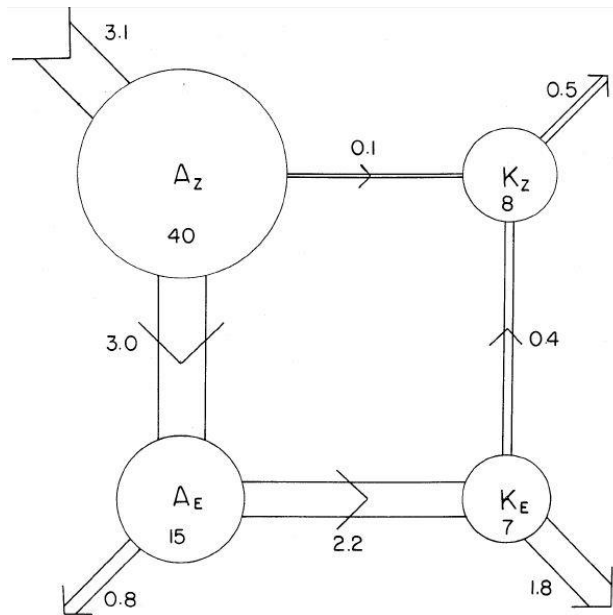
Figure 2.9 - The energy cycle of the atmosphere as estimated by Oort (1964). Values of energy are in units of $10^5$ J m$^{-2}$, and values of generation, conversion, and dissipation are in W m$^{-2}$. Source: Lorenz (1967).

## 2.2.2. ENERGY OF LORENZ IN TROPICAL SYSTEMS

For the period between 1979 and 2007, da Silva and Satyamurty (2013) calculated the components of the LEC for the ITCZ sector covering northern South America and the Atlantic Ocean (area between 5°S-10°N and 50°W-0°). The authors found that: (a) the kinetic energy is greater than the available potential energy, in contrast to the hemispheric situation; (b) the mean energy cycle is much weaker than the hemispheric cycle due to weak thermal gradients; (c) the zonal component of the kinetic energy ($K_Z$) presents the largest variability compared with other energy components; and (d) $K_Z$ it is decreasing during the last 30 years, while the other energy components do not show significant changes. According to da Silva and Satyamurty (2013), the decrease of $K_Z$ suggests a weakening of the trade winds in the Atlantic sector of ITCZ, which may have important implications for the transport of water vapor from the Atlantic to the Amazon basin.

Ramirez et al. (2009) conducted a multivariate Empirical Orthogonal Function (EOF) analysis of land precipitation and of the LEC of the South American rainy season (area between 35° W-75 ° W and 30° S-5 ° N) for the period 1979-2004. The authors found three principal EOF modes. The first EOF (EOF1) represented a dipolar structure of precipitation between South and Central America, describing the fully developed South American Monsoon System (SAMS). In the LEC-EOF1, the diabatic heating release or the eddy

available potential energy generation ($G_E$) was more important than the baroclinic instability, and the generation of zonal available potential energy ($G_Z$) was positive, indicating the importance of thermal gradients in this EOF mode. The second and third EOF modes (EOF2 and EOF3) were similar and described the establishment of the South American Convergence Zone (ZCAS). However, depending on the phase between them, they also expressed the Intertropical Convergence Zone (ZCIT) during austral fall (negative phase of Prec-EOF2), or a climatological summertime SACZ configuration in austral spring (negative phase of Prec-EOF3). The LEC-EOF2 suggested that this pattern occurs when the diabatic heating ($G_Z$ and $G_E$) is of the same order as the baroclinic instability, and so this pattern is different of a frontal system, when the baroclinic instability must be the major term.

In the study of the energetic transformations of African easterly waves, Hsieh and Cook (2007) found the baroclinic conversion as the dominant energy source for the wave generation, although barotropic conversion was almost equally important when there are ITZC convection and surface confluent zone. Asnani (2005) concluded that the generation and maintenance of tropical easterly waves is a manifestation of the energy flow $A_E \rightarrow K_E \rightarrow D_E$, a process maintained by the condensation that creates warm pockets of air along the same latitude circle.

## 2.2.3. EULERIAN AND LAGRANGIAN APPROACHES

According to Michaelides et al. (1999) it is common to use the Eulerian approach in the energetics studies of open atmospheric systems. Eulerian approach considers a unique fixed geographical area, which bounds the system in its all stages of development. The area must be large enough to include the temporal changes in the position and size of the analyzed system. However, although the Eulerian approach simplifies the energetics computations it has the problem of to include the energetics characteristics of adjacent synoptic circulations that are unwanted to consider.

Other possible approach to solve the energetic is the Lagrangian one. For Lagrangian scheme, the synoptic-scale system considered may be isolated throughout its evolution by using a small area around it that is moving with the system. In this way, the boundary of the computational volume can vary with the time implying in a continuously changing volume surrounding the system exclusively. The Lagragian approach needs to consider a conservative property of the system, which can be applied to an air mass with uniform characteristics

making a purely Lagrangian approach practically inapplicable in some cases. Other trouble of a purely Lagrangian framework is the need of consider an isolated system. This implies that the boundaries of the volume must change with time and they must be exclusively bounded the system. The exclusive-bounding condition of Lagrangian approach is difficult to know since is difficult to isolate many systems from the surrounding environment.

Michaelides et al. (1999) followed a quasi-Lagrangian scheme to calculate the LEC terms of a synoptic-scale depression that occurred in December of 1991. For this quasi-Lagrangian calculation, the atmospheric volume was bounded in the vertical by the 100-1000 hPa layer and the horizontal area moved following the position of the center of the system. This volume remained with the same horizontal size during all life cycle of the system (7.5° from the center of the depression in the east, west, north and south directions). Michaelides et al. (1999) also compared the LEC terms using the Eulerian and the quasi-Lagrangian schemes for this event and their results are in the Table 2.1 (table 4 in the work of Michaelides et al. 1999).

The terms that represent the zonal energies ($A_Z$ and $K_Z$) have slight differences in both schemes, but the contrary occurs with the eddy energies. Regarding to energy conversions and frontier energy transports terms, they are very different between Eulerian and quasi-Lagrangian schemes. Therefore, the results in the Table 2.1 show that the energetic terms in this analyzed cyclone is dependent upon the choice of approach.

Table 2.1 - Energy contents, conversions and transfers using the Eulerian and the quasi-Lagrangian schemes. Source: Michaelides et al. (1999).

|  | Eulerian scheme | Quasi-Lagrangian scheme |
|---|---|---|
| $AZ$ | 7.50 | 7.02 |
| $AE$ | 3.83 | 9.41 |
| $KZ$ | 14.48 | 19.18 |
| $KE$ | 10.80 | 4.60 |
| $(KZ - KE)$ | 2.51 | 0.28 |
| $(AZ - AE)$ | −4.47 | 2.68 |
| $(AZ - KZ)$ | 4.05 | 1.89 |
| $(AE - KE)$ | −2.76 | 0.80 |
| $BAZ$ | 3.82 | 3.35 |
| $BAE$ | 5.56 | −0.97 |
| $BKZ$ | −8.59 | 5.18 |
| $BKE$ | −17.61 | 3.70 |

Units used for the energy contents ($AZ$, $AE$, $KZ$ and $KE$) are $10^5$ J m$^{-2}$ and for both the energy conversions ($(KZ - KE)$, $(AZ - AE)$, $(AZ - KZ)$ and $(AE - KE)$) and the energy transfers ($BAZ$, $BAE$, $BKZ$ and $BKE$) are W m$^{-2}$.

# 3. CHAPTER 3: DATA AND METHODS

## 3.1. DATA

The period of 2014-2015 was chosen since it includes the Green Ocean Amazon (GoAmazon) observational campaign, which makes available new observations used to characterize the synoptic environment of SLs.

The project Go Amazon was developed between 01 January 2014 and 31 December 2015 to investigate, understand and enable the study of the coupled atmosphere-cloud-terrestrial tropical systems over the Amazon. The United States Department of Energy (DOE), with collaboration of University of São Paulo (USP) of Brazil and the Max Planck Institute of German conducted this campaign. For more information, consult http://campaign.arm.gov/goamazon2014/.

### 3.1.1. SATELLITE IMAGERY

Animations of Goes-13 Satellite Imagery in the IV channel (infrared) with 4km of spatial resolution at every 30 minutes were used to identify the SLs events (both CSL and ASL) from April to August (more frequency of SLs according to Cohen et al., 1989) 2014 and 2015. These animations covers South America and they are available at the *Centro de Previsão do Tempo e Estudios Climáticos* (CPTEC) webpage http://satelite.cptec.inpe.br/acervo/goes.formulario.logic. For some days, Goes images were not available on CPTEC webpage at every 30 minutes and then infrared Meteosat images were used. These images also are available at the same CPTEC webpage.

In the infrared images, to enhance the temperature, it was used the two-ramp dog-leg scheme for converting unsigned 8-bit integer in the range 0 to 255 into scene temperatures. This scheme is used by the NOAA-NESDIS and it is summarized as follows:

Mode-A: Tscene = 418K - counts (for counts between 255 and 176)

Mode B: Tscene = (660K – counts)/2 (for counts between 176 and 0)

The method is described at the Goes webpage: http://goes.gsfc.nasa.gov/text/

imager.calibration.html

### 3.1.2. TROPICAL RAINFALL MEASURING MISSION

The occurrence of precipitation in the SL was verified using the 3-hourly estimated rainfall from Tropical Rainfall Measuring Mission (TRMM) Multi-Satellite Precipitation Analysis (TMPA). The horizontal grid spacing of the TRMM data is 0.25° and it was used the estimation product denominated 3B42 (Huffman and Bolvin, 2015), which is available at https://pmm.nasa.gov/data-access/downloads/trmm.

### 3.1.3. ATMOSPHERIC SOUNDINGS

The data of soundings of Manacapuru municipality located in the Brazilian state of Amazonas were used to identify a vertical profile of wind, temperature and other meteorological variables of the SLs. The soundings are available in the Atmospheric Radiation Measurement (ARM) Climate Research Facility webpage (http://www.archive.arm.gov/armlogin/login.jsp) and they were obtained for Green Ocean Amazon (GOAmazon) campaign between 2014 and 2015 in the location 3.21°S – 60.6°W (Manacapuru-MAN).
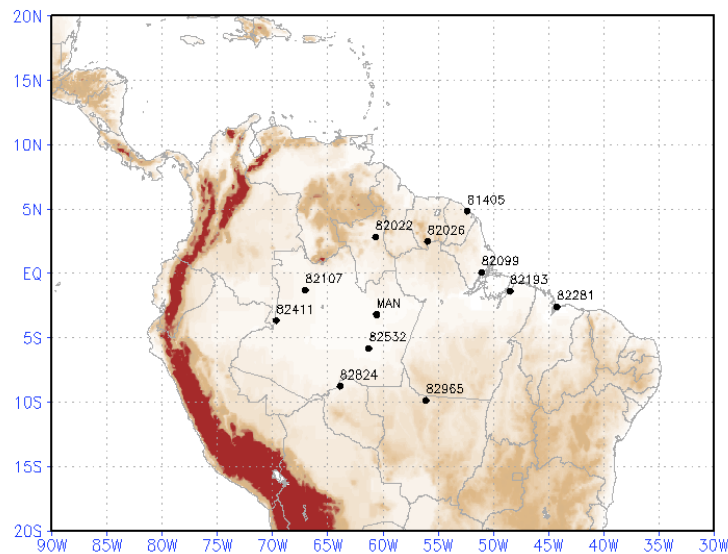


Figure 3.1 - Location of sounding stations over the Amazon basin.

In addition, atmospheric soundings of other points scattered over the Amazonian basin (see Fig. 3.1) were used. These data are available at University of Wyoming webpage (http://weather.uwyo.edu/upperair/sounding.html) and Table 3.1 provides their locations.

Table 3.1 - Number, name and location (latitude and longitude) of sounding stations over the Amazon basin. Source: http://weather.uwyo.edu/upperair/sounding.html

| WMO-SYNOP Index | ICAO Index | Common Name | Lat | Lon |
|---|---|---|---|---|
| 82022 | SBBV | Boa Vista | 2.83 | -60.70 |
| 82965 | SBAT | Alta Floresta (Aero) | -9.86 | -56.10 |
| 82411 | --- | Tabatinga | -3.67 | -69.67 |
| 82824 | SBPV | Porto Velho (Airport) | -8.76 | -63.91 |
| 82532 | --- | Manicore | -5.82 | -61.28 |
| 82107 | --- | São Gabriel Da Cachoeira | -1.30 | -67.05 |
| 82281 | --- | São Luiz | -2.60 | -44.23 |
| 82193 | SBBE | Belem (Airport) | -1.38 | -48.48 |
| 82099 | SBMQ | Macapa | 0.05 | -51.07 |
| 82026 | --- | Tirios | 2.48 | -55.98 |
| 81405 | SOCA | Rochambeau | 4.83 | -52.37 |

3.1.4. GLOBAL FORECAST SYSTEM ANALYSIS

Data of Global Forecast System (GFS) analysis with $0.5°$ of horizontal resolution, in 22 pressure levels (1000, 975, 950, 925, 900, 850, 800, 750, 700, 650, 600, 550, 500, 450, 400, 350, 300, 250, 200, 150, 100 and 70 hPa) and every 6 hours was employed for: to select SLs events that produced rain seen by the model, to identify synoptic patterns, to calculate all energetic terms (Lorenz Cycle and kinetic energy) and the thermodynamic balance. GFS data is available at https://www.ncdc.noaa.gov/data-access/model-data/model-datasets/global-forcast-system-gfs.

GFS analysis was chosen since it model cover the entire globe with horizontal grid spacing of 28 km (National Center for Environmental Information of NOAA, 2016), enabling it to better capture the environment that favors the SL.

In a previous experiment, Era Interim reanalysis data was used, but it did not represent SL signals because it has a horizontal resolution of 79 km (Berrrisford et al., 2011). As the purpose of this research was to work with an operational model, the GFS model was chosen because it represented better SLs and it has higher resolution.

## 3.2.  METHODS

### 3.2.1. SQUALL LINES IDENTIFICATION

Considering that, the frequency of SLs is larger between April and August (Cohen et al., 1989; Oliveira et al., 2016); in this study were identified events of SLs in these months of 2014 e 2015 using satellite imagery animations. These years were chosen since the Green Ocean Amazon (GoAmazon) project provided the sounding data of Manacapuru municipality (Amazonas-Brazil) used to the analysis.

The SL identification considered all events with at least 6 hours of lifetime that emerged in the northeast coast of South America (SA) (3°S-7°N and 50°W-40°W), which includes most part of the region of the Amazon SLs formation that is between 10°N and 5°S (Cohen et al., 1995). For classify them, was considered 10° of inland propagation because in the visual identification the limit of the Amazonas region is 10° from the coast and this limit was the initial boundary for classification of the SL. The SLs that propagated less than 10° since their formation on the coast were called Coastal Squall Lines (CSL), and those that displaced more of 10° to the west were called Amazonian Squall Lines (ASL).

### 3.2.2. SYNOPTIC ANALYSIS

The synoptic patterns of atmospheric circulation in the SL events were obtained from GFS analysis data (wind, geopotencial height, sea level pressure, moisture, divergence, and temperature) at different pressure levels.  Additionally, in this section were used the satellite imagery, TRMM precipitation estimation and GFS precipitation of both SCL and ASL events selected.

For the synoptic analysis, were analyzed horizontal maps of wind, vertical velocity,

divergence, relative vorticity, mean sea level pressure, speed shear, thickness and moisture in representative layers, also were analyzed vertical profile of wind in specific points with maximum convection.

### 3.2.3. LORENZ ENERGY CYCLE IN A LIMITED AREA

Studies of the energetic of synoptic systems using Lorenz Cycle were performed for different authors such as (a) Brennan and Vincent (1980), Michaelides (1987), Dias Pinto (2010) and Dias Pinto and da Rocha (2011) for investigation of cyclones. (b) Veiga et al. (2013) to study the Walker Circulation and its relationship with ENSO. (c) Norquist et al. (1977) and Hsieh and Cook (2007) to evaluate the African easterly waves. (d) da Silva and Satyamurty (2013) in the Intertropical Convergence Zone in the South American sector of the Atlantic Ocean. (e) Ramirez et al. (2009) in a work about the energy of the South American rainy season. These works have used the Lorenz Energy Cycle (LEC) in limited area as proposed by Muench (1965), considering the transfer of energy across the boundaries.

The LEC in a limited area using the form and the notation given by Michaelides (1987) was used in this work:

$$\frac{\partial A_Z}{\partial t} = C_Z(K_Z, A_Z) - C_A(A_Z, A_E) + G_Z + BA_Z \quad \dots \quad \textbf{3.1}$$

$$\frac{\partial A_E}{\partial t} = C_A(A_Z, A_E) - C_E(A_E, K_E) + G_E + BA_E \quad \dots \quad \textbf{3.2}$$

$$\frac{\partial K_Z}{\partial t} = -C_Z(K_Z, A_Z) + C_K(K_E, K_Z) - D_Z + BK_Z + B\Phi_Z \quad \dots \quad \textbf{3.3}$$

$$\frac{\partial K_E}{\partial t} = C_E(A_E, K_E) - C_K(K_E, K_Z) - D_E + BK_E + B\Phi_E \quad \dots \quad \textbf{3.4}$$

where $_Z$ and $_E$ represent zonal and eddy energies, respectively.

According Lorenz (1967) $A_Z$ represents the amount of available potential energy that would exist if the all mass field was replaced by its zonal average, and $A_E$, the excess of available potential energy over $A_Z$. Likewise, $K_Z$ represents the amount of kinetic energy which would exist if the existing zonally averaged motion but no eddy motion were present, and $K_E$, the excess of kinetic energy over $K_Z$. The equations for these types of energy are:

$$A_Z = \int_{pt}^{pb} \frac{\overline{T^{*2}}}{2\bar{\sigma}} dp \quad \dots \quad \textbf{3.5}$$

$$A_E = \int_{pt}^{pb} \frac{\overline{T'^2}}{2\bar{\sigma}} dp \quad \dots \quad \textbf{3.6}$$

$$K_Z = \frac{1}{2g} \int_{pt}^{pb} \overline{([u]^2 + [v]^2)} dp \quad \dots \quad \textbf{3.7}$$

$$K_E = \frac{1}{2g} \int_{pt}^{pb} \overline{(u'^2 + v'^2)} dp \quad \dots \quad \textbf{3.8}$$

In the equations 3.1 – 3.4 the terms with C express conversions between different types of energy; terms with G, generation of available potential energy; terms with D, dissipation of kinetic energy; and terms with B, energy flux across the boundary.

The equations for conversion one form of energy to another are:

$$C(K_Z, A_Z) = -\frac{1}{g} \int_{pt}^{pb} \frac{R}{p} \overline{\omega^* T^*} dp \quad \dots \quad \textbf{3.9}$$

$$C(A_E, K_E) = -\frac{1}{g} \int_{pt}^{pb} \frac{R}{p} \overline{\omega' T'} dp \quad \dots \quad \textbf{3.10}$$

$$C(A_Z, A_E) = \int_{pt}^{pb} \left( \frac{1}{2\bar{\sigma}a} \overline{v'T' \frac{\partial T^*}{\partial \phi}} + \overline{\frac{\omega'T'}{p^{R/cp}} \frac{\partial}{\partial p} \left( \frac{T^* p^{R/cp}}{\bar{\sigma}} \right)} \right) dp \quad \dots \quad \textbf{3.11}$$

$$C(K_E, K_Z) = \frac{1}{g} \int_{pt}^{pb} \left( \overline{\frac{\cos\phi}{a} u'v' \frac{\partial}{\partial \phi}\left(\frac{[u]}{\cos\phi}\right)} + \overline{\frac{v'^2}{a} \frac{\partial [v]}{\partial \phi}} + \overline{\frac{\tan\phi}{a} u'^2 [v]} + \overline{\omega'u' \frac{\partial [u]}{\partial p}} \right.$$
$$\left. + \overline{\omega'v' \frac{\partial [v]}{\partial p}} \right) dp \quad \dots \quad \textbf{3.12}$$

The equations for processes indicating energy flux across the boundary:

$$BA_Z = -\frac{1}{a(\lambda_E - \lambda_W)(\sin\phi_N - \sin\phi_S)} \int_{pt}^{pb} \int_{\phi_S}^{\phi_N} \frac{1}{2\bar{\sigma}} (2T^*T'u + T^{*2}u)_{\lambda_W}^{\lambda_E} d\phi dp$$

$$-\frac{1}{a(\sin\phi_N - \sin\phi_S)} \int_{pt}^{pb} \frac{1}{2\bar{\sigma}} \{([v'T']T^* + T^{*2}[v])\cos\phi\}_{\phi_S}^{\phi_N} dp$$

$$-\frac{1}{2\bar{\sigma}} \left( 2[\omega'T']T^* + T^{*2}[\omega] \right)_{pt}^{pb} \quad \dots \quad \textbf{3.13}$$

$$BA_E = -\frac{1}{a(\lambda_E - \lambda_W)(sin\phi_N - sin\phi_S)}\int_{pt}^{pb}\int_{\phi_S}^{\phi_N}\frac{1}{2\bar{\sigma}}(uT'^2)_{\lambda_W}^{\lambda_E}d\phi dp$$

$$-\frac{1}{a(sin\phi_N - sin\phi_S)}\int_{pt}^{pb}\frac{1}{2\bar{\sigma}}\{[v'T'^2]cos\phi\}_{\phi_s}^{\phi_N}dp$$

$$-\frac{1}{2\bar{\sigma}}\overline{(\omega'T'^2)}_{pt}^{pb} \quad ... \quad \textbf{3.14}$$

$$BK_Z = -\frac{1}{a(\lambda_E - \lambda_W)(sin\phi_N - sin\phi_S)}\int_{pt}^{pb}\int_{\phi_S}^{\phi_N}\frac{1}{2g}(u[u^2 + v^2 - u'^2 - v'^2])_{\lambda_W}^{\lambda_E}d\phi dp$$

$$-\frac{1}{a(sin\phi_N - sin\phi_S)}\int_{pt}^{pb}\frac{1}{2g}\{[vcos\phi(u^2 + v^2 - u'^2 - v'^2)]\}_{\phi_s}^{\phi_N}dp$$

$$-\frac{1}{2g}\overline{\omega(u^2 + v^2 - u'^2 - v'^2)}_{pt}^{pb} \quad ...\textbf{3.15}$$

$$BK_E = -\frac{1}{a(\lambda_E - \lambda_W)(sin\phi_N - sin\phi_S)}\int_{pt}^{pb}\int_{\phi_S}^{\phi_N}\frac{1}{2g}(u[u'^2 + v'^2])_{\lambda_W}^{\lambda_E}d\phi dp$$

$$-\frac{1}{a(sin\phi_N - sin\phi_S)}\int_{pt}^{pb}\frac{1}{2g}\{[vcos\phi(u'^2 + v'^2)]\}_{\phi_s}^{\phi_N}dp$$

$$-\frac{1}{2g}\overline{\omega(u'^2 + v'^2)}_{pt}^{pb} \quad ... \quad \textbf{3.16}$$

where $a$ denotes the mean radius of the earth.

The equations that express processes which generates available potential energy and which dissipates kinetic energy are:

$$G_Z = \int_{pt}^{pb}\frac{\overline{Q^*T^*}}{c_P\bar{\sigma}}dp \quad ...\textbf{3.17}$$

$$G_E = \int_{pt}^{pb}\frac{\overline{Q'T'}}{c_P\bar{\sigma}}dp \quad ...\textbf{3.18}$$

$$D_Z = \frac{1}{g}\int_{pt}^{pb}\overline{([u][F_\lambda] + [v][F_\phi])}dp \quad ...\textbf{3.19}$$

$$D_E = \frac{1}{g}\int_{pt}^{pb}\overline{(u'F_\lambda + v'F_\phi)}dp \quad ...\textbf{3.20}$$

where Q and F represent diabatic fonts of heat and friction, respectively.

In the equations 3.5 – 3.20, *pb* and *pt* are lower and upper limits of pressure for the vertical integration; and the statistic concepts of:

Zonal Mean: $[(\ )] = \frac{1}{\lambda_E - \lambda_W} \int_{\lambda_W}^{\lambda_E} (\ )\, d\lambda$  ...  **3.21**

Areal Mean: $\overline{(\ )} = \frac{1}{sin\varphi_N - sin\varphi_s} \int_{\phi_S}^{\phi_N} (\ )\, cos\phi d\phi$  ...**3.22**

Zonal Mean Deviation: $(\ )' = (\ ) - [(\ )]$  ...  **3.23**

Areal Mean Deviation of Zonal Mean: $(\ )^* = [(\ )] - \overline{(\ )}$  ...  **3.24**

where $\varphi$ and $\lambda$ are horizontal limits of latitude and longitude, respectively.

$\bar{\sigma}$ represents the mean static stability parameter, its equation is:

$$\bar{\sigma} = \overline{\left( \frac{gT}{c_p} - \frac{pg}{R}\frac{\partial T}{\partial p} \right)} \quad ... \quad \textbf{3.25}$$

where $g$ is the acceleration of gravity; $c_p$ , the specific heat at constant pressure; T, temperature; p, pressure; and R is the universal gas constant.

The terms $B\Phi_Z$ e $B\Phi_E$ were added by Muench (1965) and express the appearance of $K_Z$ and $K_E$ within the volume of the limited region associated with work produced at its boundaries. In preliminary studies obtained quite unrealistic values of these terms and so in Michaelides (1987) they were combined with dissipation terms as follows and they were estimated as residuals of equations 3.3 and 3.4, resulting in:

$$-\Delta R_z = B\Phi_Z - D_Z + \varepsilon_{KZ} \quad ... \quad \textbf{3.26}$$

$$-\Delta R_E = B\Phi_E - D_E + \varepsilon_{KE} \quad ... \quad \textbf{3.27}$$

Likewise, the terms $G_Z$ and $G_E$ were estimated as residuals of equation 3.1 and 3.2, resulting in:

$$\Delta G_z = G_z + \varepsilon_{AZ} \quad ... \quad \textbf{3.28}$$

$$\Delta G_E = G_E + \varepsilon_{AE} \quad ... \quad \textbf{3.29}$$

where the terms with $\varepsilon$   represent the accumulated error from the numerical estimation of each of the other terms in equations 3.1 – 3.4.

Considering all these estimations, the LEC of the Figure 2.8 was modified and shown in

the next equations and Figure 3.2:

$$\frac{\partial A_Z}{\partial t} = C_Z(K_Z, A_Z) - C_A(A_Z, A_E) + \Delta G_Z + BA_Z \quad \text{...} \quad \textbf{3.30}$$

$$\frac{\partial A_E}{\partial t} = C_A(A_Z, A_E) - C_E(A_E, K_E) + \Delta G_E + BA_E \quad \text{...} \quad \textbf{3.31}$$

$$\frac{\partial K_Z}{\partial t} = -C_Z(K_Z, A_Z) + C_K(K_E, K_Z) - \Delta R_Z + BK_Z \quad \text{...} \quad \textbf{3.32}$$

$$\frac{\partial K_E}{\partial t} = C_E(A_E, K_E) - C_K(K_E, K_Z) - \Delta R_E + BK_E \quad \text{...} \quad \textbf{3.33}$$
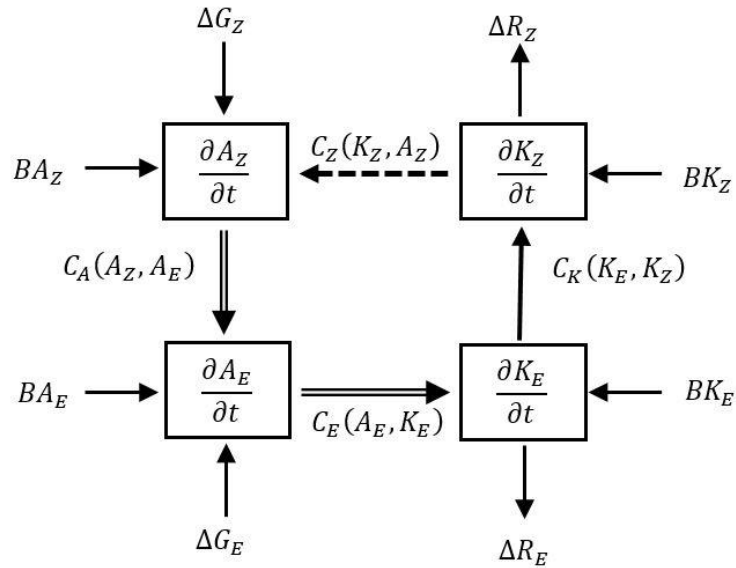


Figure 3.2 - Diagram of Lorenz Energy Cycle (LEC) in a limited area (Michaelides, 1987)

In this work was used this LEC in a limited area (Fig. 3.2 and equations 3.1 – 3.29) for two SLs episodes, a CSL and an ASL.

3.2.4. KINETIC ENERGY

In order to determine which component of kinetic energy is more important, in this study also was used the kinetic energy equation in isobaric coordinates in the form and with the notation of Fuelberg and Scoggins (1978) and given by Smith (1969). It is applicable to

hydrostatic systems and allowed for boundary transport. The equation is:

$$\frac{\partial K}{\partial t} = \frac{1}{g}\int_{pt}^{pb} \overline{-\vec{V}.\vec{\nabla}_P \emptyset}\, dp - \frac{1}{g}\int_{pt}^{pb} \overline{\vec{\nabla}_P . k\vec{V}}\, dp - \frac{1}{g}\int_{pt}^{pb} \overline{\frac{\partial \omega k}{\partial p}}\, dp$$

$$\qquad\qquad\quad \textbf{(a)} \qquad\qquad\qquad \textbf{(b)} \qquad\qquad \textbf{(c)}$$

$$+\frac{1}{g}\int_{pt}^{pb} \overline{\vec{V}.\vec{F}}\, dp + \overline{k_o \frac{\partial p_o}{\partial t}} \quad \dots \; \textbf{3.34}$$

$$\qquad\qquad \textbf{(d)} \qquad\qquad \textbf{(e)}$$

where:

$$K = \int_{pt}^{pb} k\, dp \qquad\qquad \emptyset = gz$$

$\vec{V}$ = Horizontal wind vector

$\omega$ = Vertical motion in isobaric coordinates $[= dp/dt]$

$k$ = Horizontal kinetic energy per unit mass $[= (u^2 + v^2)/2]$

$\vec{F}$ = Frictional force per unit mass

$A$ = Area of computation

Subscript $_o$ denotes surface values

Local changes in kinetic energy for a fixed volume ($\partial K / \partial t$) result from five processes. Term (a) is the generation of kinetic energy from the work done by the horizontal pressure gradient on the mass of the atmosphere over the volume studied (Kung, 1966) or the rate at which kinetic energy within the systems is changed by pressure gradient forces (Smith, 1970). Terms (b) and (c) represent horizontal and vertical flux divergence of kinetic energy, respectively, and represent interaction of the limited volume with surrounding atmosphere. Term (d) represents thermodynamic frictional processes or dissipation and it is calculated as residual of equation 3.34, and so it represents a transfer of energy between grid and subgrid scales of motion due mostly to unresolvable eddy processes. At the last, the term (e) represent changes in kinetic energy due the changes in mass of the volume studied (Fuelberg and Scoggins, 1978).

### 3.2.5. THERMODYNAMIC BALANCE EQUATION

During a SL development, the heating released influence in its surrounding atmosphere making important to study the heat budget in its synoptic environment (Braun and Houze, 1996).

Starting from the first law of thermodynamic applied to a system in thermodynamic equilibrium (or not) in motion, it is obtained the commonly called thermodynamic energy equation (Holton, 2004), which with the help of the continuity equation, can be expressed as (Asnani, 2005):

$$\frac{\partial}{\partial t}\left(c_p T\right) + \nabla.\left(c_p T \vec{V}\right) + \frac{\partial}{\partial p}\left(c_p T \omega\right) - \omega\alpha = Q \quad \text{...} \quad \mathbf{3.35}$$

The thermodynamic equation in the heat balance form is expressed as:

$$\frac{\partial T}{\partial t} + \left(\frac{u}{a\,cos\varphi}\frac{\partial T}{\partial\lambda} + \frac{v}{a}\frac{\partial T}{\partial\varphi}\right) + \omega\left(\frac{\partial T}{\partial p} - \frac{\alpha}{c_p}\right) = \frac{Q}{c_p} \quad \text{...} \quad \mathbf{3.36}$$

where $\partial T / \partial t$ represents local changes of temperature; the second term in the left hand represents changes in temperature due to horizontal advection; the third term, the adiabatic heating; and the term in the right hand, the diabatic heating. This latter term can be considered as the rate of heating per unit mass due to radiation, conduction, and latent heat release according Holton (2004), or mainly as latent heating effects (Sinclair, 1993).

# 4. CHAPTER 4: RESULTS AND DISCUSSIONS

## 4.1. SQUALL LINES IDENTIFIED IN 2014 AND 2015

In this section, SLs identified between April and August of 2014 and 2015 are presented and classified as CSL or ASL. Their mean features are described, analyzed and compared with those obtained in other works of Amazon SLs.

Table 4.1 - List of SLs identified between April and August 2014.

| Date (2014) | Type | Approx. h_start (UTC) | Approx. h_end (UTC) | Approx. duration (h) | Inland propagation (km) | Propag. Speed (m s$^{-1}$) | Length in its maximum develop. (km) | Width in its maximum develop. (km) |
|---|---|---|---|---|---|---|---|---|
| 31 Mar to 02 Apr | **ASL\*** | 14:30 | 15:00 | 48:30 | 3221 | 18,4 | 2220 | 524 |
| 27 to 28 Apr | CSL | 13:00 | 13:00 | 24:00 | 755 | 8,7 | 1694 | 399 |
| 29 to 30 Apr | CSL | 15:00 | 07:00 | 16:00 | 1110 | 19,3 | 2286 | 313 |
| 15 to 16 May | CSL | 19:00 | 05:00 | 10:00 | 333 | 9,3 | 1847 | 268 |
| 09 to 10 Jun | CSL | 15:00 | 07:00 | 16:00 | 316 | 5,5 | 1601 | 176 |
| 28 to 29 Jun | **ASL** | 16:30 | 10:00 | 17:30 | 1535 | 24,7 | 2288 | 157 |
| 20 to 21 Aug | CSL | 18:30 | 08:00 | 13:30 | 434 | 8,9 | 1821 | 142 |
| 21 to 22 Aug | CSL | 19:30 | 05:00 | 9:30 | 248 | 7,3 | 808 | 111 |
| 31 Aug to 01 Sep | CSL | 19:00 | 14:00 | 19:00 | 785 | 11,5 | 1180 | 124 |

\*ASLs that reached the Peruvian Amazon.

Between April and August 2014 (Table 4.1) and 2015 (Table 4.2) were identified 21 SLs, being fifteen classified as CSL and six as ASL. According to Alcantara et al. (2011) and Cohen et al. (1995), almost half of the SLs that started in the northeast coast of South America propagated more than 170 km inland and it is the type of SLs studied in the present work. Considering inland propagation, the SLs identified here would be classified as Squall Line type 1 and type 2 (SL1 and SL2) in Cohen et al. (1989) since they propagated more than 170 km inland. Considering SL genesis place, they are considered as Amazon Coastal Squall Lines (ACSL) in Garstang et al. (1994) because are SLs having coastal genesis and

propagating across the central Amazon Basin.

Table 4.2 - List of SLs identified between April and August 2015.

| Date (2015) | Type | Approx. h_start (UTC) | Approx. h_end (UTC) | Approx. duration (h) | Inland propagation (km) | Propag. speed (m s⁻¹) | Length in its maximum develop. (km) | Width in its maximum develop. (km) |
|---|---|---|---|---|---|---|---|---|
| 31 Mar to 01 Apr | CSL | 17:00 | 04:30 | 11:30 | 389 | 9,4 | 1355 | 231 |
| 11 to 13 Apr | ASL* | 11:00 | 12:00 | 49:00 | 2887 | 16,4 | 1493 | 265 |
| 17 to 18 Apr | CSL | 14:00 | 09:00 | 19:00 | 969 | 14,2 | 1578 | 200 |
| 22 to 23 Apr | CSL | 10:00 | 07:00 | 21:00 | 923 | 12,2 | 1493 | 157 |
| 06 to 07 May | ASL | 16:00 | 18:00 | 26:00 | 1226 | 13,1 | 2220 | 392 |
| 01 to 02 Jun | CSL | 18:30 | 03:30 | 9:00 | 598 | 18,4 | 1180 | 111 |
| 10 to 11 Jun | ASL | 17:00 | 22:00 | 29:00 | 1404 | 13,4 | 1727 | 248 |
| 13 to 14 Jun | CSL | 07:30 | 04:00 | 20:30 | 1020 | 13,8 | 993 | 111 |
| 13 to 14 Jul | CSL | 16:00 | 02:00 | 10:00 | 503 | 14 | 1295 | 56 |
| 14 to 15 Jul | CSL | 17:00 | 02:00 | 9:00 | 392 | 12,1 | 948 | 89 |
| 24 to 25 Jul | CSL | 17:00 | 05:00 | 12:00 | 613 | 14,2 | 1665 | 126 |
| 17 to 18 Aug | ASL | 18:00 | 14:00 | 20:00 | 1405 | 19,5 | 1665 | 200 |

*ASLs that reached the Peruvian Amazon.

The mean features for CSL events were 11.9 m s$^{-1}$ of propagation speed, 15 hours of lifetime, 626 km of inland propagation, 1450 km of length, and 174 km of width in its maximum development. The majority of the CSL type started between 15:00 and 18:00 UTC and finished between 03:00 and 06:00 UTC. The Figure 4.1 presents the trajectories of the fifteen CSLs, where it is noted a preferential movement of CSLs from northeast to southwest.
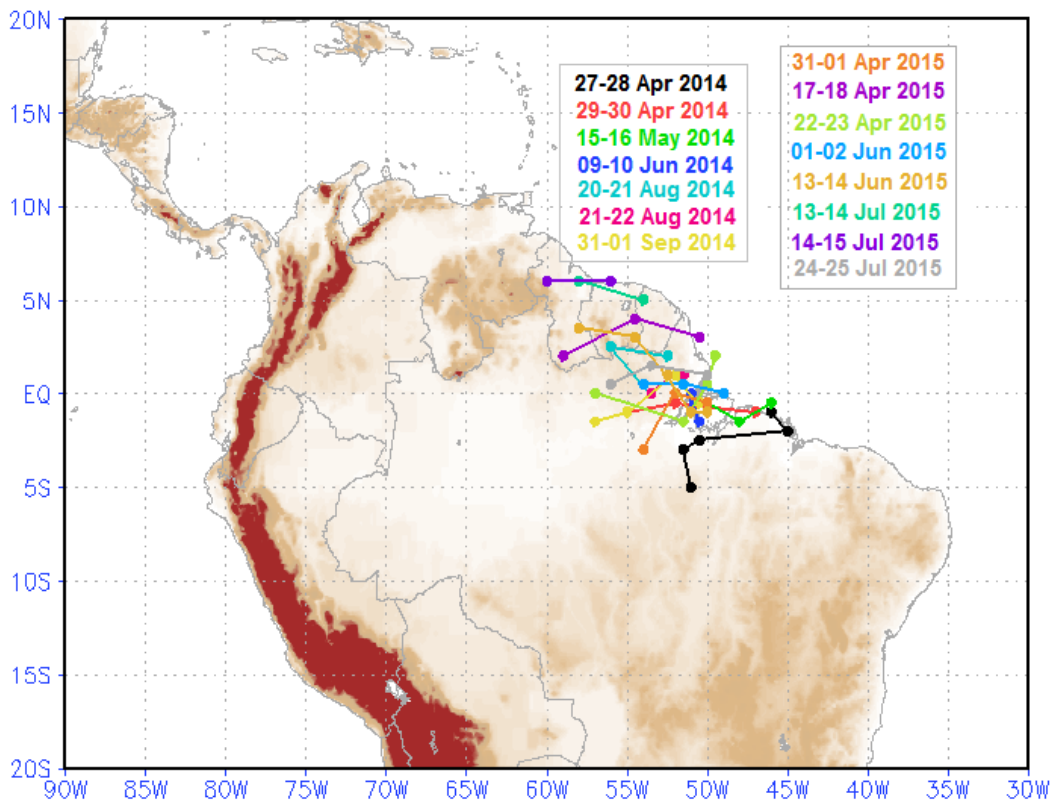
Figure 4.1 - Trajectories of Coastal Squall Lines (CSL) between April and August 2014 and 2015. The points represent the center of the SL and are separated each 6 hours.

Regarding the ASLs, of the six ASL found, two displaced more of 20° of longitude from the beginning on the coast to the west until reached the Peruvian Amazon. These SLs were not considered to calculate mean features of the ASLs since the lifetime and inland propagation of them are almost twice as many as the others. The mean characteristics of these two ASLs were 17.4 m s$^{-1}$ of speed propagation, 49 hours of lifetime, 3054 km of inland propagation, 1857 km of length and 394 km of width in its maximum development. These two ASLs started and finished at hours near to 12:00 UTC.

The mean features of the remaining four ASLs were 17.7 m s$^{-1}$ of speed propagation, 23 hours of lifetime, 1393 km of inland propagation, 1975 km of length and 249 km of width in its maximum development. The majority of these ASLs started at 17:00 UTC and finished near the 15:00 UTC.

The trajectories of ASLs are illustrated in the Figure 4.2 and it is noted a preferential movement of ASLs from northeast to southwest like CSLs.
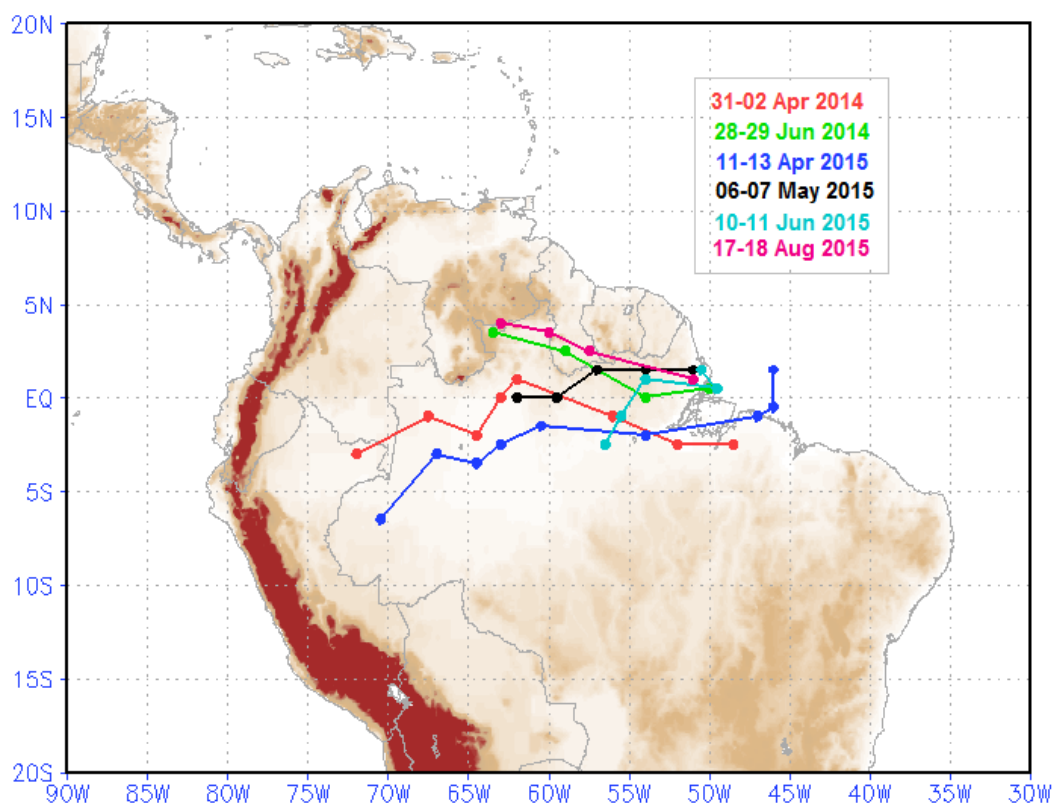
Figure 4.2 - Trajectories of Amazonian Squall Lines (ASL) between April and August 2014 and 2015. The points represent the center of the SL and are separated each 6 hours.

The Table 4.3 summarize the mean characteristics of AmSLs (both CSL as ASL), which are similar than those found in other works (Cohen (1989); Greco et al. 1990; Garstang et al, 1994; Santos Neto[3] (2004) *apud* Cavalcanti et al. (2009)). Slight differences between some features of Amazon SLs may be due to different periods of analysis.

Table 4.3 - Comparison of average characteristics of AmSLs in different works

| Mean Characteristics | Cohen (1989) | Greco et al (1990); Garstang et al. (1994) | Santos Neto (2004) | This work |
|---|---|---|---|---|
| Type of SL | SL1 and SL2 | ACSL | --- | CSL and ASL |
| Years analyzed | 8 | 1 | 23 | 2 |

[3] SANTOS NETO L.A. Análise observacional das linhas de instabilidade formadas na costa norte-nordeste da América do Sul. Trabalho de Conclusão de Curso (Graduação em Meteorologia) – Universidade Federal do Pará, 2004.

|  | (1979-1986) | (1987) | (1979-2002) | (2014-2015) |
|---|---|---|---|---|
| Length (km) | 1400 | 1000-2000 | 1344 | 1712 |
| Width (km) | 170 | 100-300 | --- | 212 |
| Speed (m s$^{-1}$) | 12-16 | 14-17 | 15.4 | 15 |
| Lifetime (hours) | 12-16 | 24-48 | 20.4 | 19 |

In both SL types is notable that the starting point of SLs advanced from south to north as time progressed, from April to August. According to Cavalcanti (1982), this occurs due to the northward displacement of the ITCZ in austral winter. Likewise, the period when the SLs are wider coincides with period when the ITCZ is better configured in its south position (Cavalcanti et al., 2009). Also is important to say that most of SL moved from NE to SW (Figs. 4.1 and 4.2) as already noted by Garstang et al. (1994). Other common characteristic between the two SLs types is the time of formation along the coast around or after local noon (15:00 UTC), as found by Cohen et al (1995).

Otherwise, the majority of SLs found in this work formed at north of northeast region of Brazil, which can be related with interannual variability of these systems. According to Cavalcanti et al. (2009), in El Niño years, the SLs tend to form a little north of its average position, and in La Niña years, a little south, in the north and northeast of Brazil. According to the Oceanic Niño Index (ONI), the period from November 2014 to April 2016 was characterized as of El Niño activity, which comprises the period of the present study.

## 4.2. SELECTED SQUALL LINES

Of the 21 SLs identified, were selected two for description and analysis of Lorenz energy, one CSL and one ASL. These SLs were selected since they were realistically represented by GFS analysis, they have GFS data available for all the times, and represent the average behavior of the energetic terms of the two SL types. The mean values of energetic terms of all CSLs and ASLs chosen in this work are in the appendix.

The CSL started approximately at 13:00 UTC 27 April and ended at 13:00 UTC 28 April 2014. The ASL occurred from 16:00 UTC 06 May to 18:00 UTC 07 May 2015. The black lines in the Figures 4.1 (CSL) and 4.2 (ASL) show the displacement of these two SLs.

## 4.2.1. SATELLITE IMAGERY

According to satellite images (Fig. 4.3), the CSL started as an isolated convection over Marajó Island, located in northeast of Pará, at 13:00 UTC 27 April 2014 and after 5 hours the system was organized as SL affecting a large area of the north-northeast of Brazil (Pará, Maranhão and Piauí states). At 00:00 UTC 28 April, the SL advanced southwestward and it covered all the north and northeast of Pará and the north-center of Maranhão. In the next 3 hours, the SL practically did not move suffering a weakening over Pará and intensifying over Maranhão. At 09:00 UTC 28 April, the system moved southward and it is located over the center of Pará and south of Maranhão. At 13:00 UTC the CSL has dissipated.
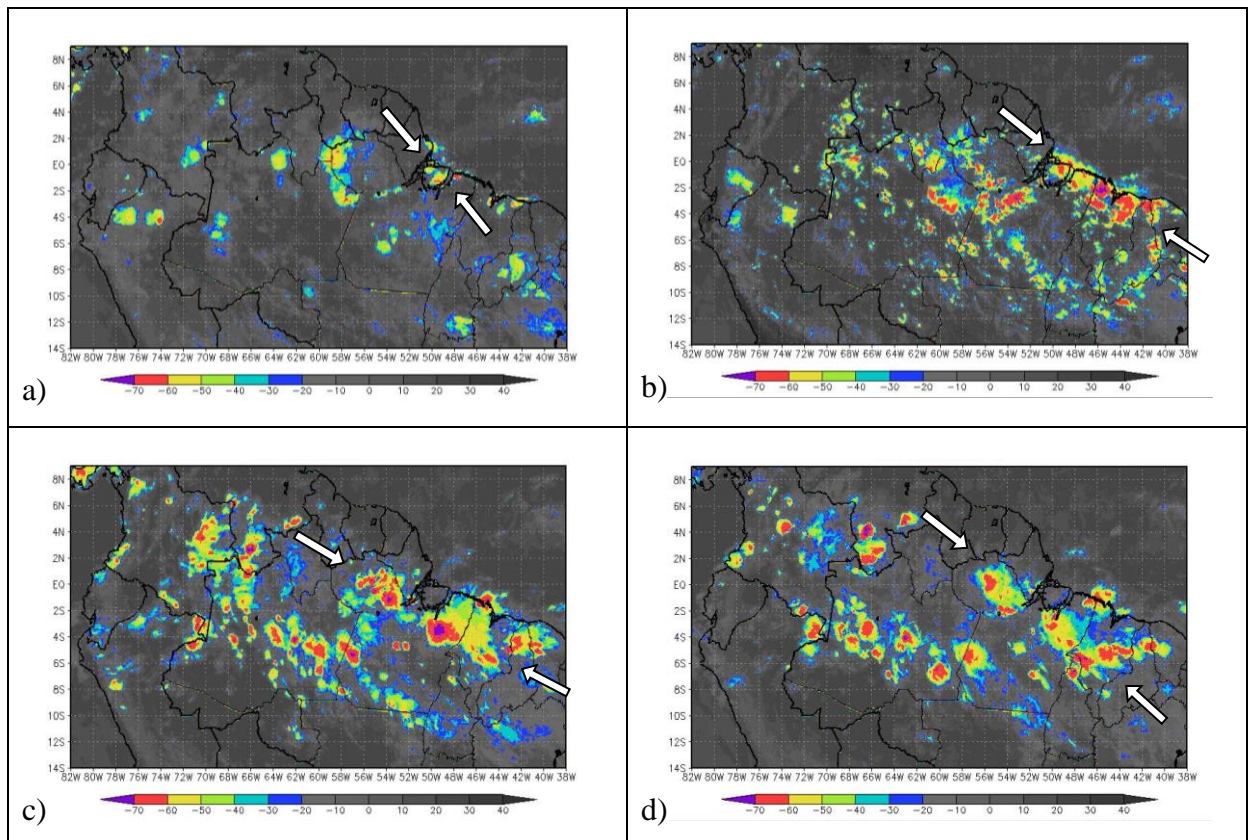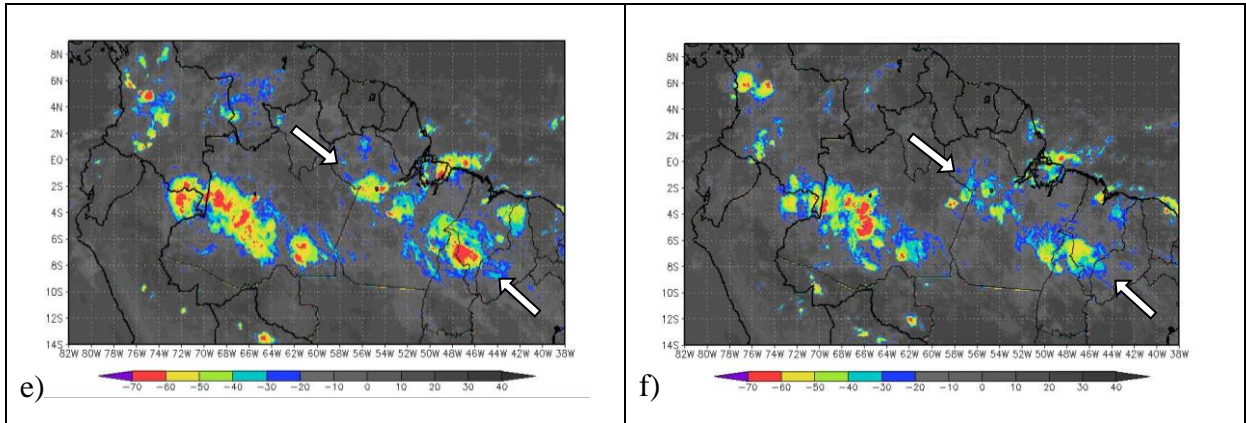
Figure 4.3 - Infrared satellite imagery for the CSL event. (a) 13:00 UTC, (b) 18:00 UTC 27 April, (c) 00:00 UTC, (d) 03:00 UTC, (e) 09:00 UTC and (f) 12:00 UTC 28 April 2014.

The satellite imagery in Figure 4.4 revels the ASL life cycle, which started at 18:00 UTC 06 May 2015 as a set of cumulonimbus clouds over Marajó Island (Pará) and south of Amapá. In the 3 hours after the convective activity was organized as SL covering the northeast of South America (Suriname and French Guiana countries, Amapá, Pará, and Maranhão states). At 03:00 UTC 07 May, the SL presented very intense convective activity and advanced southwestward, while its strongest associated convection was over the north of Pará. The ASL continued to move westward and at 06:00 UTC 07 May was covering northwest of Pará, south of Roraima and Guyana. In the next 6 hours, at 12:00 UTC 07 May, the ASL was yet displacing to west and it covered all Roraima and arrived at Amazonas. At 18:00 UTC the ASL was located in similar position of 6 hours before and it was dissipating.
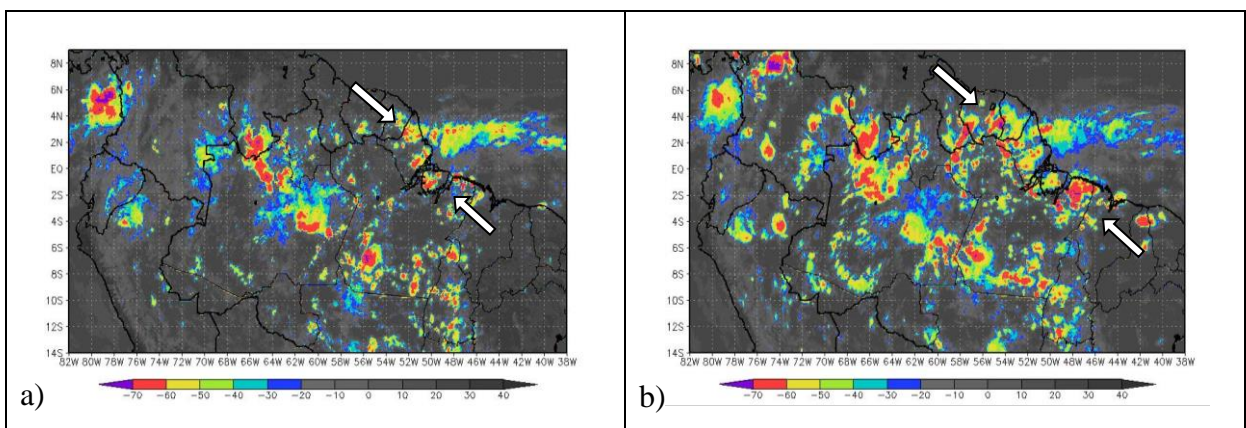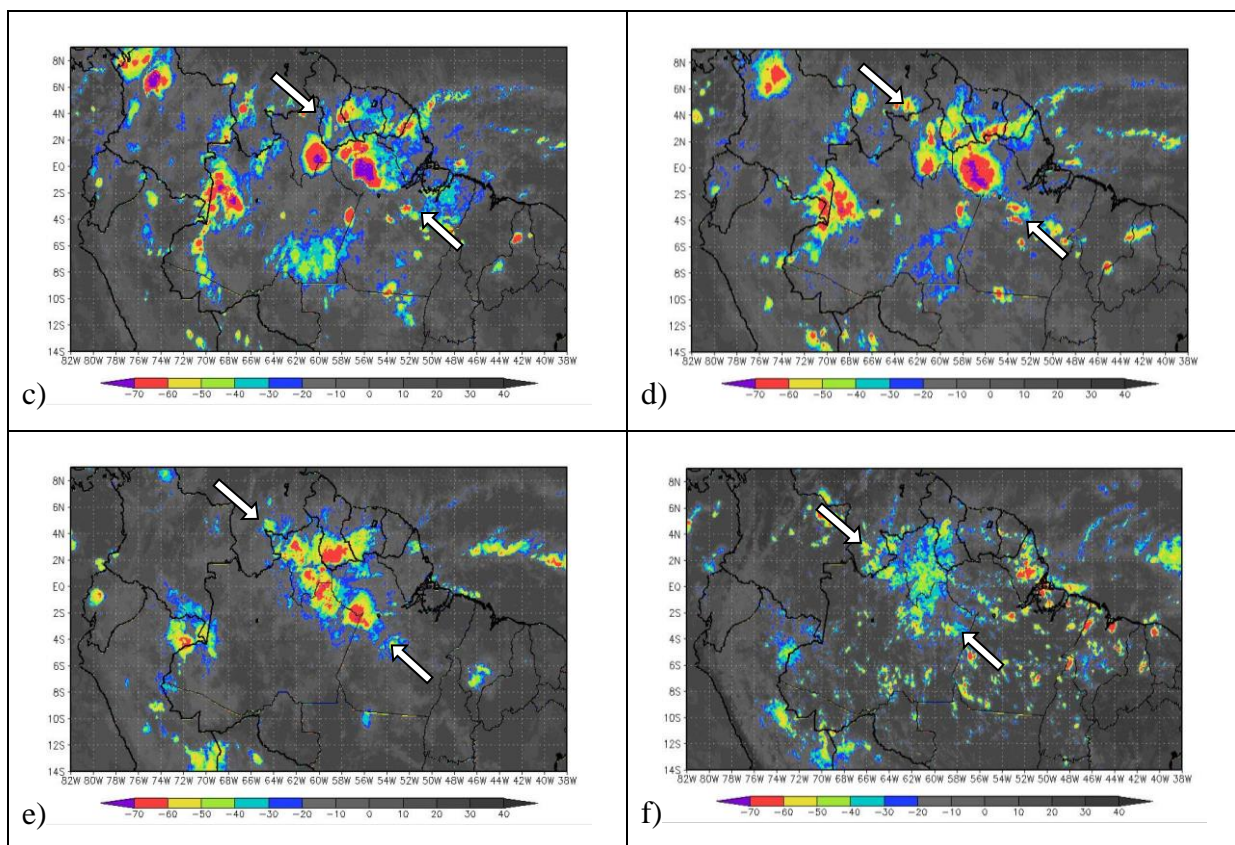
Figure 4.4 - Infrared satellite imagery for the ASL event. (a) 18:00 UTC, (b) 21:00 UTC 06 May, (c) 03:00 UTC, (d) 06:00 UTC, (e) 12:00 UTC and (f) 18:00 UTC 07 May 2015. Values are in °C.

### 4.2.2. TRMM AND GFS PRECIPITATION

Figs. 4.5 and 4.6 present, respectively, for CSL and ASL events, the time evolution of the intensity of the precipitation estimated by TRMM. The red boxes represent the areas of SL identified in satellite imagery in the same horary of TRMM estimation.

The precipitation estimated by TRMM coincides with the cloudiness observed in satellite imagery. Therefore, at 12:00 UTC 27 April 2014 (Fig. 4.5a), as shown in Figure 4.3a, the precipitation was over Marajó Island, and at 18:00 UTC 27 April (Fig. 4.5b) the system was formed as SL over the north-northeast of Brazil. Then it began to move southwestward (Figs. 4.5c-e) to dissipate over Pará at 12:00 UTC 28 April 2014 (Fig. 4.5f).
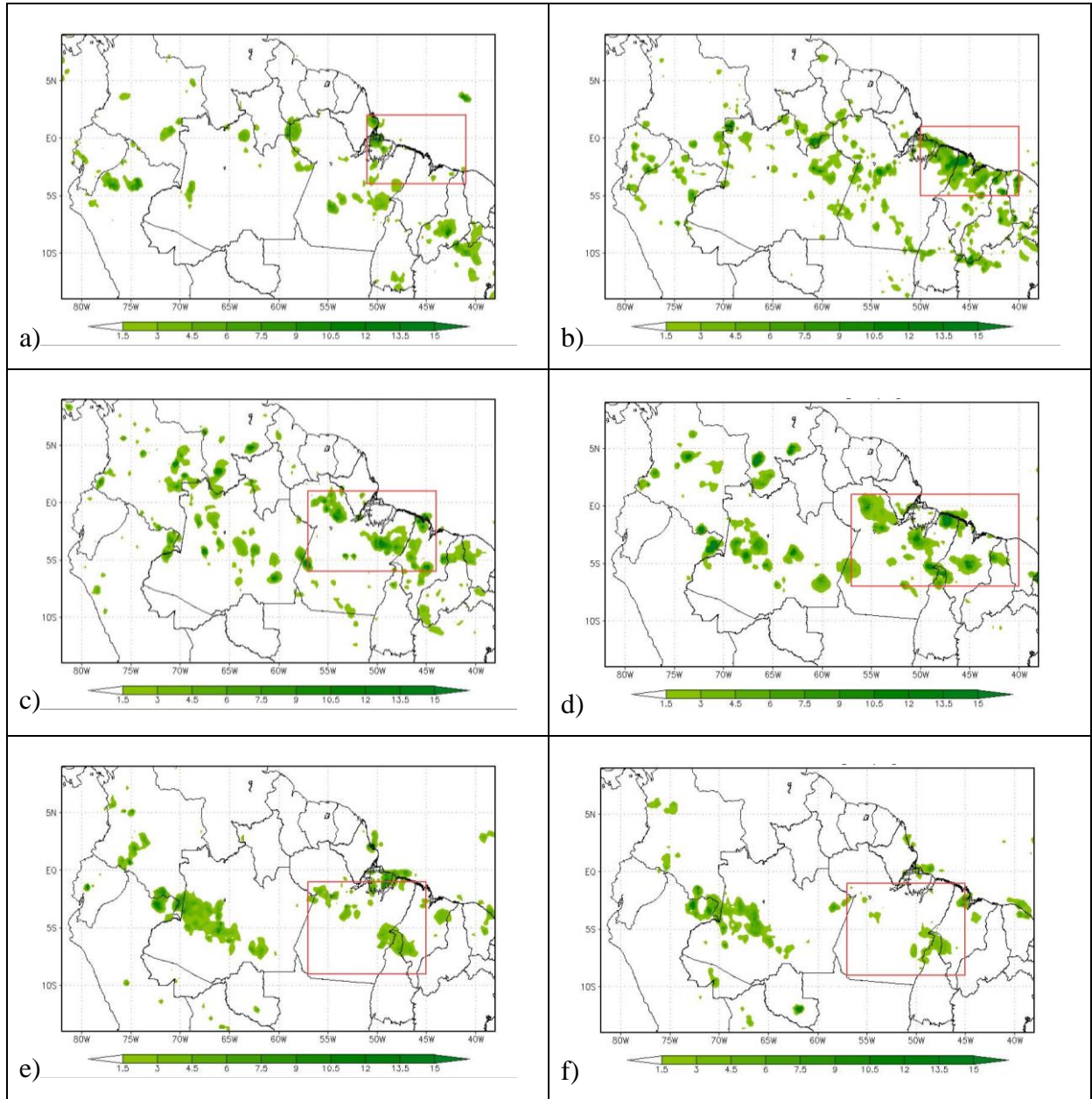
Figure 4.5 - TRMM estimated precipitation for the CSL at: (a) 12:00 UTC, (b) 18:00 UTC 27 April, (c) 00:00 UTC, (d) 03:00 UTC, (e) 09:00 UTC and (f) 12:00 UTC 28 April 2014. Values are in mm h$^{-1}$. Red boxes represent the locations of SLs identified in satellite imagery.

The precipitation estimated by TRMM in ASL event shows the formation of the SL over Marajó Island and Amapá at 18:00 UTC 06 May 2015 (Fig. 4.6a) and its southwestern displacement and intensification until 06:00 UTC 07 May (Fig. 4.6d) when it is localized over northwest of Pará and south of Guyana. At 12:00 UTC 07 May (Fig. 4.6e), the ASL intensity was diminishing until its dissipation at 18:00 UTC 07 May (Fig. 4.6f).
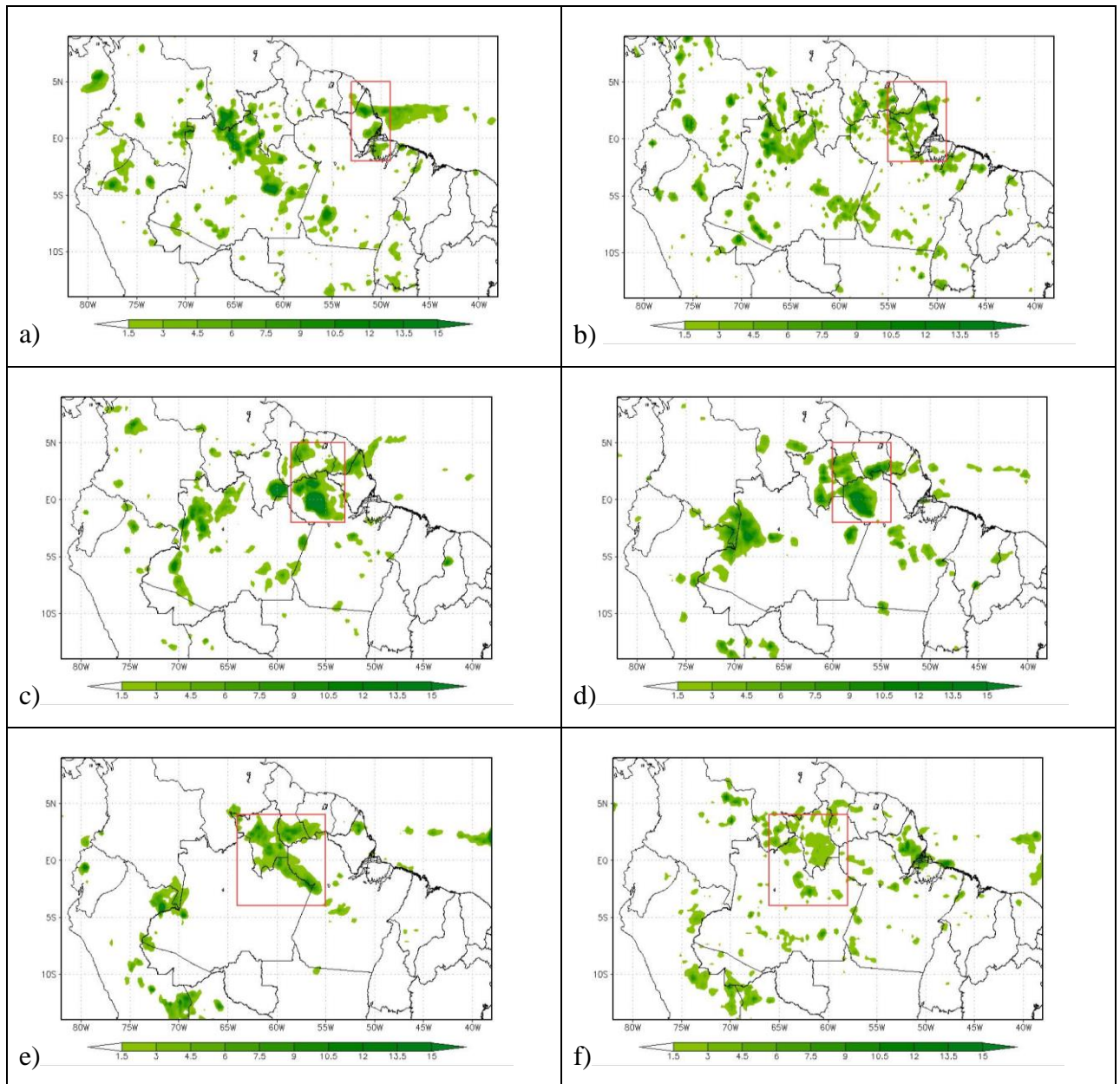
Figure 4.6 - TRMM estimated precipitation for the ASL at: (a) 18:00 UTC, (b) 21:00 UTC 06 May, (c) 03:00 UTC, (d) 06:00 UTC, (e) 12:00 UTC and (f) 18:00 UTC 07 May 2015. Values are in mm h^{-1}. Red boxes represent the locations of SLs identified in satellite imagery.

Of the 21 SLs selected with the imagery satellite, only in nine it is found that GFS analysis was able to reproduce the associated precipitation. This selection was necessary based in the fact that if GFS analysis does not reproduce adequately all SLs systems, the LEC would provide wrong information or false results concerning their energetic. The nine SL events captured by GFS analysis are listed in the Table 4.4.

Table 4.4 – List of SLs where GFS analysis reproduces the observed precipitation between April and August 2014 and 2015.

| Date | Type | Approx. duration (h) | Approx. inland propagation (km) | Propag. speed (m s$^{-1}$) |
|---|---|---|---|---|
| 31 Mar – 02 Apr 2014 | **ASL\*** | 48:30 | 3221 | 18,4 |
| 27 – 28 Apr 2014 | CSL | 24:00 | 755 | 8,7 |
| 28 – 29 Jun 2014 | **ASL** | 17:30 | 1535 | 24,7 |
| 31 Mar – 01 Apr 2015 | CSL | 11:30 | 389 | 9,4 |
| 11 – 13 Apr 2015 | **ASL\*** | 49:00 | 2887 | 16,4 |
| 17 – 18 Apr 2015 | CSL | 19:00 | 969 | 14,2 |
| 22 – 23 Apr 2015 | CSL | 21:00 | 923 | 12,2 |
| 06 – 07 May 2015 | **ASL** | 26:00 | 1226 | 13,1 |
| 24 – 25 Jul 2015 | CSL | 12:00 | 613 | 14,2 |

\*ASLs that reached the Peruvian Amazon.

Figures 4.7 and 4.8 show the 6 hours accumulated precipitation of GFS in CSL and ASL, respectively. As shown in the Figure 4.7a, the precipitation accumulated from 12:00 UTC to 18:00 UTC 27 April 2014 had maximum values of 30 mm and was localized over the northeast of Pará and the north of Maranhão and Piauí (Brazilian states). After 6 hours, at 00:00 UTC 28 April (Fig. 4.7b) the precipitation accumulated signalized the location of the SCL at north of Pará. In the 06 hours after, at 06:00 UTC 28 April (Fig. 4.7c), the system of precipitation had maximum values of 50 mm and continued over the north of Pará with southwestern displacement until its dissipation at 12:00 UTC 28 April (Fig. 4.7d).
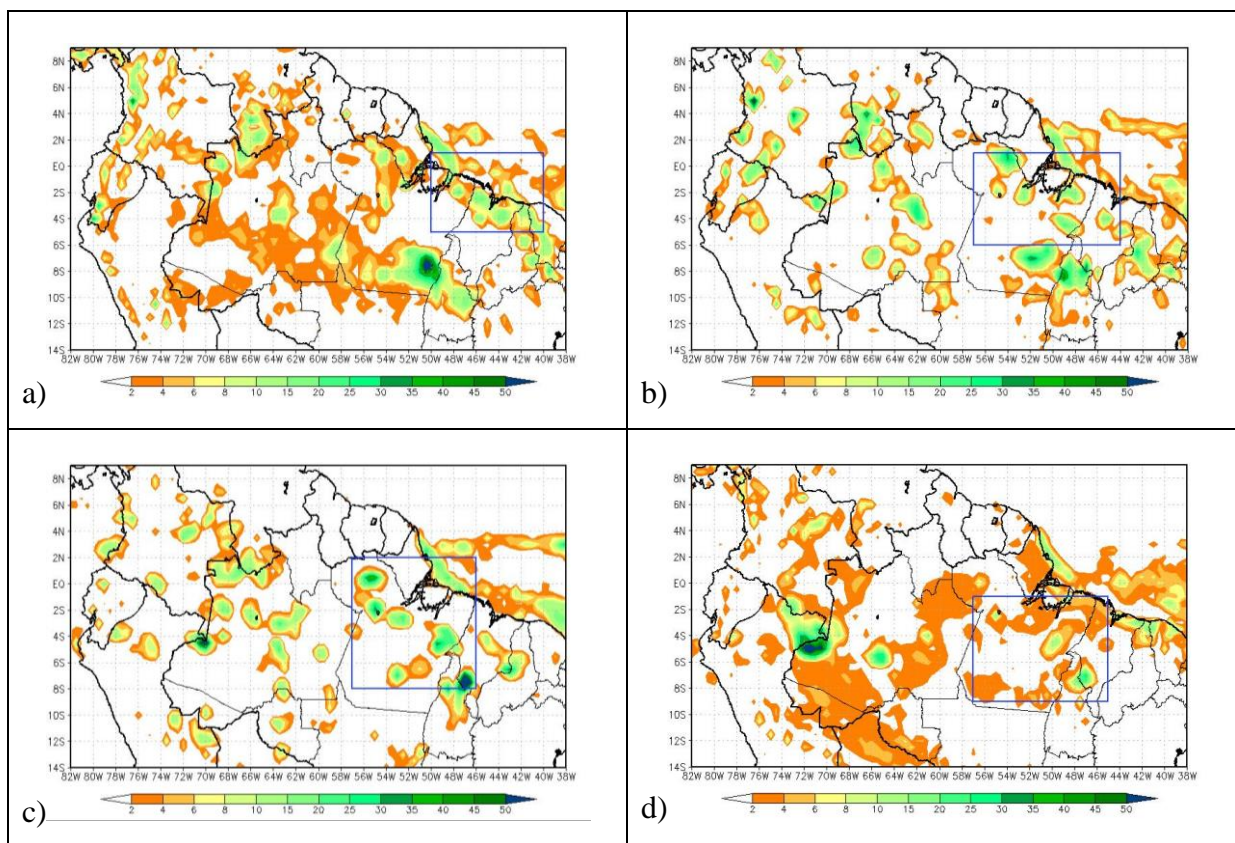
Figure 4.7 - GFS 6h accumulated precipitation of the CSL at: (a) 18:00 UTC 27 April, (b) 00:00 UTC, (c) 06:00 UTC and (d) 12:00 UTC 28 April 2014. Values in mm/6h. Blue boxes represent the locations of SLs identified in satellite imagery.

Figure 4.8a shows the accumulated precipitation from 18:00 UTC 06 May to 00:00 UTC 07 May 2015 with maximum values of 50 mm over northwest of Pará. After 6 hours, at 06:00 UTC 07 May (Fig. 4.8b) the accumulated precipitation with maximums of 50 mm remained on northwest of Pará and south of Guyana and southeast of Roraima. At 12:00 UTC 07 May (Fig. 4.8c), the accumulated precipitation covered all Roraima and remained over northwest of Pará and south of Guyana. The precipitation accumulated from 12:00 UTC to 18:00 UTC 07 May (Fig. 4.7d) showed the dissipation of the ASL.
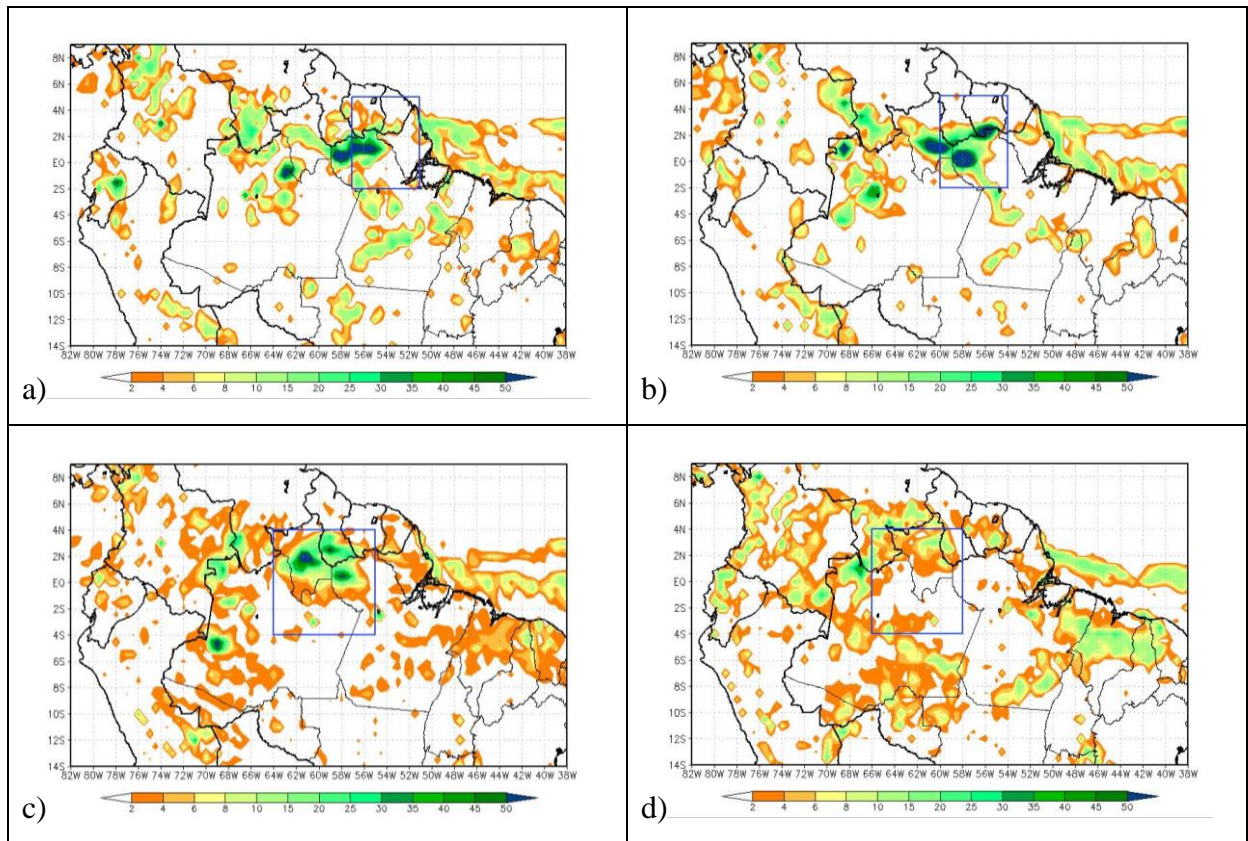
Figure 4.8 - GFS 6h accumulated precipitation of the ASL at: (a) 00:00 UTC, (b) 06:00 UTC, (c) 12:00 UTC and (d) 18:00 UTC 07 May 2015. Values in mm/6h. Blue boxes represent the locations of SLs identified in satellite imagery.

## 4.2.3. SYNOPTIC ANALYSIS

The Figure 4.9 presents the streamlines and wind intensity at 250 hPa. Analyzing the jet stream at 250 hPa in the CSL and ASL events, the principal difference found was the weaker wind in CSL than in ASL. For ASL case, the more intense wind was associated to two anticyclonic systems, one over the North Hemisphere (NH), centered in 7°N-60°W, and the other in the South Hemisphere (SH), centered in 10°S-52°W. The locations of these systems contributed to intensify the easterly wind near the Equator, which accompanied and favored the westward displacement of ASL event (Figs. 4.9c and 4.9d). This configuration of two anticycloninc systems, one at each side of the equator, also was found by Cohen et al. (1995) in the SL of May 1987, but displaced to the west.

42
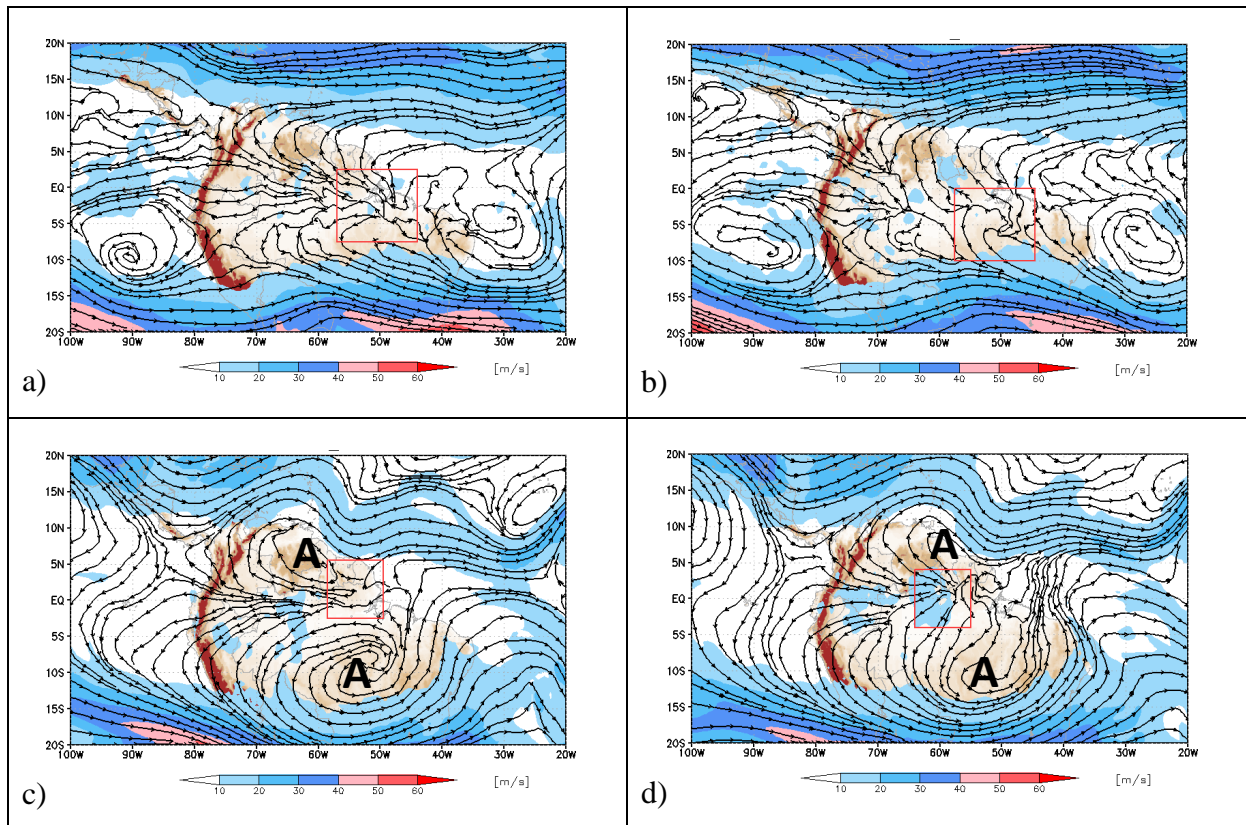
Figure 4.9 - Streamlines (black lines with arrows) and wind speed (shaded in m s$^{-1}$) at 250 hPa for CSL event at: a) 00:00 UTC and b) 12:00 UTC 28 April 2014, for ASL event at: c) 00:00 UTC and d) 12:00 UTC 07 May 2015. The red boxes represent the areas considered in the quasi-Lagrangian approach.

To analyze the relation between divergence in upper levels – convergence in lower levels, Figure 4.10 presents the divergence at 250 hPa and the convergence together streamlines at 850 hPa.

Both SCL and ASL events were associated with divergence at upper levels, but in low-levels, the wind convergence and confluence were more intense in the ASL than in CSL. The wind at 850 hPa in ASL area was only easterly, but in CSL had a northerly component associated with the anticyclonic circulation at low-levels configured over Brazil.
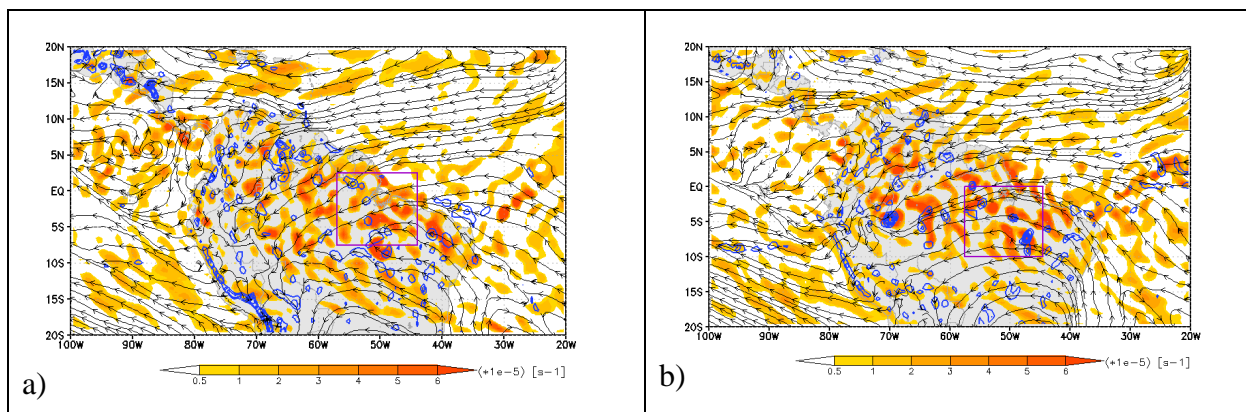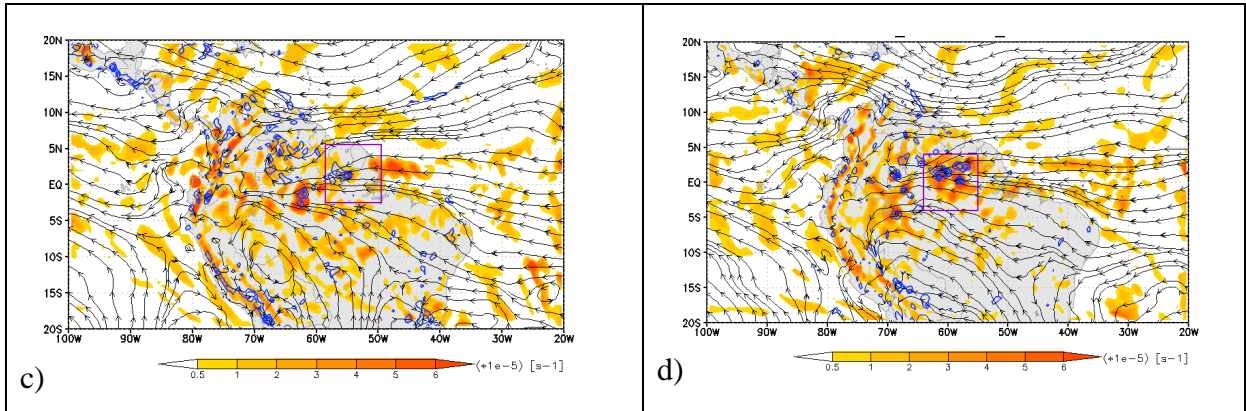
Figure 4.10 - Streamlines (black lines) and convergence (contour blue lines) at 850 hPa, divergence (shaded x10-5 s-1) at 250 hPa for CSL event at: a) 00:00 UTC and b) 12:00 UTC 28 April 2014, for ASL event at: c) 00:00 UTC and d) 12:00 UTC 07 May 2015. The boxes represent the areas considered in the quasi-Lagrangian approach.

In the proximity of the CSL and ASL events, the wind and the relative vorticity at 500 hPa were similar, as shown in Figure 4.11. In both SLs it was noted the presence of one inverted trough with cyclonic vorticity in its axis (negative in CSL because it developed in Southern Hemisphere-SH, while positive in ASL because it developed in Northern Hemisphere-NH).The anticyclonic systems in the SH observed at 250 hPa also were observed at 500 hP in ASL event (Figs. 4.11c and 4.11d).
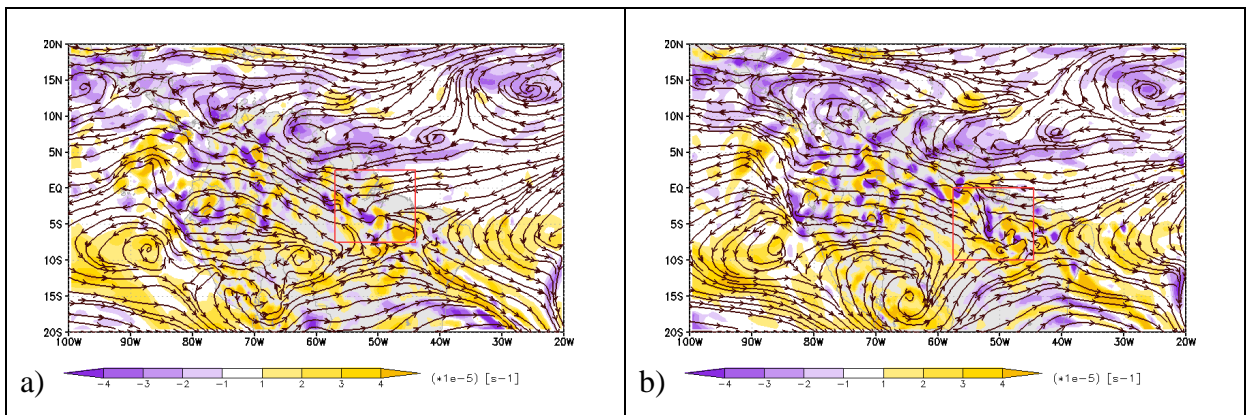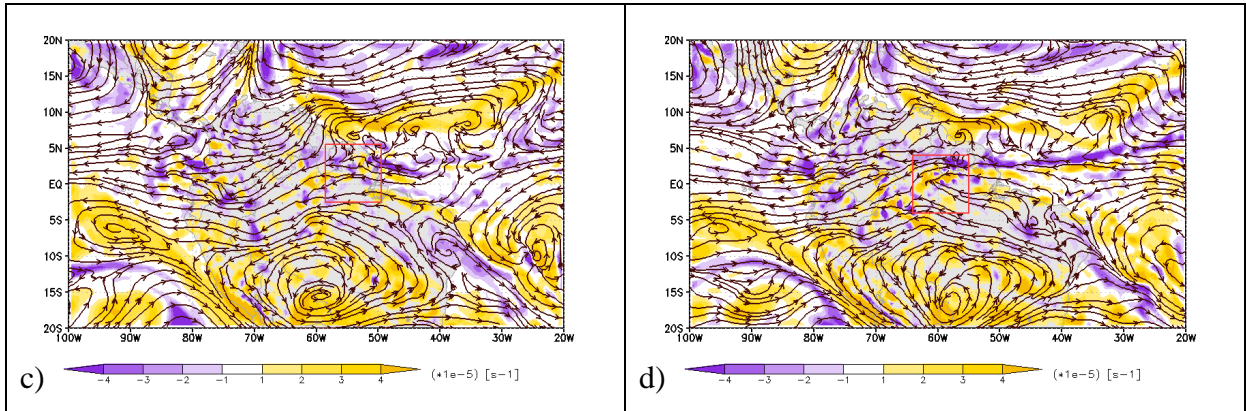
Figure 4.11 - Streamlines (brown lines) and relative vorticity (shaded x 10-5 s-1) at 500 hPa for CSL event at: a) 00:00 UTC and b) 12:00 UTC 28 April 2014, for ASL event at: c) 00:00 UTC and d) 12:00 UTC 07 May 2015. The boxes represent the areas considered in the quasi-Lagrangian approach.

The thickness in 850-1000 hPa layer and the wind at 925 hPa had clear differences in CSL and ASL. While the CSL was developing (Figs. 4.12a and 4.12b), a cold system was approaching from the south by the east side of SA and imposed southerly winds, which converged with the northeasterly winds in the CSL area. In the area of development of the ASL can be observed deeper 850-1000 hPa layer than in CSL, which is related to higher temperature (Figs. 4.12c and 4.12d). This could explain the regeneration of new convective cells and the larger inland displacement in the ASL due to atmospheric instability related to the higher temperature.
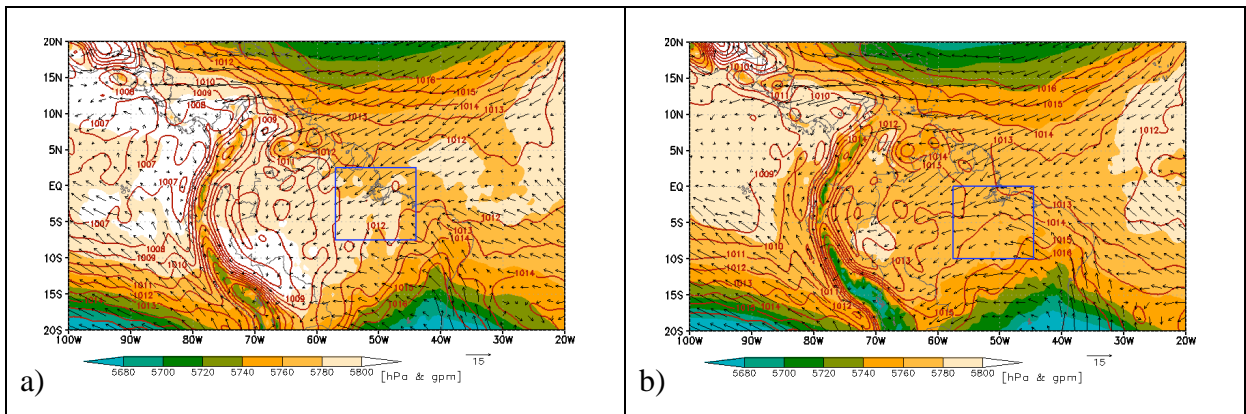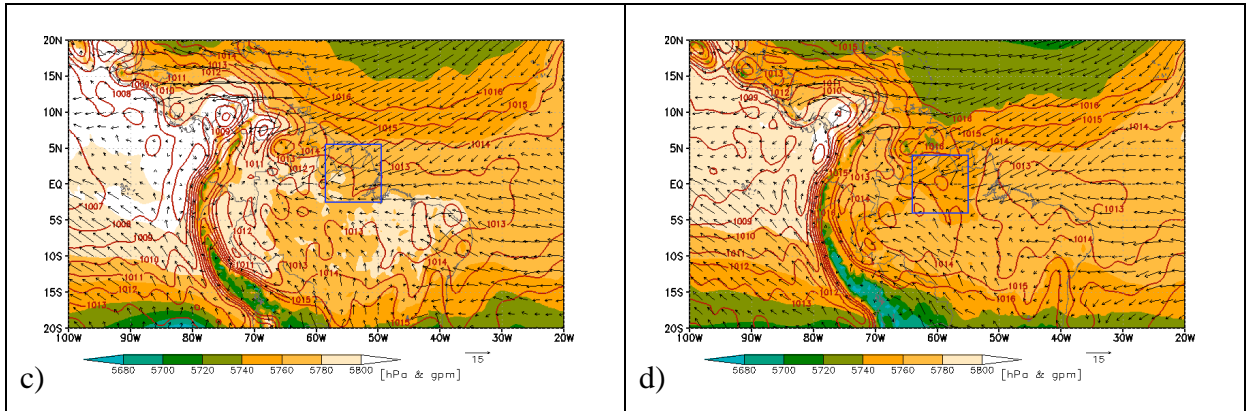
Figure 4.12 - Mean sea level pressure (red lines in hPa) and thickness between 850-1000 hPa layer (shaded gpm) for CSL event at: a) 00:00 UTC and b) 12:00 UTC 28 April 2014, for ASL event at: c) 00:00 UTC and d) 12:00 UTC 07 May 2015. The boxes represent the areas considered in the quasi-Lagrangian approach.

From Figure 4.13 it is clear that during the ASL development there was higher moisture flux convergence than during the CSL and the wind convergence was also more intense at 850 hPa (Fig. 4.10) in ASL than in CSL.
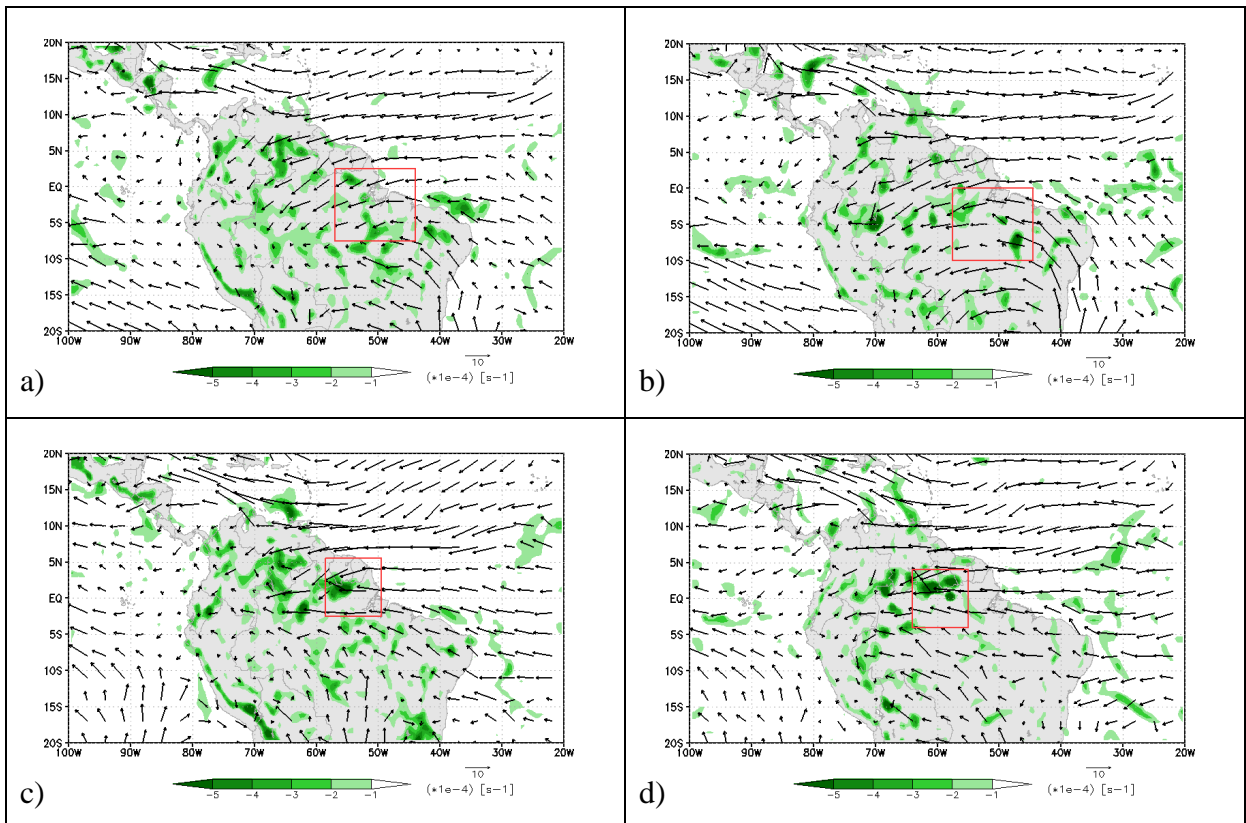


Figure 4.13 - Wind (vectors) and moisture flux divergence (shaded x10⁻⁴ in g kg⁻¹ s⁻¹) at 850 hPa for CSL event at: a) 00:00 UTC and b) 12:00 UTC 28 April 2014, for ASL event at: c) 00:00 UTC and d) 12:00 UTC 07 May 2015. The boxes represent the areas considered in the quasi-Lagrangian approach.

In ASL, the vertical wind speed shear in 700-850 hPa layer accompanied all its developing and it was higher than in CSL (Fig. 4.14). The wind speed shear was calculated by the difference of wind speed between 700 and 850 levels. According to Rotunno et al. (1988) the vertical shear is the principal factor for new convective cells generation and it also contributes to the SL displacement. According to LeMone et al. (1998) the orientation of the primary convective band is determined by the shear in the low-levels layer. The areas of upward motions at 700 hPa, represented by the pseudo-vertical velocity omega, allowed a clear identification of both SLs as shown in Figure 4.14. The winds at 700 hPa showed a belt with intense values near the Equator, between $20°$ to $65°W$, in both SL events, as found by Cohen et al. (1995) in a SL of May 1987. This wind belt was more intense in ASL than in SCL, and since the ASL was organized over the Equator, compared to CSL that was further south, the wind belt contributed to its westward propagation.
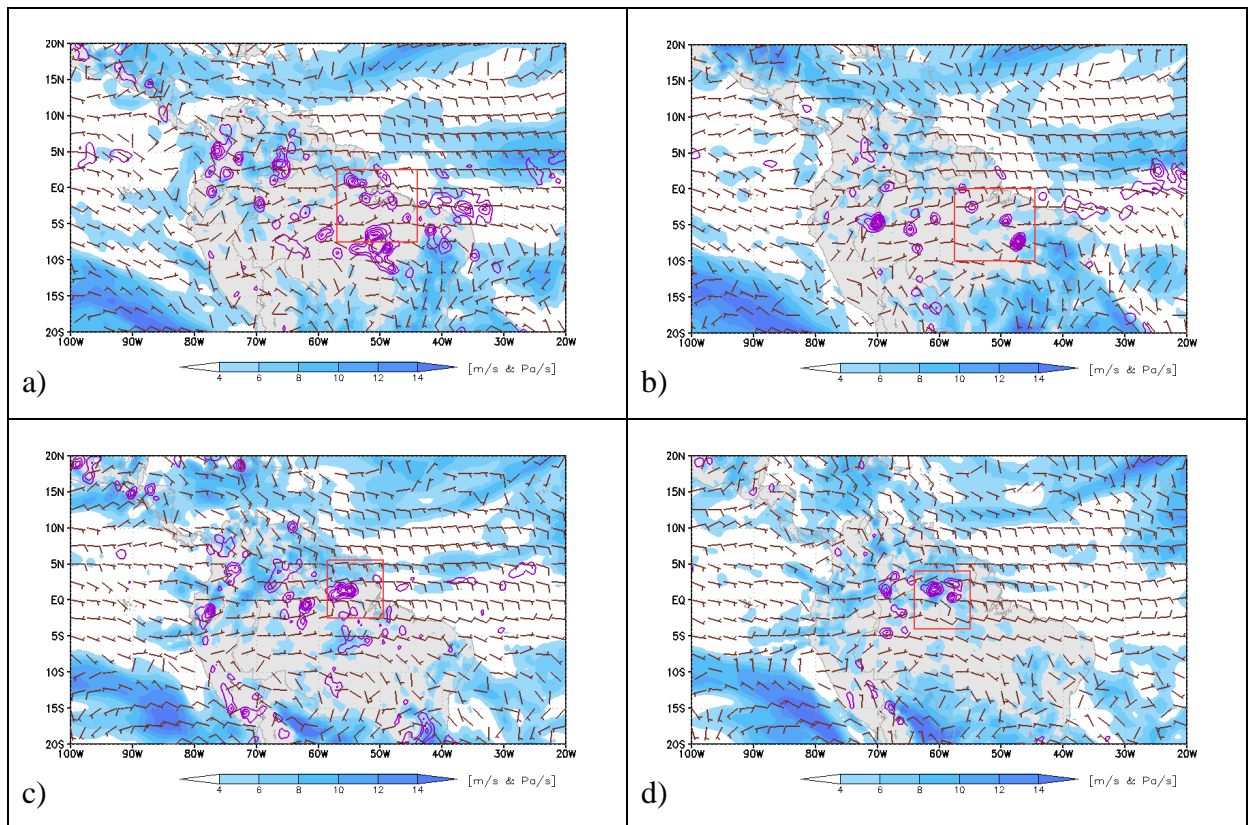


Figure 4.14 - Vertical wind speed shear between 700-850 hPa layer (shaded in m s^{-1}), wind (barbs in m s^{-1}), and negative values pseudo-vertical velocity, omega, (purple contour in Pa s^{-1}) at 700 hPa. For CSL event at: a) 00:00 UTC and b) 12:00 UTC 28 April 2014. For ASL event at: c) 00:00 UTC and d) 12:00 UTC 07 May 2015. The boxes represent the areas considered in the quasi-Lagrangian approach.

As presents the Figure 4.15, the vertical profiles of the horizontal wind presented a clear difference between CSL and ASL. In the upper level, in most of the time southerly wind was

found in CSL event, while northerly wind predominated for ASL. This agrees with the work of Oliveira and Oyama (2015), who found northerly wind for SL category (SLC) and southerly wind for no convection category (NOC). In addition, at upper levels westerly and/or weak easterly winds was noted in the CSL, while in ASL during all it lifecycle it was found only easterly winds (Fig. 4.15). This provides more favorable environment to the westward propagation of the ASL and it is according to the presence of a maximum of wind (Fig. 4.9), but it is in disagreement with the works of Cavalcanti et al. (2009) and Cohen (1996). For SL with large propagation, these works showed the presence of westerly and easterly winds, at upper and lower levels, respectively, forming a duct for propagation of gravity waves favoring the westward movement of the SL. However, considering only the wind speed, in this study two maximum wind velocity were observed, one at upper levels and the other at low-levels, which formed the propagation duct in the ASL. From low to mid-levels, the Figure 4.15 presents easterly winds, which is according to Cohen et al. (1995) and Alcantara et al. (2011) observational study about SLs. From Figure 4.15, an easterly low-level jet was situated around 700 hPa and it was stronger in ASL than in CSL event.
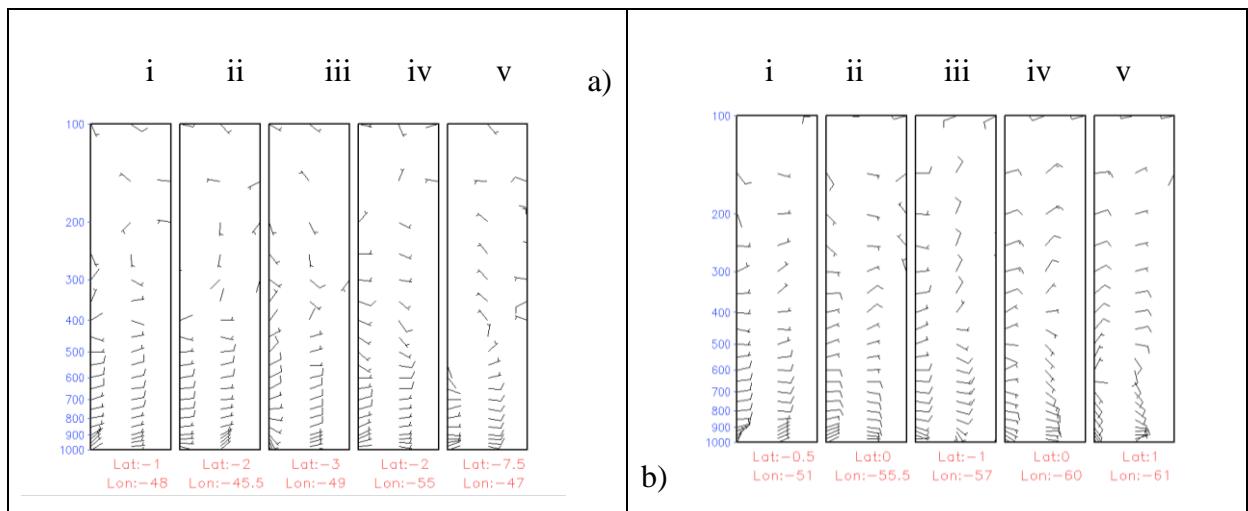


Figure 4.15 - Vertical profile of the horizontal wind in the points with maximum convection. **a) CSL** (i.12:00 UTC, ii.18:00 UTC 27 April, iii.00:00 UTC, iv.06:00 UTC and v.12:00 UTC 28 April 2014). **b) ASL** (i.18:00 UTC 06 May, ii.00:00 UTC, iii.06:00 UTC, iv.12:00 UTC and v.18:00 UTC 07 May 2015).

With respect to the vertical wind shear, Figure 4.15 shows directional shear at upper levels for CSL, a feature that may difficult its westward displacement. For ASL event, the more vertical speed shear in low-levels may help to explain the continuous generation of new convective cells according to RKW theory (Rotunno et al.1988). It is important to mention that according to Alcantara et al. (2014) there should be no directional shear in lower levels

for the formation of a SL and it was observed in both profiles.

Figures. 4.16 and 4.17 show the atmospheric soundings of selected stations where CSL and ASL, respectively, passing over the stations presented in Figure 3.1



c)
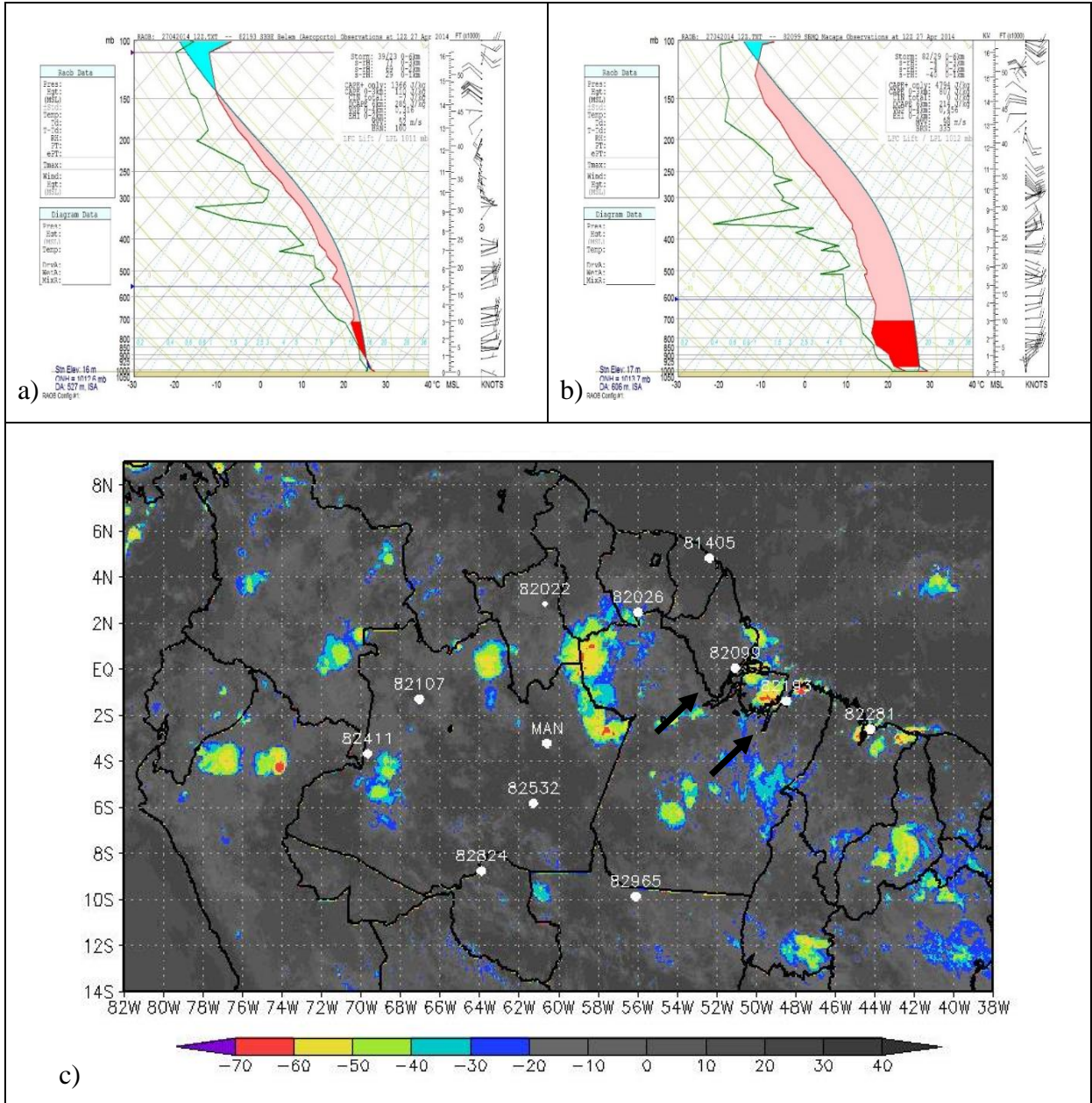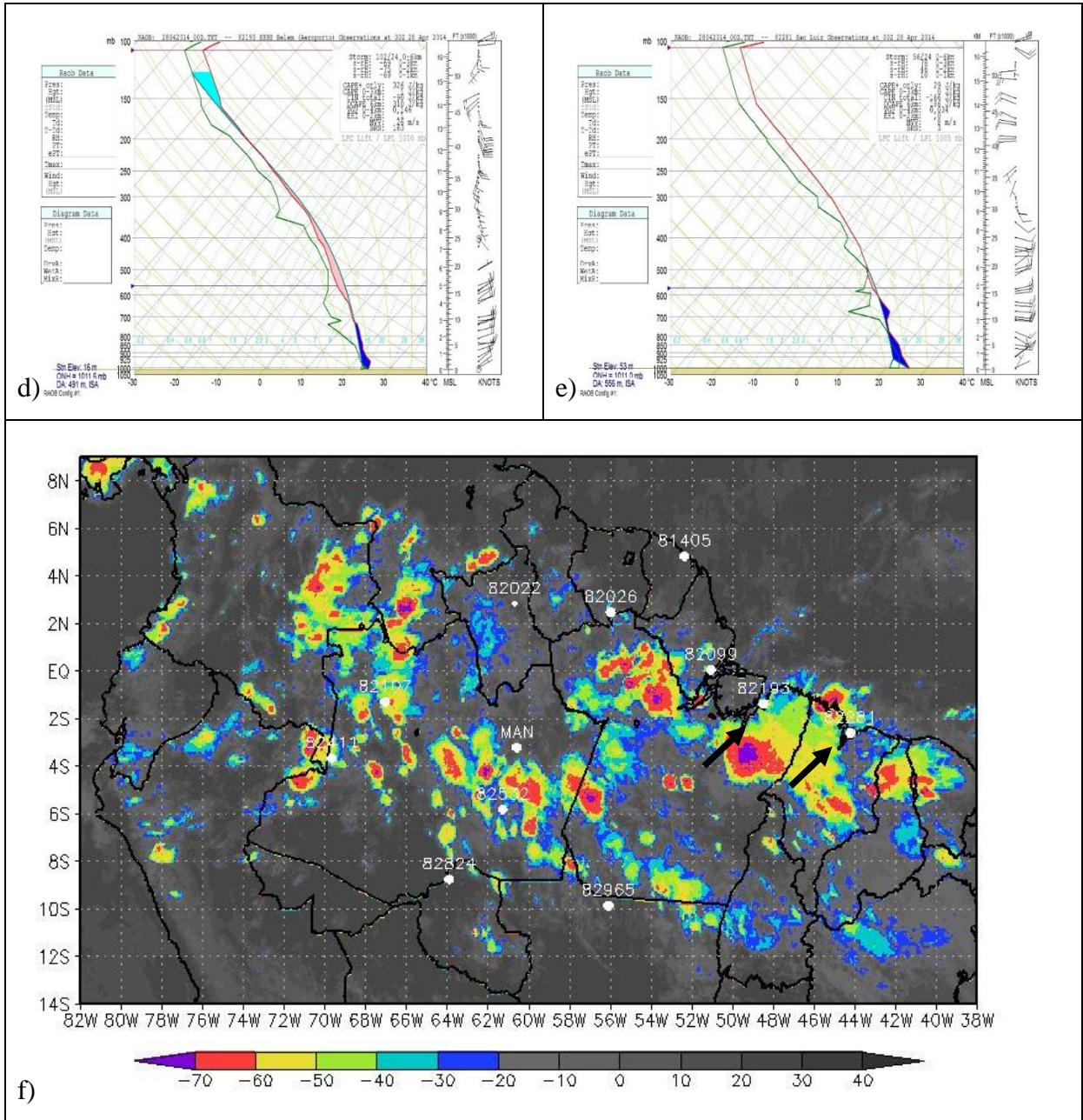
Figure 4.16 - Soundings of CSL in: a) **82193** station at 12:00 UTC, b) **82099** station at 12:00 UTC 27, d) **82193** station at 00:00 UTC and e) **82281** station at 00:00 UTC 28 April 2014. Satellite images at c) 13:00 UTC 27 April and f) 00:00 28 April 2014. The black arrows indicate the stations considered because the SL is over them at that time.

For the initial phase of CSL the soundings in Figure 4.16(a)-(b), show high values of CAPE (higher than 1000 J kg$^{-1}$, which is in general assigned as the minimum value for the storm occurrence), mainly over Macapa (82099). The soundings in Figure 4.16(d)-(e) are not precisely on the CSL core, but they are over the anvil region. Thus, these soundings do not have high CAPE, but they are quasi-saturated (dew point and air temperature are close) in all vertical structure of the troposphere.

50
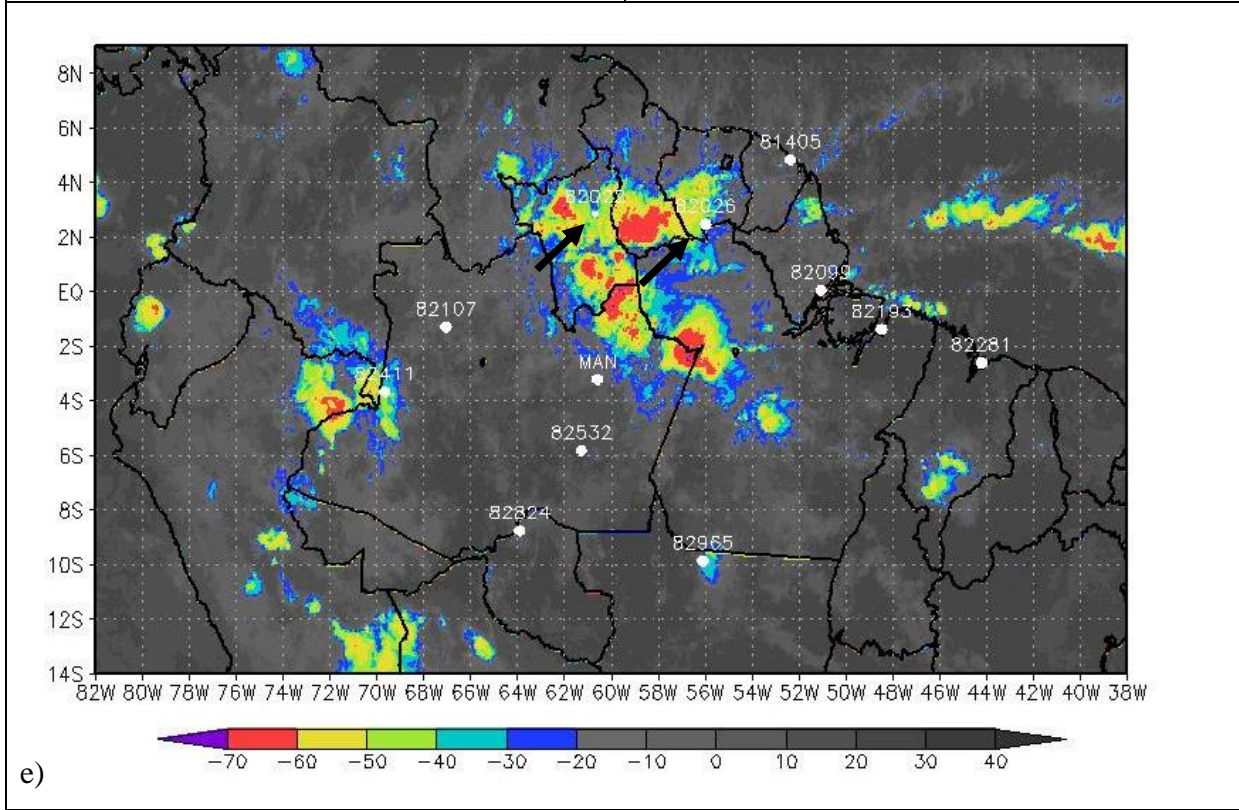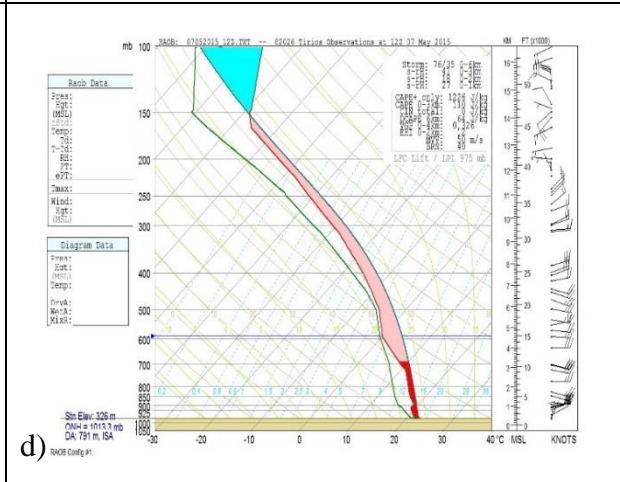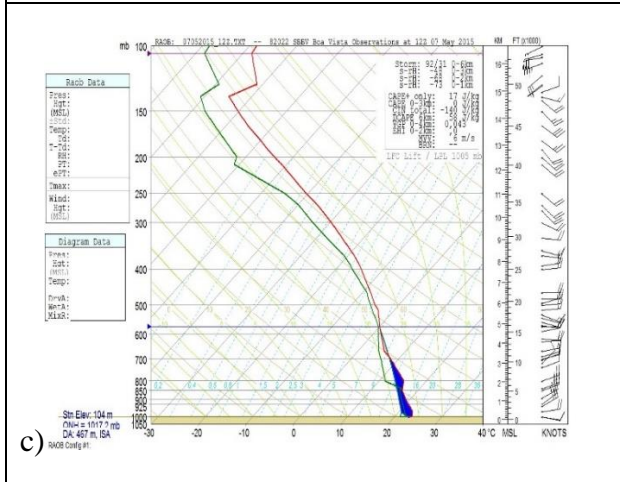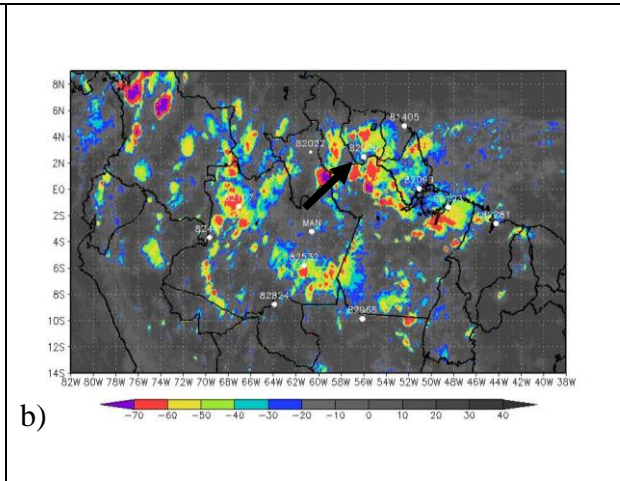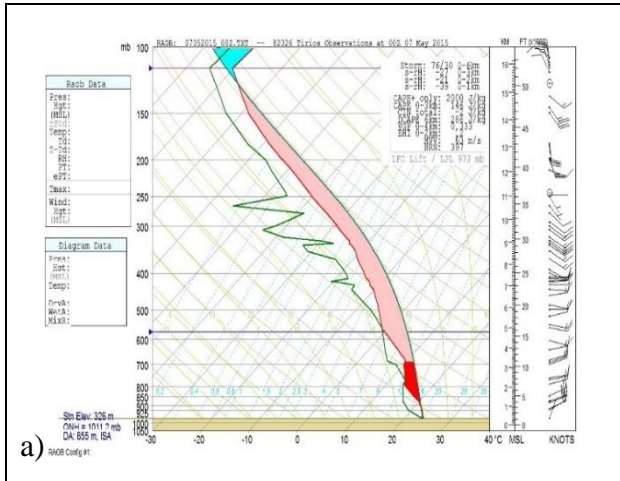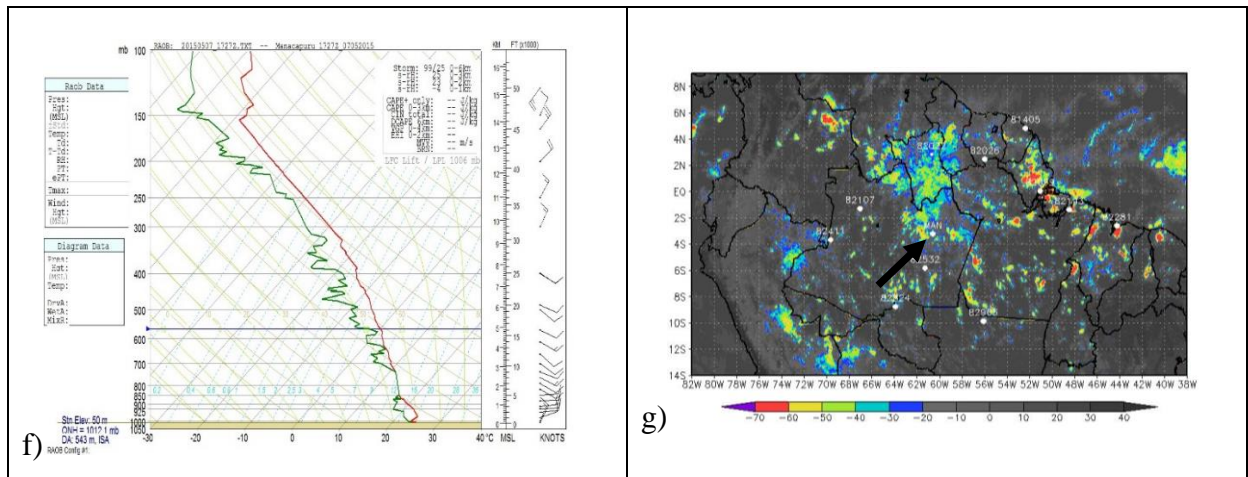
Figure 4.17 - Soundings of ASL in: a) **82026** station at 00:00 UTC, c) **82022** station at 12:00 UTC, d) **82026** station at 12:00 UTC and f) **MAN** station at 18:00 UTC 07 May 2015. Satellite images at b) 00:00 UTC, e) 12:00 UTC and g) 18:00 UTC 07 May 2015. The black arrows indicate the stations considered because the SL is over them at that time.

For ASL event, there were no sounding coinciding with its positions, but Figure 4.17 presents those that were close to the event. The sounding at 00:00 UTC 07 May 2015 (Fig. 4.17a) showed higher CAPE compared with the other soundings. The soundings in 82022 and 82026 stations for 12:00 UTC 7 May (Figs. 4.17c and 4.17d) were quasi-saturated in all tropospheric column since at this time the soundings are over the anvil region of the ASL. At 18:00 UTC 07 May, which corresponds to the dissipation time, the sounding of Manacapuru (Fig. 4.17f) showed the 750-850 hPa layer saturated, while the levels above were quasi-saturated.

Regarding the winds, in the CSL easterly winds predominated between the surface and 300 hPa level, with maximum values at low-levels (700-850 hPa layer) and perpendicular to the coast line (Fig. 4.16), as found by Cohen et al. (1995), while above the 300 hPa the winds were from west. On the other hand, in the ASL easterly winds occupied the whole tropospheric column and westerly winds just occurred above the 150 hPa, which was already noted in previous synoptic analysis using GFS. This is an important difference between CSL and ASL. Other difference is the vertical depth of easterly low-level jet; in CSL it is smaller than in ASL. This is according to Alcantara (2010) and Alcantara et al. (2011), who concluded that a deeper easterly jet is necessary for existence of propagating SLs.

## 4.2.4. QUASI-LAGRANGIAN AND EULERIAN APPROACHES

Since Lagrangian and Eulerian approaches have advantages and disadvantages, in this work it was decided to calculate the LEC terms in both frameworks. This allowed a comparison between both approaches, but the quasi-Lagrangian approach was used instead the purely Lagrangian approach. The local derivatives of the energy components (Equations 3.30 – 3.36) were calculated only considering the Eulerian approach since for local derivative the area must be constant.

For quasi-Lagrangian scheme the volume considered was bounded by the 1000 and 70 hPa pressure surfaces in the vertical, and the horizontal boundaries moved following the position of the center of the system, but always keeping the same size in each SL event. For CSL, 5° meridional (latitude) and 6.5° zonal (longitude) distances from the center of the system, bounded the rectangular areas for each time. For ASL, areas were limited by 4° of latitude and 4.5° of longitude from the center. These limits were obtained considering the maximum distances in relation to the center in all the times of developing of the systems observed in the satellite imagery, as presented in Tables 4.5 and 4.6.

For Eulerian approach, the area considered was the same in all times for each SL event. The definition of these areas considered the northernmost and southernmost latitudes of all times in the quasi-Lagrangian scheme for their north and south limits, respectively. In the same way, the westernmost and easternmost longitudes were the limits to the left and right, respectively. This resulted in areas shown in Figure 4.18 for CSL and ASL event. In the Table 4.5 and 4.6 and in the Figure 4.18 are represented the systems centers each 6 hours for the two SL selected.

Table 4.5 – Limits and areas considered for quasi-Lagrangian and Eulerian energy calculations in CSL of 27-28 April 2014.

| Satellite Imagery | | | | | |
|---|---|---|---|---|---|
| Time UTC - 2014 | Center lat/lon | Meridional distance from the center (degrees) | Zonal distance from the center (degrees) | Area for quasi-Lagrangian calculation (5°lat and 6.5°lon away the center) | Area for Eulerian calculation |
| 12:00 27 Apr | -1/-46 | 3 | 5 | Lat: -6/**4**   Lon:-52.5/-39.5 | Lat: -10/4 |

| | | | | | |
|---|---|---|---|---|---|
| 18:00 27 Apr | -2/-45 | 3 | 5 | Lat: -7/3   Lon:-51.5/-**38.5** | Lon: -58/-38.5 |
| 00:00 28 Apr | -2.5/-50.5 | 3.5 | **6.5** | Lat: -7.5/2.5 Lon:-57/-44 | |
| 06:00 28 Apr | -3/-51.5 | **5** | 5.5 | Lat: -8/2   Lon:-**58**/-45 | |
| 12:00 28 Apr | -5/-51 | 4 | 6 | Lat: -**10**/0  Lon:-57.5/-44.5 | |

Table 4.6 – Limits and areas considered for quasi-Lagrangian and Eulerian energy calculations in ASL of 06-07 May 2015

| Satellite Imagery | | | | | |
|---|---|---|---|---|---|
| Time UTC - 2015 | Center lat/lon | Meridional distance from the center (degrees) | Zonal distance from the center (degrees) | Area for quasi-Lagrangian calculation (4°lat and 4.5°lon away the center) | Area for Eulerian calculation |
| 18:00 06 May | 1.5/-51 | 3.5 | 2 | Lat: -2.5/**5.5**   Lon:-55.5/-**46.5** | Lat: -4/5.5 Lon: -66.5/-46.5 |
| 00:00 07 May | 1.5/-54 | 3.5 | 3 | Lat: -2.5/5.5   Lon:-58.5/-49.5 | |
| 06:00 07 May | 1.5/-57 | 3.5 | 3 | Lat: -2.5/5.5   Lon:-61.5/-52.5 | |
| 12:00 07 May | 0/-59.5 | **4** | **4.5** | Lat: -4/4   Lon:-64/-55 | |
| 18:00 07 May | 0/-62 | 4 | 4 | Lat: **-4**/4   Lon:**-66.5**/-57.5 | |
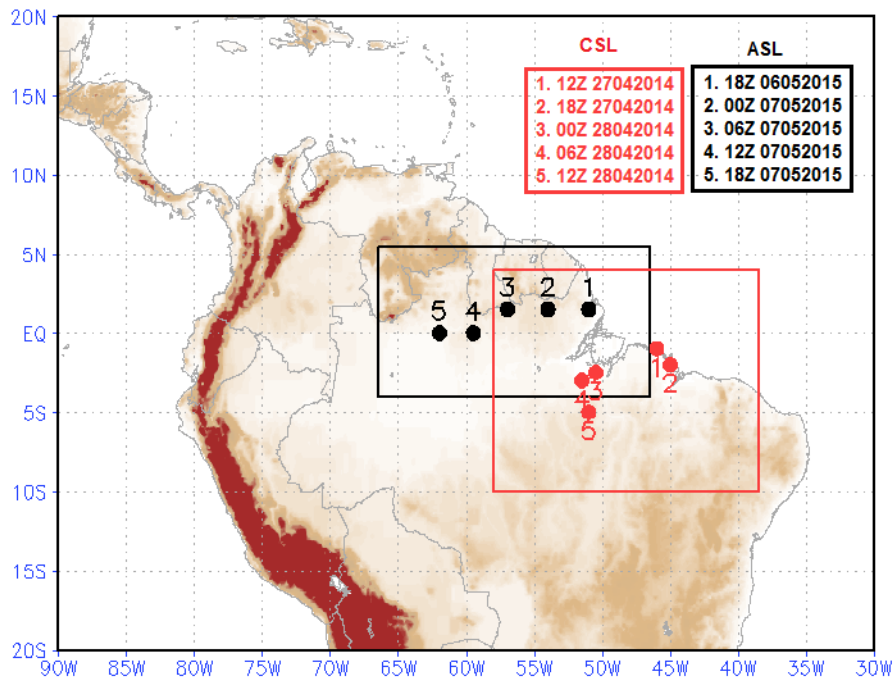


Figure 4.18 - The areas defined by continues lines represent the area considered in each SL event (red: CSL, black: ASL) for Eulerian scheme. The points represent the center of systems at each 6 hours used to define the areas in quasi-Lagrangian approach.

54

## 4.3. LORENZ ENERGY

This section present the time series, considering 24 hours before and after the SLs occurrence, of the Lorenz Cycle Energy terms integrated in all the volume considered for the quasi-Lagrangian and Eulerian approaches. The cycles of energy considering only Eulerian approach since includes local derivatives, also are presented.

### 4.3.1. ENERGIES

For CSL of 27-28 April 2014, $K_Z$ was the term with greatest values compared to other terms ($K_Z$ was one order of magnitude greater) in both approaches (Figs. 4.19a and 4.19b). This is according to da Silva and Satyamurty (2013) who found higher values of kinetic energy than available potential energy studying the energetic of the ITCZ. The time series show an increase of $K_Z$ at the end of the CSL event and the values increased from 10 to 26 x $10^4$ J m$^{-2}$. The next term with high values was $K_E$, which like $K_Z$, it increased at the end of event with maximum value of almost 51 x $10^3$ J m$^{-2}$ at 12:00 UTC 28 April 2014. The other terms ($A_Z$ and $A_E$) were smaller and presented only variation with diurnal cycle presenting maximums at 18:00 UTC since them depend of the air temperature. $A_Z$ and $A_E$ terms were one order of magnitude smaller than the zonal kinetic term because the horizontal thermal gradients are very small in the equatorial region. The above characteristics were observed in both schemes. However, the Eulerian approach emphasized the $K_E$ and $A_E$ values more than the quasi-Lagrangian approximation. The opposite occurred with the values of $K_Z$, which were higher in the quasi-Lagrangian than in the Eulerian approximation.
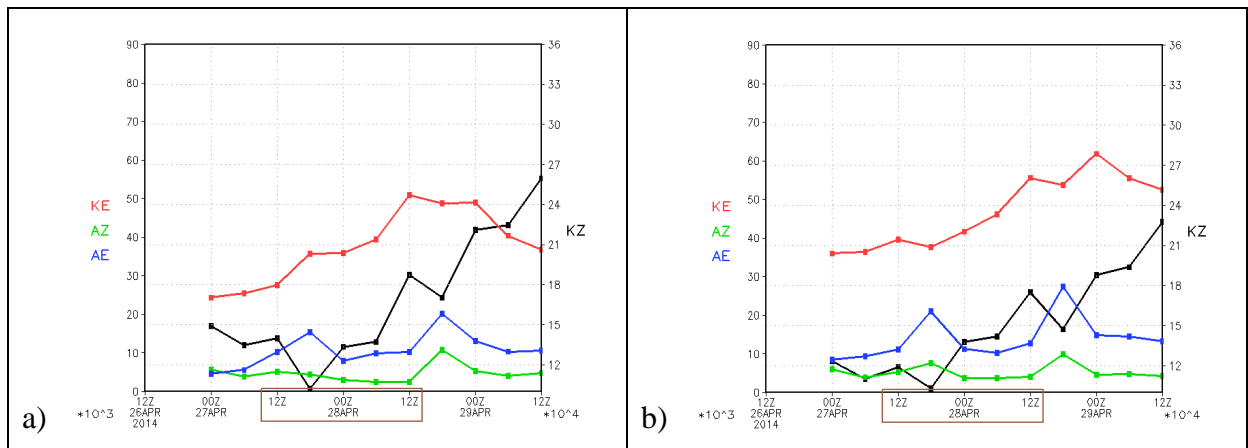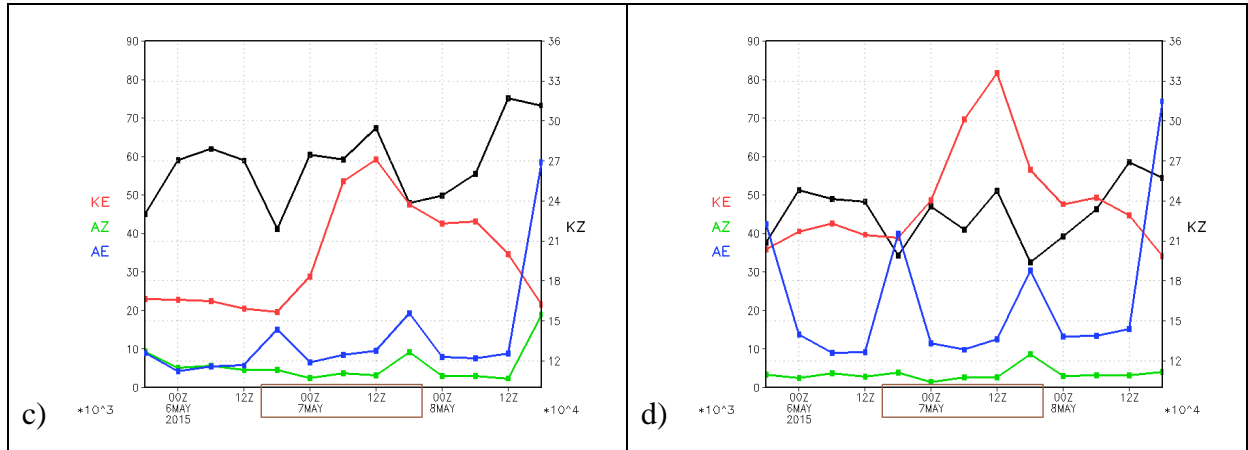
Figure 4.19 - Time series of volume-integrated of Lorenz energy terms ($K_Z$ x$10^4$, $K_E$ x$10^3$, $A_Z$ x$10^3$ and $A_E$ x$10^3$) for CSL → 27-28 Abril 2014 (top) and ASL → 06-07 May 2015 (bottom) calculated using: (a)-(c) Quasi-Lagrangian and (b)-(d) Eulerian approaches. Values in J m$^{-2}$.

For ASL event (Figs. 4.19c and 4.19d), from 06-07 May 2015 in both schemes $K_Z$ was also the term with highest values (it was one order magnitude greater compared with the other terms). The time evolution of $K_Z$ presents an evident diurnal cycle behavior with minimums and maximums, respectively, at 18:00 and 12:00 UTC, and values range from 21 to 32 x $10^4$ J m$^{-2}$. As in CSL, $K_E$ was also the second term of importance and it increased during the ASL occurrence reaching a peak at 12:00 UTC 07 May 2015. Comparatively, $K_E$ was higher in Eulerian (maximum of 80x$10^3$ J m$^{-2}$) than in quasi-Lagrangian scheme (maximum of 60x$10^3$ J m$^{-2}$). For ASL case, $A_Z$ and $A_E$ only varied according to the diurnal cycle and their values were higher in Eulerian than in quasi-Lagrangian scheme.

Comparing the two SL events, for each energetic term the ASL presents higher values than the CSL. This probably happens because the ASL needs more energy to move to the Amazon basin.

Time series of vertical profiles of the Lorenz energy terms are presented in Figure 4.20. Using Eulerian approach, CSL event showed maximum values of $K_Z$ in the layers of 650-1000 hPa and 100-200 hPa after 00:00 UTC 28 April (Fig. 4.20b). In the quasi-Lagrangian scheme $K_Z$ values were higher than in Eulerian scheme mostly at mid-upper atmospheric levels (Figs. 4.20a-b).

From Figures 4.20c-d, maximum values of KZ in 600-1000 hPa and 100-150 hPa layers in both Eulerian and quasi-Lagrangian approaches characterized the ASL life cycle. In addition, in the quasi-Lagrangian approximation it was also observed a maximum of $K_Z$ in

mid-levels (150-400 hPa layer) from 00:00 UTC 07 May until the end the event, which did not occur in Eulerian approach. It is important to note that $K_Z$ at low-levels was more intense during the initial phase (from 18:00 UTC 06 May to 06:00 UTC 07 May) of ASL event, which was mainly associated with the low-level jet shown in Figure 4.15b.
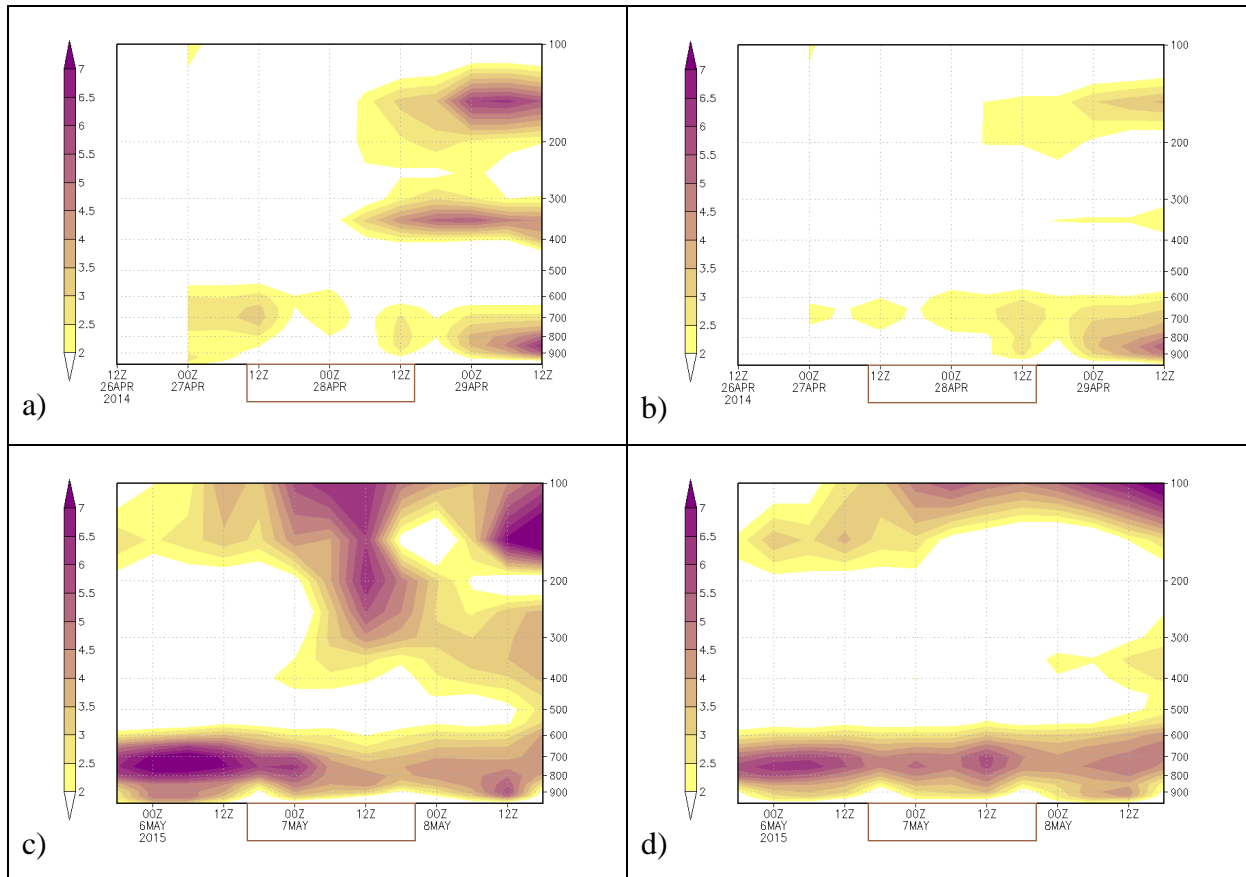


Figure 4.20 - Time series of vertical profiles of $K_Z$ for CSL → 27-28 Abril 2014 (top) and ASL → 06-07 May 2015 (bottom) calculated using: (a)-(c) Quasi-Lagrangian and (b)-(d) Eulerian approaches. Values in J m$^{-2}$. The brown box represents the development time of the event.

The vertical profiles of $K_E$ in CSL in Figures 4.21a-b showed maximum values between 100 and 550 hPa, which were greater at the end of its life cycle at mid-levels; but unlike of $K_Z$ the maximum values of $K_E$ were obtained in Eulerian approach. For ASL (Figs. 4.21c-d), the $K_E$ time tendencies were similar in both schemes, with high values in the layer 100-400 hPa during SL mature phase (between 00:00 UTC to 18:00 UTC 07 May). Like in CSL, Eulerian approach presented higher values of $K_E$ than quasi-Lagrangian approach.
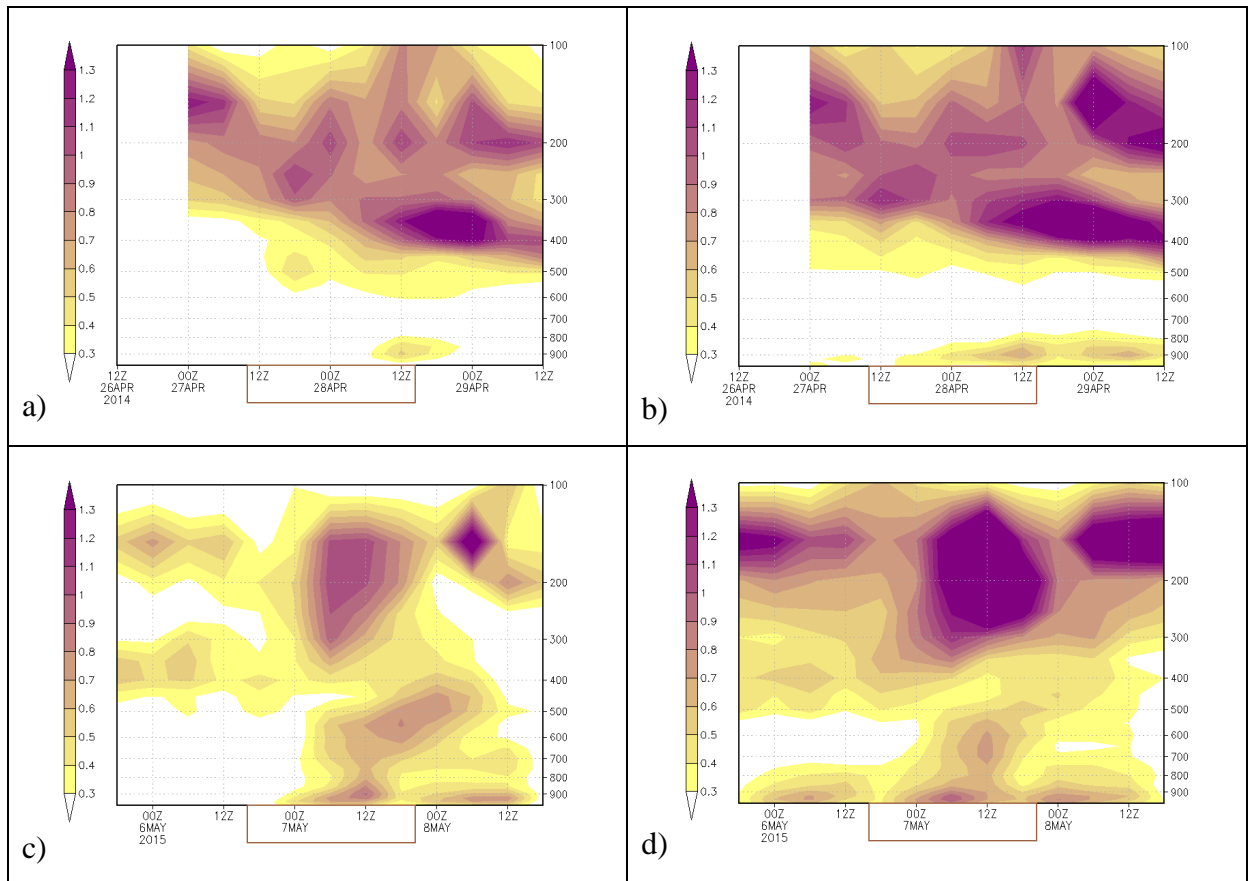
Figure 4.21 - Time series of vertical profiles of $K_E$ for CSL → 27-28 Abril 2014 (top) and ASL → 06-07 May 2015 (bottom) calculated using: (a)-(c) Quasi-Lagrangian and (b)-(d) Eulerian approaches. Values in J m$^{-2}$. The brown box represents the development time of the event.

In both CSL and ASL, $A_Z$ and $A_E$ only showed diurnal variation, with maximum occurring at 18:00 UTC of each day (Figs. 4.22 and 4.23). Comparatively, $A_Z$ was higher in quasi-Lagrangian scheme than in Eulerian scheme, while the opposite occurred for $A_E$.
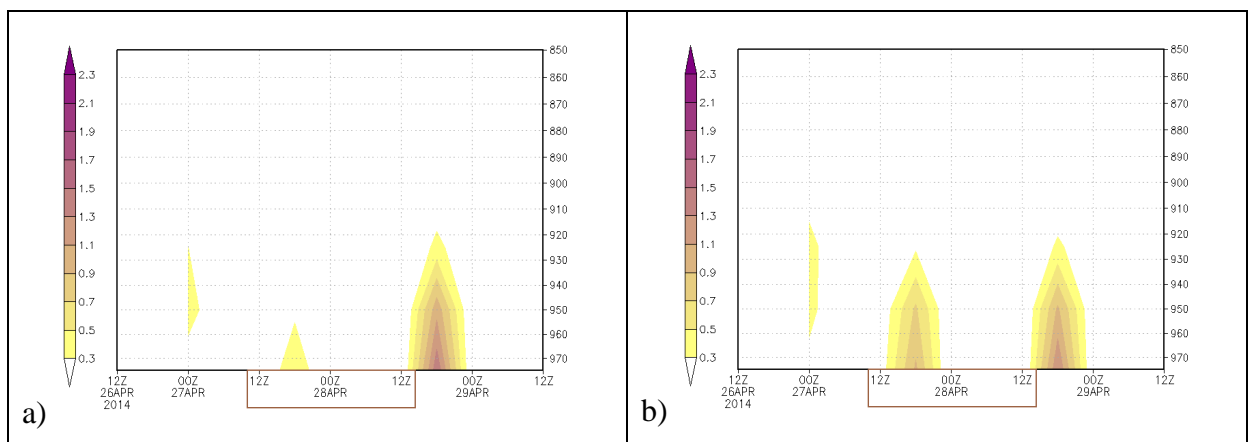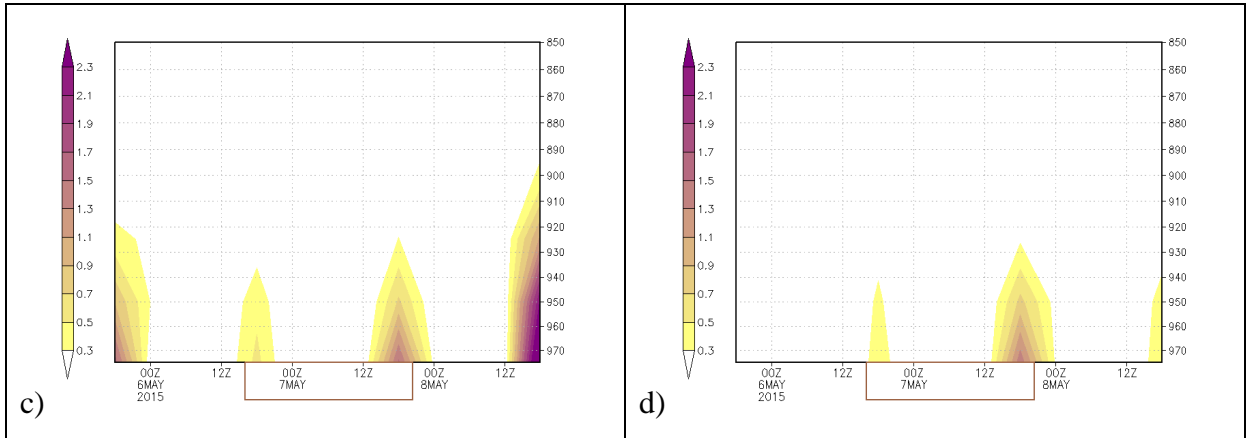
Figure 4.22 - Time series of vertical profiles of $A_Z$ for CSL → 27-28 Abril 2014 (top) and ASL → 06-07 May 2015 (bottom) calculated using: (a)-(c) Quasi-Lagrangian and (b)-(d) Eulerian approaches. Values in J m$^{-2}$. The brown box represents the development time of the event.
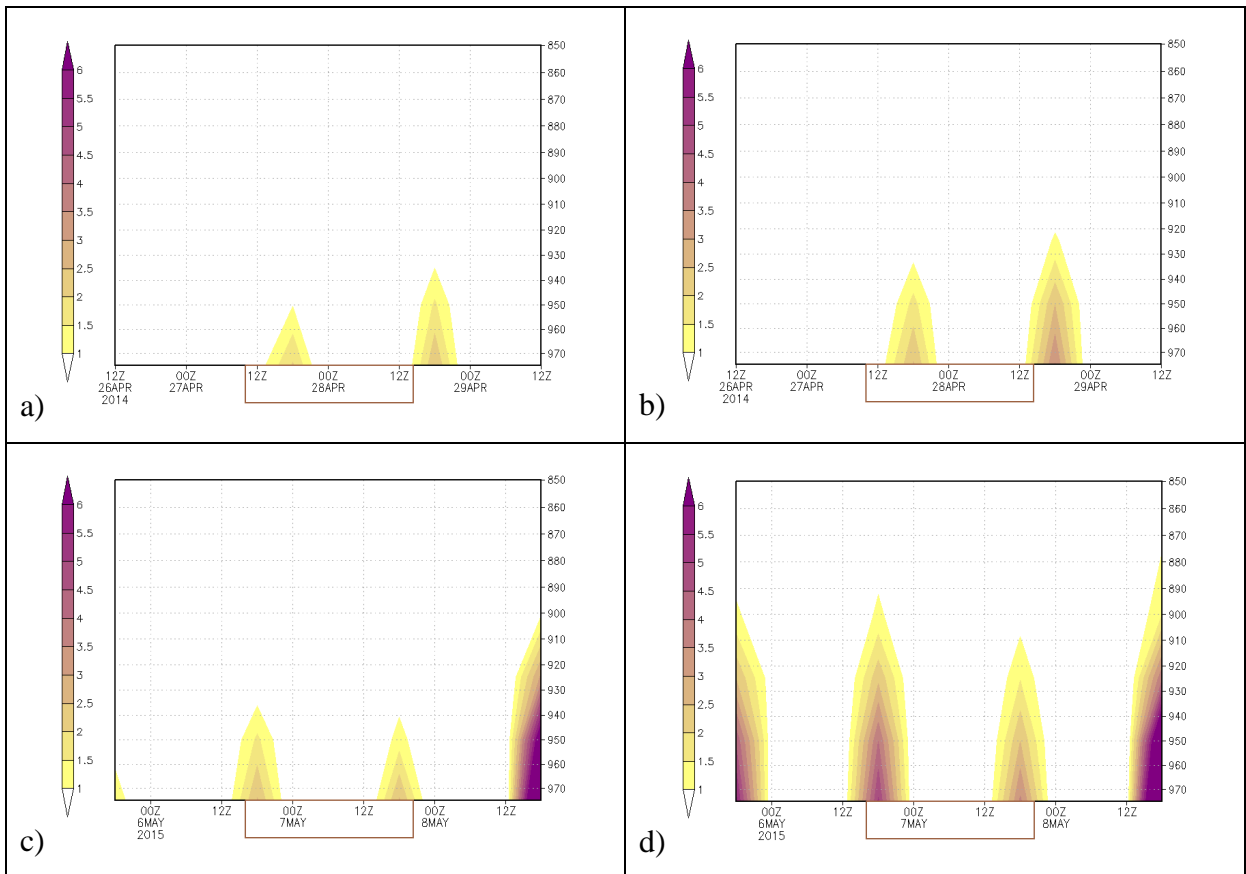


Figure 4.23 - Time series of vertical profiles of $A_E$ for CSL → 27-28 Abril 2014 (top) and ASL → 06-07 May 2015 (bottom) calculated using: (a)-(c) Quasi-Lagrangian and (b)-(d) Eulerian approaches. Values in J m$^{-2}$. The brown box represents the development time of the event.

### 4.3.2. ENERGY CONVERSIONS

In Figure 4.24, the time evolution of volume-integrated energy conversion terms shows a slight increase of $C_E$ ($A_E$, $K_E$) during the CSL event and the increase is more evident in the Eulerian scheme. In most of the time, $C_K$ ($K_E$, $K_Z$) stayed constant and close to zero in both approaches. A little increase after 00:00 UTC 28 April of $C_Z$ ($K_Z$, $A_Z$) was noted, mainly in quasi-Lagrangian scheme. The $C_A$ ($A_Z$, $A_E$) term had lower values than the other terms (one order of magnitude smaller) and stayed quasi-constant during all CSL life cycle, which was due to the very small thermal gradients in equatorial latitudes. Da Silva and Satyamurty (2013) and Hsieh and Cook (2007) obtained similar behavior for $C_A$ ($A_Z$, $A_E$) term in the equatorial latitudes.
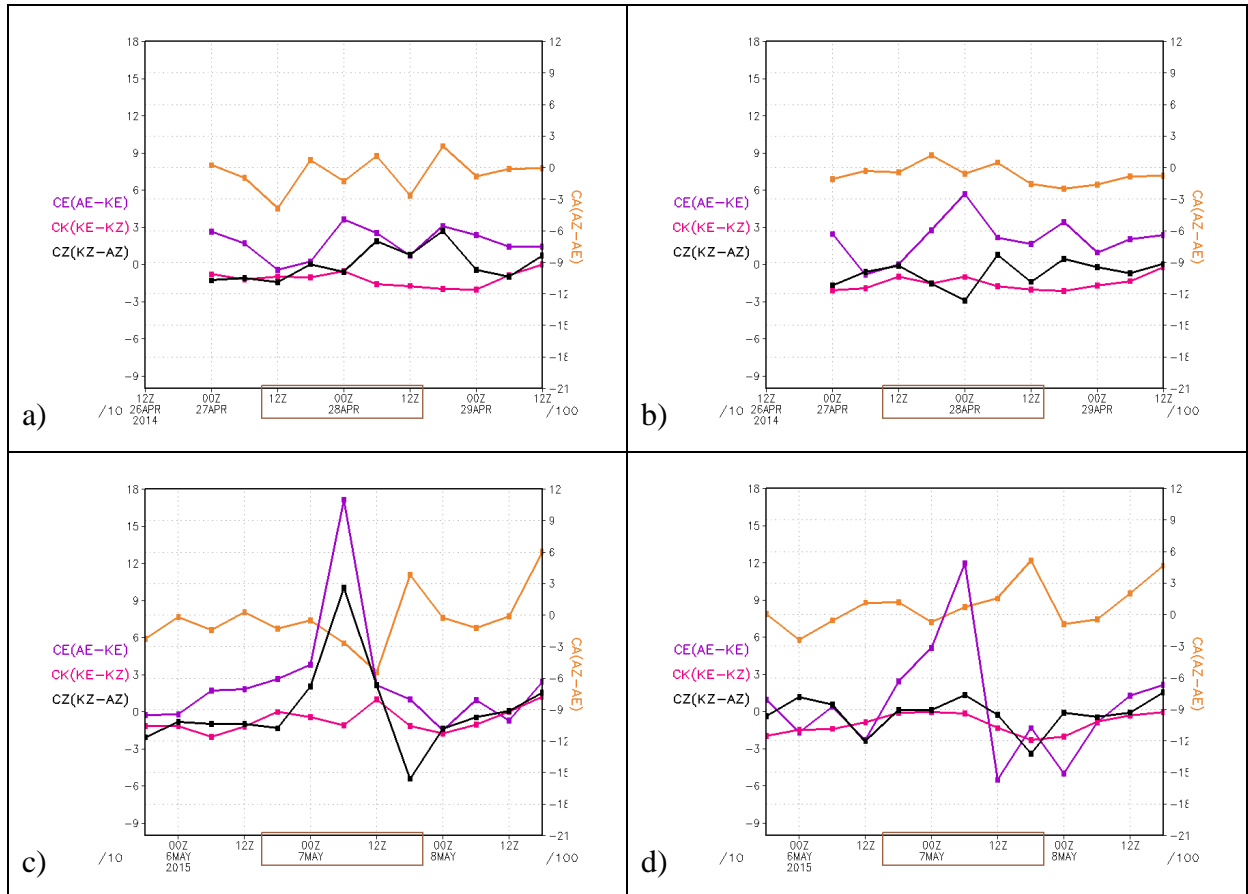


Figure 4.24 - Time series of volume-integrated energy conversions of Lorenz energy cycle ($C_A$ x$10^{-2}$, $C_E$ x$10^{-1}$, $C_K$ x$10^{-1}$ and $C_Z$ x$10^{-1}$) for CSL → 27-28 Abril 2014 (top) and ASL → 06-07 May 2015 (bottom) calculated using: (a)-(c) Quasi-Lagrangian and (b)-(d) Eulerian approaches. Values in W m$^{-2}$.

For ASL, the $C_E$ ($A_E$, $K_E$) term increased during the event and attained a maximum value of 1.7 W m$^{-2}$ at 06:00 UTC 07 May. The increase of $C_E$ was higher in quasi-Lagrangian

than in Eulerian scheme (Fig. 4.24c and 4.24d). It was also noted an increase of $C_Z$ ($K_Z$, $A_Z$) during the developing of ASL event with maximum value of 1.0 W m$^{-2}$ at 06:00 UTC 07 May. The increase of $C_Z$ was larger in quasi-Lagrangian than in Eulerian framework. As in CSL, in ASL event $C_K$ ($K_E$, $K_Z$) stayed constant and close to zero, and $C_A$ ($A_Z$, $A_E$) term had one order of magnitude smaller than the other terms and stayed quasi-constant in both approaches.

For the ASL and CSL events, the energy and conversion terms were one order of magnitude smaller compared with extratropical systems as the cyclones analyzed by Dias Pinto and da Rocha (2011), but they had the same order of magnitude of tropical and equatorial systems as ITCZ system analyzed by da Silva and Satyamurty (2013).

The energy of two cyclones presented by Dias Pinto and Da Rocha (2011), as well as in other works analyzing extratropical latitudes, the terms of $C_A$ ($A_Z$, $A_E$) and $C_E$ ($A_E$, $K_E$) dominated, showing the importance of baroclinic instability in mid-latitudes. For the CSL and ASL events analyzed in this work, the terms $C_E$ ($A_E$, $K_E$) and $C_Z$ ($K_Z$, $A_Z$) also were strong, mainly for ASL occurrence, showing the importance of baroclinic instability in these type of systems. However, as well as in da Silva and Satyamurty (2013), the term $C_K$ ($K_E$, $K_Z$) presented the same order of $C_E$ ($A_E$, $K_E$), showing also the importance of barotropic instability in tropical systems.

The baroclinic term $C_A$ ($A_Z$, $A_E$) presented small values in both quasi-Lagrangian and Eulerian approaches for ASL and CSL events (Fig. 4.25). For CSL, there were negative values of $C_A$ ($A_Z$, $A_E$) above 350 hPa, i.e., it was occurring conversion from $A_E$ to $A_Z$ in this layer and it was higher at start and the end of the event (12:00 UTC 27 and 28 April). The negative values of $C_A$ also presented in time series of volume-integrated (Fig. 4.24a). For ASL, the vertical profile of $C_A$ ($A_Z$, $A_E$) showed negative values (conversion energy is from $A_E$ to $A_Z$) above 300 hPa and a small region of positive values (conversion energy is from $A_Z$ to $A_E$) in 300-550 hPa layer.
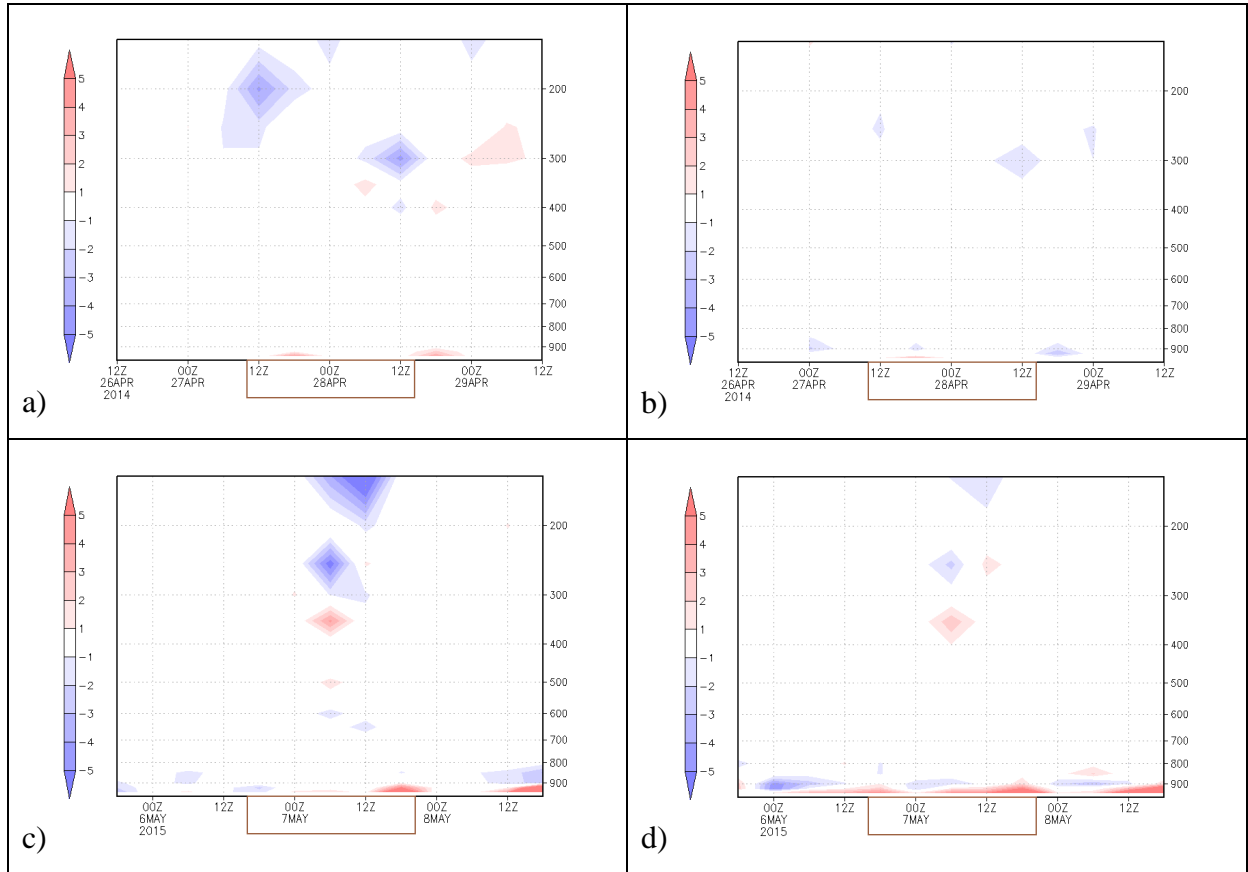
Figure 4.25 - Time series of vertical profiles of $C_A$ ($A_Z$, $A_E$) x$10^{-6}$ for CSL → 27-28 Abril 2014 (top) and ASL → 06-07 May 2015 (bottom) calculated using: (a)-(c) Quasi-Lagrangian and (b)-(d) Eulerian approaches. Values in W m$^{-2}$. The brown box represents the development time of the event.

In both quasi-Lagrangian and Eulerian schemes, the baroclinic term $C_E$ ($A_E$, $K_E$) for CSL was positive in 200-400 hPa layer, which means conversion from $A_E$ to $K_E$ or that $K_E$ developed at the expense of $A_E$ and it occurred in all life cycle of CSL (Fig. 4.26a-b). The $C_E$ ($A_E$, $K_E$) term also was positive in 200-550 hPa layer and negative over 200 hPa for ASL event between 12:00 UTC 06 and 18:00 UTC 07 May. Comparatively, the quasi-Lagrangian approach provided larger values of $C_E$ ($A_E$, $K_E$) than Eulerian scheme (Fig. 4.26c-d).
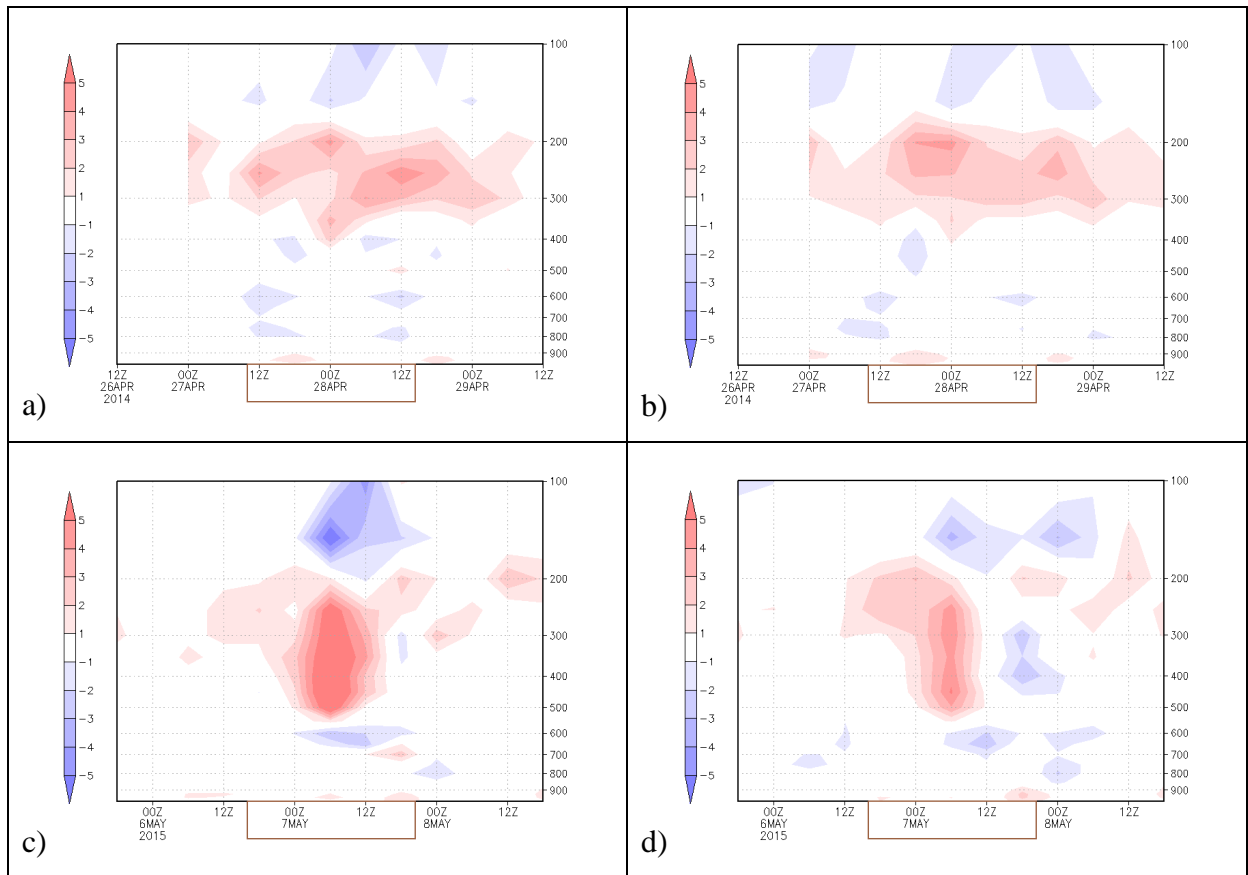
Figure 4.26 - Time series of vertical profiles of $C_E$ ($A_E$, $K_E$) x10$^{-5}$ for CSL → 27-28 Abril 2014 (top) and ASL → 06-07 May 2015 (bottom) calculated using: (a)-(c) Quasi-Lagrangian and (b)-(d) Eulerian approaches. Values in W m$^{-2}$. The brown box represents the development time of the event.

In the Figures 4.27a-b, for CSL the barotropic term $C_K$ ($K_E$, $K_Z$) presented negative values in 300-500 hPa layer and principally at the end of the event in quasi-Lagrangian approach. This implied in conversion from $K_Z$ to $K_E$ or that $K_E$ developed at the expenses of $K_Z$ in this layer. In the ASL event, the $C_K$ ($K_E$, $K_Z$) term was mainly negative below 500 hPa and positive ($K_Z$, $K_E$) above of 400 hPa, which was more evident in quasi-Lagrangian than in Eulerian scheme (Fig. 4.27c-d). This conversion occurred mostly during the time of maximum development of ASL (from 06:00 to 12:00 UTC 07 May).

Figure 4.27 - Time series of vertical profiles of $C_K$ ($K_E$, $K_Z$) x10$^{-5}$ for CSL → 27-28 Abril 2014 (top) and ASL → 06-07 May 2015 (bottom) calculated using: (a)-(c) Quasi-Lagrangian and (b)-(d) Eulerian approaches. Values in W m$^{-2}$. The brown box represents the development time of the event.

As presented in Figures 4.28a-b, for CSL event the baroclinic term $C_Z$ ($K_Z$, $A_Z$) did not show a clear pattern and it was close to zero in both of schemes, indicating that the baroclinic conversion of energy was not important for coastal SLs. However, in the ASL (Fig. 4.28c-d), this term was positive in 200-600 hPa layer and negative above 200 hPa, mainly in quasi-Lagrangian approach. The positive values of $C_Z$ term indicated energy conversion from $K_Z$ to $A_Z$ between 00:00 and 18:00 UTC 07 May.

Figure 4.28 - Time series of vertical profiles of $C_Z$ ($K_Z$, $A_Z$) $x10^{-5}$ for CSL → 27-28 Abril 2014 (top) and ASL → 06-07 May 2015 (bottom) calculated using: (a)-(c) Quasi-Lagrangian and (b)-(d) Eulerian approaches. Values in W m$^{-2}$. The brown box represents the development time of the event.

### 4.3.3. BOUNDARY ENERGY TRANSPORTS

Since the areas and borders are changing at each time in the quasi-Lagrangian approach it is noted large differences of the boundary transport terms compared to Eulerian scheme that have the same area in all times. According the Figure 4.29, in both CSL and ASL events, the boundary energy transports $BK_Z$ and $BK_E$ had a higher order than other terms.

The exchange energy between the domain and neighborhoods in CSL did not show a marked tendency during its life cycle (Figs. 4.29a and 4.29b). By contrast, both $BK_Z$ and $BK_E$ increased during ASL occurrence in the quasi-Lagrangian scheme, reaching a maximum at 12:00 UTC 7 May. It important to note that as $K_Z$ term the $BK_Z$ also presented a diurnal variation with maximum values at 12:00 UTC. At the beginning of the ASL event $BA_Z$ increased and $BA_E$ decreased (Fig. 4.29c). This last term was negative in most part of the life cycle of ASL in the quasi-Lagrangian approach. The time series of boundary energy

transports for ASL in Eulerian scheme (Fig. 4.29d) were almost constant with time and they were very different of that obtained in quasi-Lagrangian approach (Fig. 4.29c). From Eulerian approach, only $BA_E$ presented a diurnal cycle with maximum at 18:00 UTC.
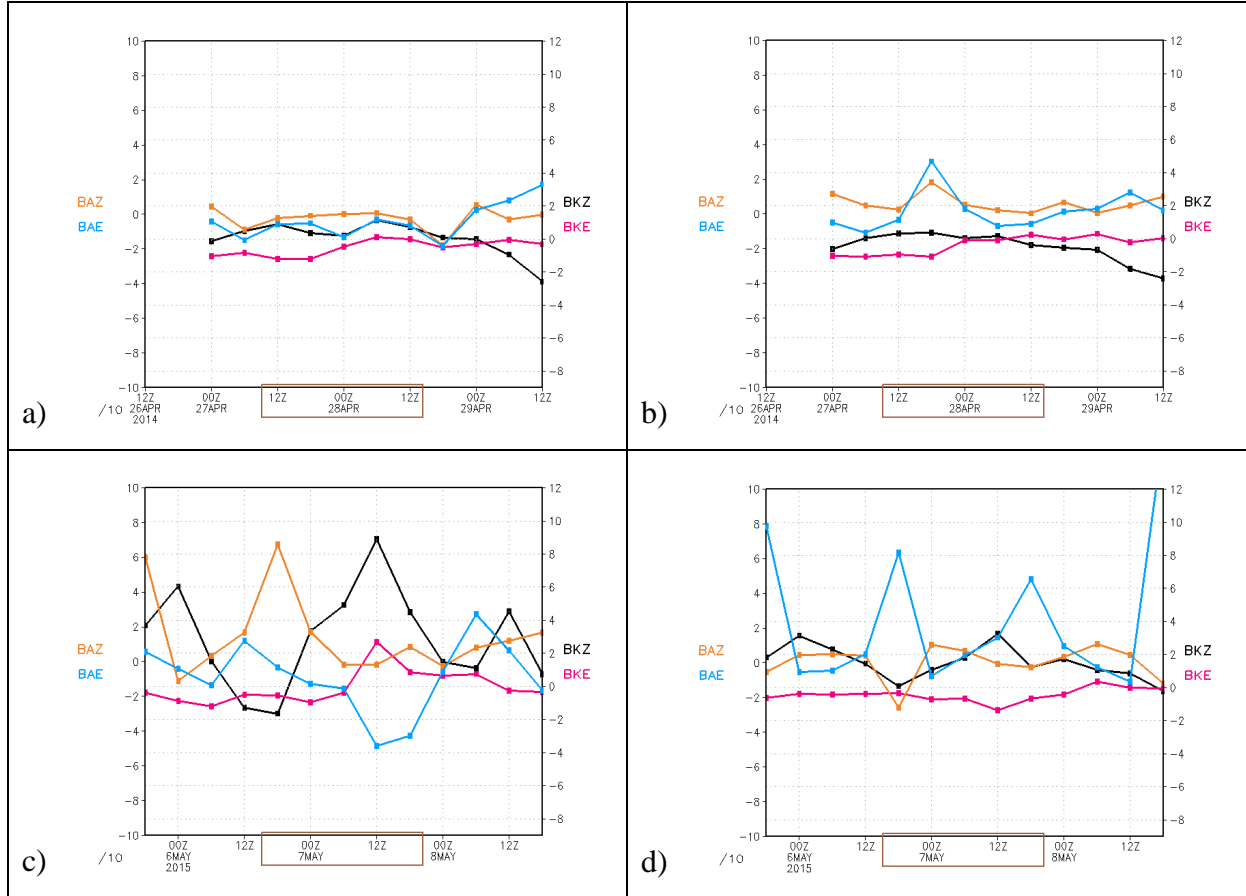


Figure 4.29 - Time series of volume-integrated boundary energy transports of Lorenz energy cycle ($BK_Z$, $BK_E$, $BA_Z$ x10$^{-1}$ and $BA_E$ x10$^{-1}$) for CSL → 27-28 Abril 2014 (top) and ASL → 06-07 May 2015 (bottom) calculated using: (a)-(c) Quasi-Lagrangian and (b)-(d) Eulerian approaches. Values in W m$^{-2}$.

During CSL life cycle, the transport of energy $K_Z$ across the boundary did not present a clear pattern in any of the approaches (Figs. 4.30a-b). On other hand, in ASL event, $BK_Z$ presented positive and negative values, respectively, above 400 hPa and below 500 hPa after 00:00 UTC 07 May, mainly in quasi-Lagrangian scheme (Figs. 4.30a and 4.30c). The positive values of $BK_Z$ mean that the transport of energy is from outside to into the area of study, while the negative values are related with energy transport from the study area to its surroundings. The increment of $BK_Z$ during the ASL developing (from 18:00 UTC 06 May to 18:00 UTC to 07 May) in the volume-integrated representation (Fig. 4.29c) was well represented by positive values in 100-300 hPa layer in vertical profile (Fig. 4.30c).
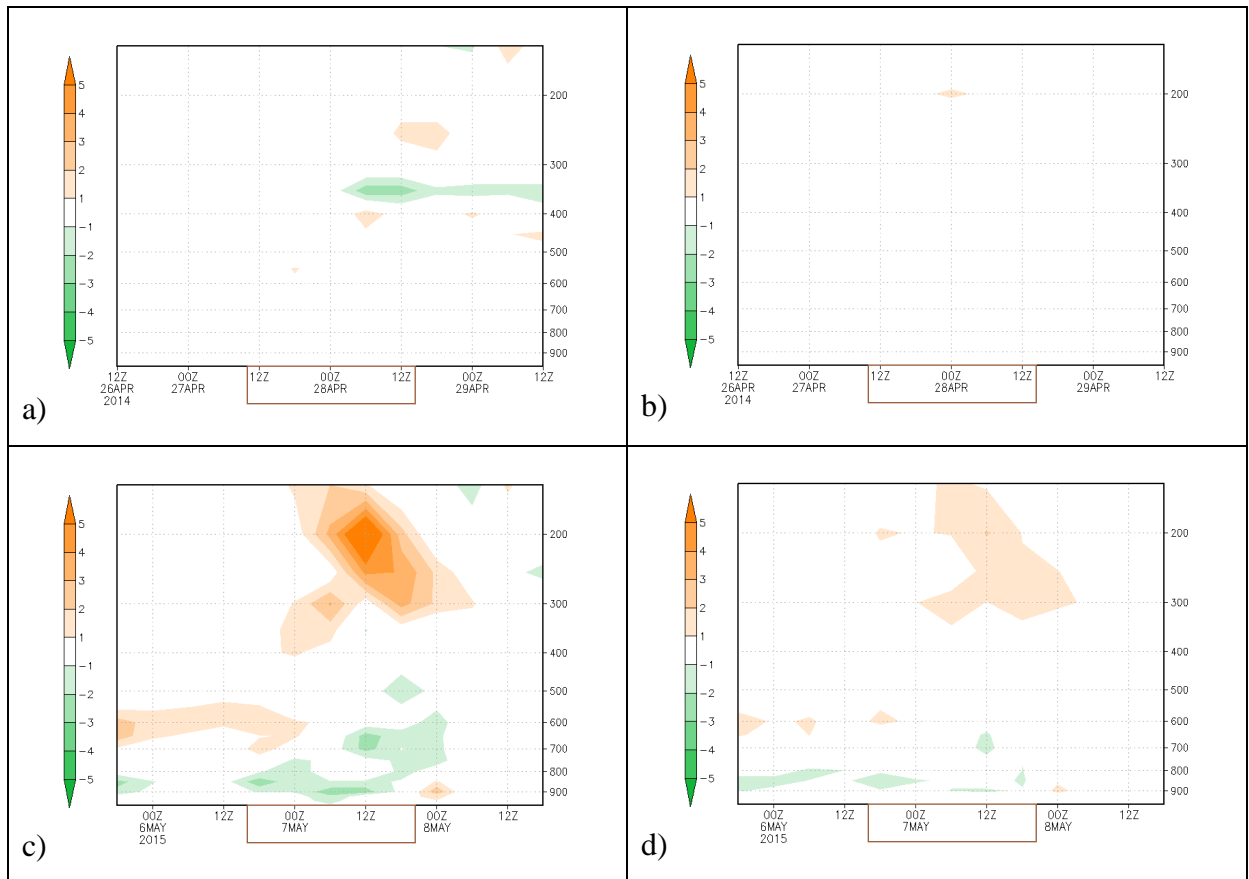
Figure 4.30 - Time series of vertical profiles of $BK_Z$ x10$^{-1}$ for CSL → 27-28 Abril 2014 (top) and ASL → 06-07 May 2015 (bottom) calculated using: (a)-(c) Quasi-Lagrangian and (b)-(d) Eulerian approaches. Values in W m$^{-2}$. The brown box represents the development time of the event.

Like $BK_Z$, if $BK_E$ is positive, there is energy transport from the surroundings into the study area, and if it is negative, the opposite is occurring. According Figures 4.31a and 4.31b in both of schemes for CSL event, $BK_E$ was positive above 350 hPa and negative in the layer 350-500 hPa. For ASL, Figures 4.31c and 4.31d depicted both approaches showing $BK_E$ mostly positive above 300 hPa and negative below this level. The values of $BK_E$ for ASL were more intense than for CSL.
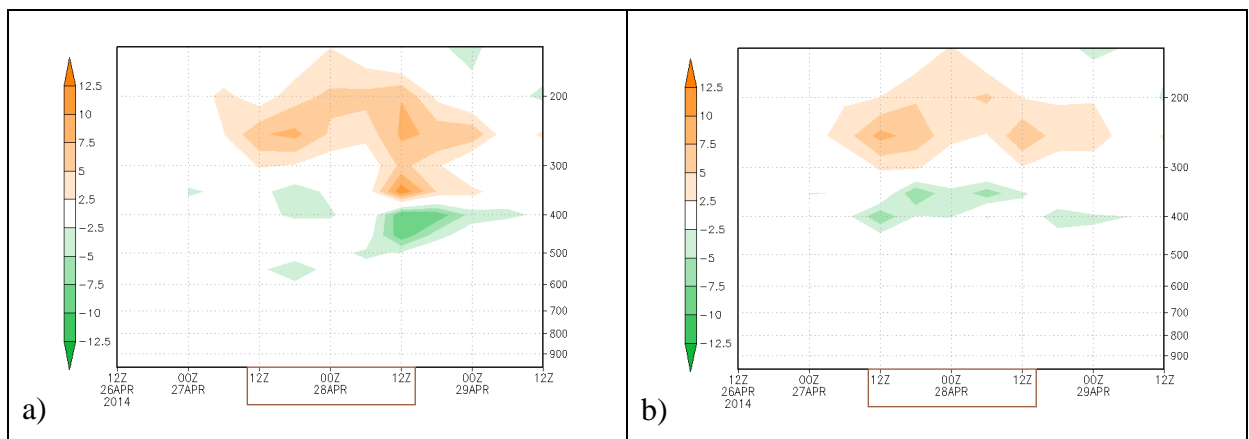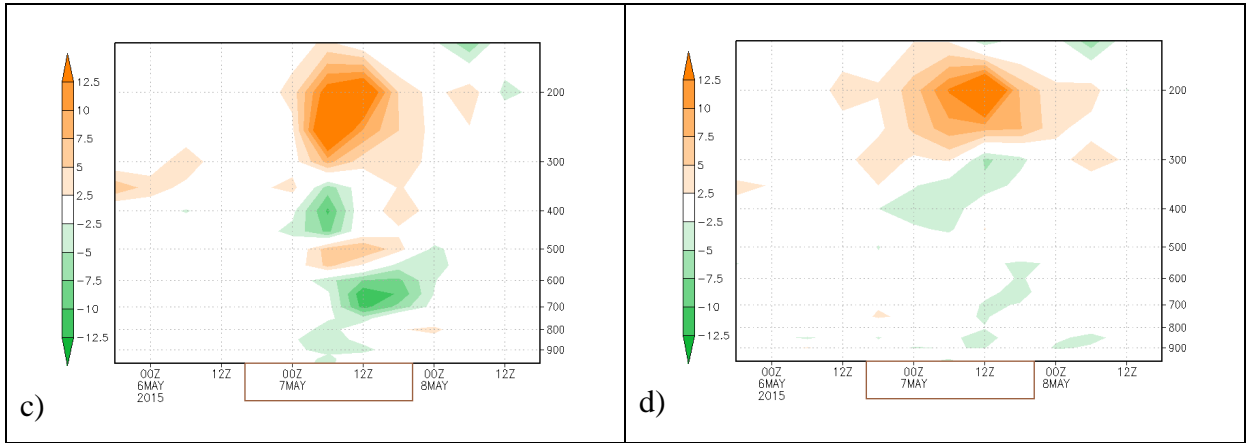
Figure 4.31 - Time series of vertical profiles of $BK_E$ $x10^{-2}$ for CSL → 27-28 Abril 2014 (top) and ASL → 06-07 May 2015 (bottom) calculated using: (a)-(c) Quasi-Lagrangian and (b)-(d) Eulerian approaches. Values in W m$^{-2}$. The brown box represents the development time of the event.

As shown in Figures 4.32 and 4.33, both $BA_Z$ and $BA_E$ terms did not show a clear pattern in CSL event. On the other hand, these terms were more intense during the ASL maximum development (06:00 UTC 07 May), implying higher flux of available energy by the boundaries in ASL than in CSL.
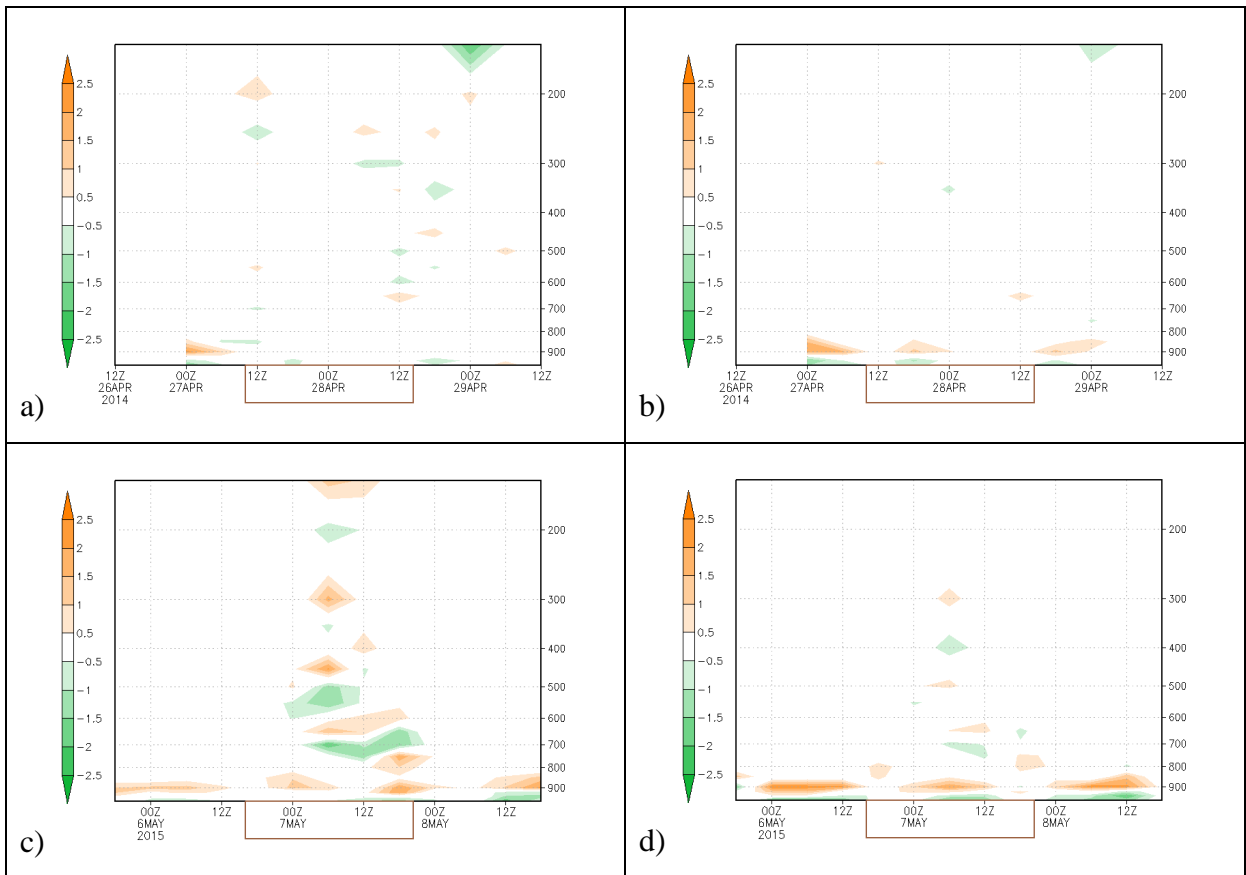


Figure 4.32 - Time series of vertical profiles of $BA_Z$ $x10^{-3}$ for CSL → 27-28 Abril 2014 (top) and ASL → 06-07 May 2015 (bottom) calculated using: (a)-(c) Quasi-Lagrangian and (b)-(d) Eulerian approaches. Values in W m$^{-2}$. The brown box represents the development time of the event.
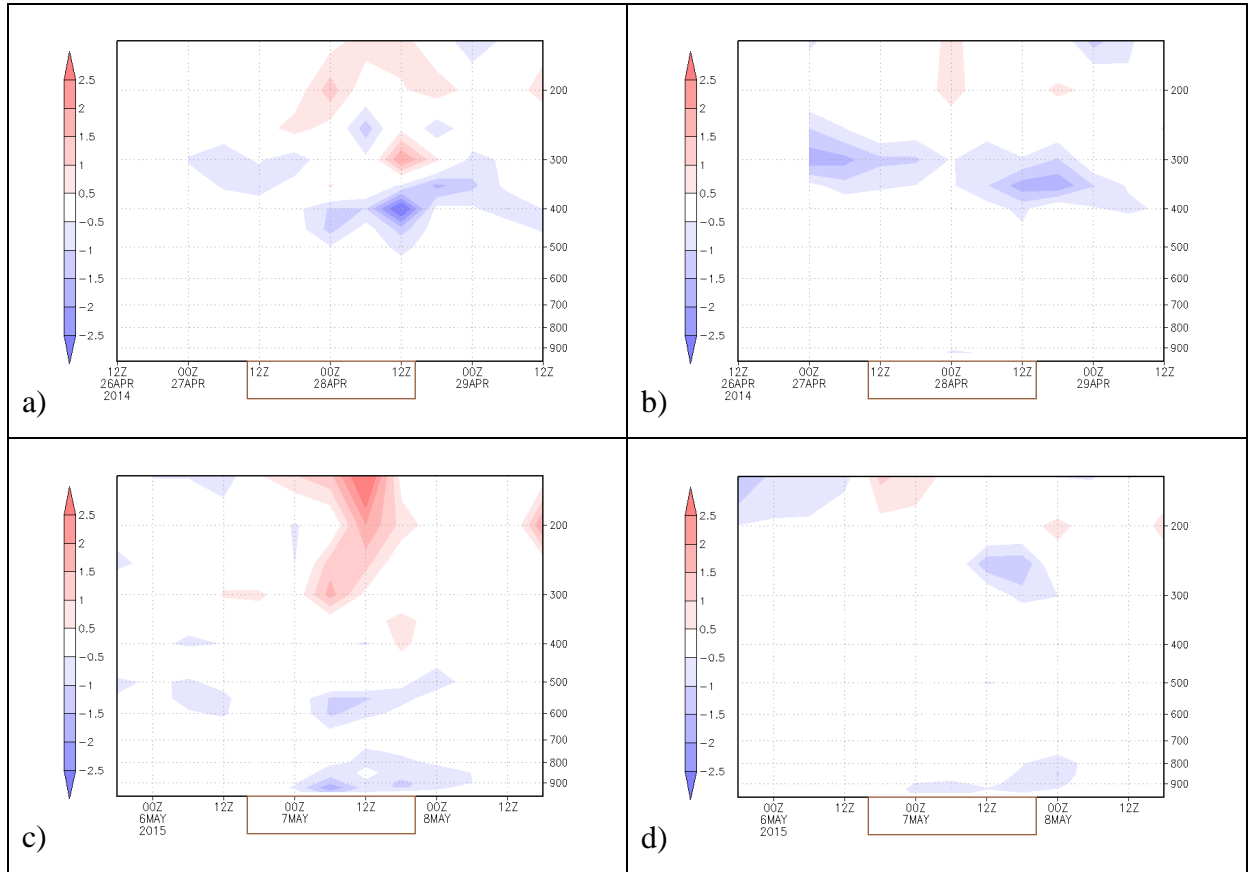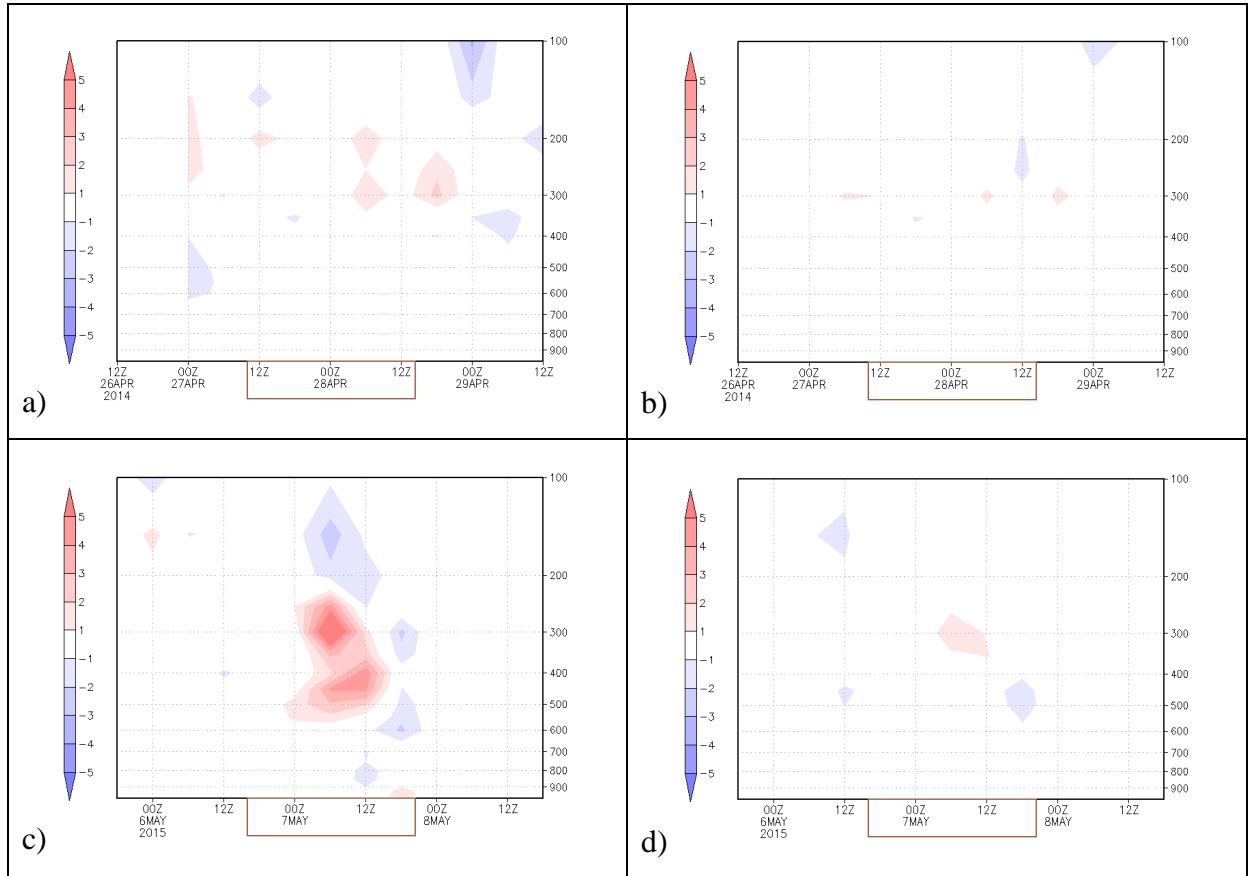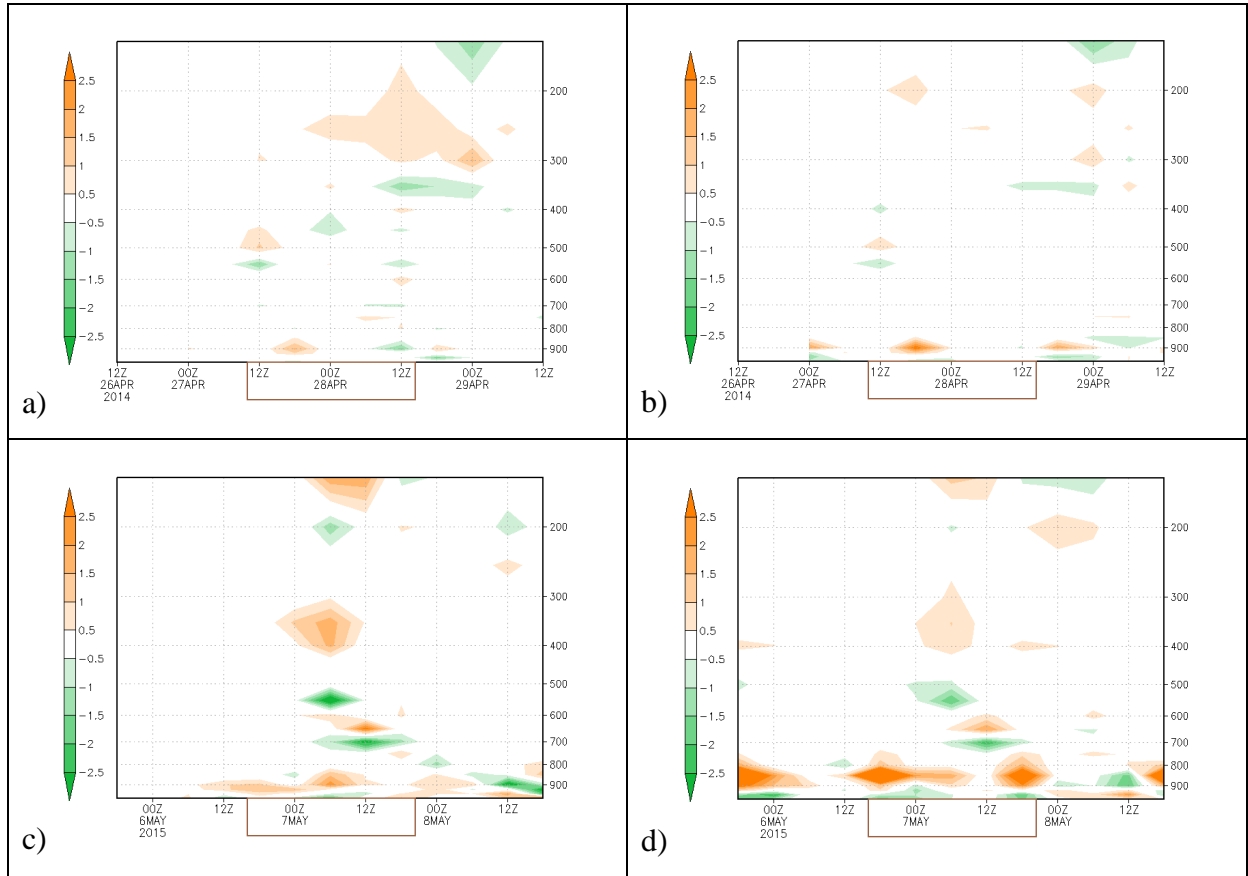
Figure 4.33 - Time series of vertical profiles of $BA_E$ x$10^{-3}$ for CSL $\rightarrow$ 27-28 Abril 2014 (top) and ASL $\rightarrow$ 06-07 May 2015 (bottom) calculated using: (a)-(c) Quasi-Lagrangian and (b)-(d) Eulerian approaches. Values in W m$^{-2}$. The brown box represents the development time of the event.

### 4.3.4. LORENZ ENERGY CYCLE

The Lorenz Energy Cycles for CSL and ASL events were obtained for two moments. (1) Initial-phase, or the first 12 hours, which represents the interval from the first hour of the SL until the hour of maximum intensity.(2) Final-phase, or the last 12 hours, which considers the period since the hour of maximum intensity until the hour of end. The values were multiplied by 10 and are in the Figure 4.34, where the thickness of the arrows is proportional to the magnitude of the terms.

As shown in Fig 4.34a, $K_Z$ incremented with time (4.37x$10^{-1}$ W m$^{-2}$) in CSL initial-phase. The increase was due to: (a) the baroclinic process of conversion from zonal potential available ($A_Z$) to zonal kinetic ($K_Z$) energy, (b) the transport $K_Z$ from the surroundings into the study area (2.49x$10^{-1}$ W m$^{-2}$) and (c) $\Delta R_Z$ acted like a font of energy providing 1.52x$10^{-1}$ W m$^{-2}$ to the system. $K_E$ also increased in CSL initial-phase due to: (a) the barotropic process

69

of conversion of $K_Z$ in $K_E$ (the eddies removed kinetic energy from the zonal flow), (b) the baroclinic conversion of $A_E$ in $K_E$ and (c) $\Delta R_Z$ also was providing energy (giving $3.69 \times 10^{-1}$ W $m^{-2}$). This increase of $K_E$ with the time was smaller than the increase of $K_Z$ with time, which was due to system transferred energy to its surroundings ($BK_E = -7.2 \times 10^{-1}$ W $m^{-2}$).

Regarding to available potential energy, the longitudinal and latitudinal thermal variation in this SCL initial-phase produced potential energy ($\Delta G_Z = 0.31 \times 10^{-1}$ W $m^{-2}$ and $\Delta G_E = 1.84 \times 10^{-1}$ W $m^{-2}$) that was transferred to kinetic energy through baroclinic processes (Fig. 4.34a). This implied in the negative variation with time of $A_Z$ and near zero variation with time of $A_E$ despite the transport of energy from surrounding to the study area ($BA_Z = 0.87 \times 10^{-1}$ and $BA_E = 0.99 \times 10^{-1}$ W $m^{-2}$). The baroclinic process of conversion from $A_Z$ to $A_E$ had very low value, so it did not participate of the energy balance.

In the CSL final-phase (Fig. 4.34b), all energies were increasing with time, but $\partial K_Z/\partial t$ and $\partial K_E/\partial t$ had the higher values. The increase of $K_Z$ with time occurred due to the baroclinic conversion from $A_Z$ to $K_Z$ and, principally, as function of $\Delta R_Z$ that was the main font of energy in the CSL final-phase ($\Delta R_Z = -9.53 \times 10^{-1}$ W $m^{-2}$). The barotropic conversion between $K_Z$ and $K_E$, the baroclinic conversion from $A_E$ to $K_E$ and the boundary transport from surrounding into the area of study were responsible for the increment of $K_E$ with time ($\partial K_E/\partial t = 3.23 \times 10^{-1}$ W $m^{-2}$) although the dissipation by friction was removing $K_E$ ($\Delta R_E = 1.76 \times 10^{-1}$ W $m^{-2}$).

The generations of the available potential energies were higher during CSL final phase ($\Delta G_Z = 0.94 \times 10^{-1}$ W $m^{-2}$ and $\Delta G_E = 3.94 \times 10^{-1}$ W $m^{-2}$) than in CSL initial-phase. It is also noted that $A_Z$ and $A_E$ incremented with time at the end despite of the baroclinic conversions were transforming available potential in kinetic energy at a higher rate than in initial-phase.
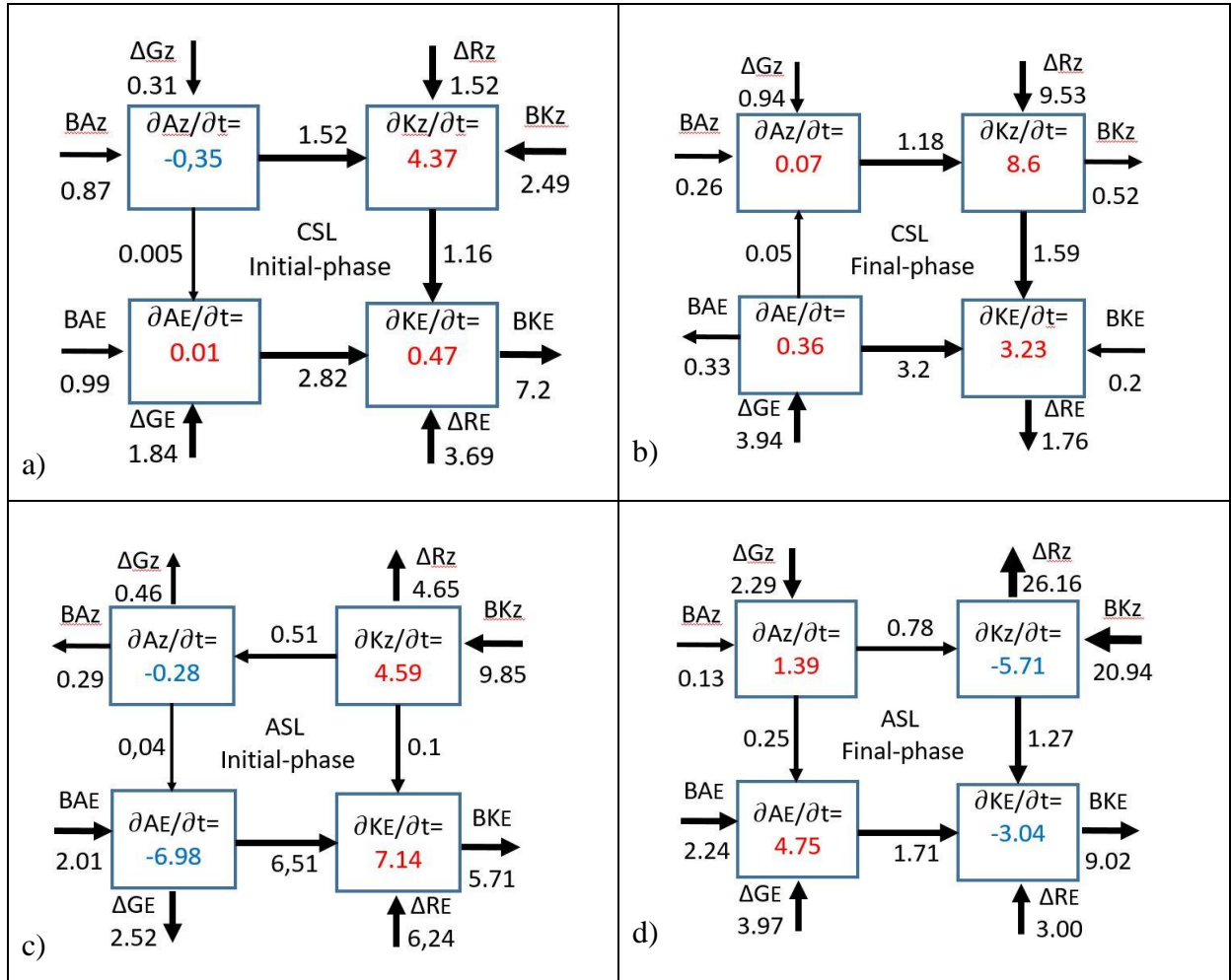
Figure 4.34 - Lorenz Energy Cycles for CSL → 27-28 Abril 2014 (top) and ASL → 06-07 May 2015 (bottom) analyzed in: (**a**)-(**c**) the start and (**b**)-(**d**) the end of the event. Values in W m$^{-2}$x10$^{-1}$.

As shown in Figure 4.34c, the local variation of the kinetic energy was positive, of the available potential energy was negative, in ASL initial-phase, in both zonal and eddy components. The decreased with time of $A_Z$ (-0.28x10$^{-1}$ W m$^{-2}$) is mainly attributed to: a) the energy transport from the area of study to the surroundings (BA$_Z$=-0.29 x10$^{-1}$ W m$^{-2}$), and b) $\Delta G_Z$ removed energy from system (-2.52 x10$^{-1}$ W m$^{-2}$), although the baroclinic conversion between $K_Z$ and $A_Z$ was positive. Similarly, $A_E$ decreased with time as function of the : a) $\Delta G_E$ acted like a sink of energy and b) the high value of baroclinic conversion between $A_E$ and $K_E$ (6.51x10$^{-1}$ W m$^{-2}$). This baroclinic process converted available potential energy into kinetic energy through the upward motions of the warm air and downward motions of the cold air in the same latitude (Asnani, 2005) due to the strong convective activity in the initial-phase of ASL. The positive local variation of $K_Z$ resulted solely of the energy transport of the surrounding to the area of study (BK$_Z$=9.85X10$^{-1}$ W m$^{-2}$) since the barotropic and baroclinic

conversions and the friction were removing the energy of the system (Fig. 4.34c). The main fonts to the $K_E$ increase were the baroclinic conversion between $A_E$ and $K_E$ ($6.51 \times 10^{-1}$ W m$^{-2}$), a very small contribution of the barotropic conversion of $K_Z$ in $K_E$ ($0.1x \times 10^{-1}$ W m$^{-2}$) and $\Delta R_E = 6.24 \times 10^{-1}$ W m$^{-2}$, although the surrounding environment was acting to remove the energy of the system ($5.71 \times 10^{-1}$ W m$^{-2}$).

In ASL final-phase (Fig. 4.34d), the local change of energy terms had contrary variation compared with ASL initial-phase. In the final-phase period, the local variation of kinetic energy was negative and of the available potential energy was positive. The negative variation of kinetic energy occurred since energy must decrease due to the weakening of the winds during ASL disappearing. $A_Z$ incremented resulted from the environment and the latitudinal thermal differences providing energy to the ASL, although the baroclinic processes were converting $A_Z$ in $K_Z$ (through upward motions of warm air and downward motions of cold air in different latitudes) and $A_Z$ in $A_E$ (due to the wave movements). $A_E$ also increased as function of the surrounding and the thermal differences in the same latitude provided energy to system, but this increment was higher than of $A_Z$ associated with the baroclinic conversion from $A_Z$ to $A_E$ (related to the latitudinal movement of air due to the thermal differences).

Regarding to $K_Z$, in ASL final-phase (Fig. 4.34d), it decreased with time due to the strong loss of energy by friction ($\Delta R_Z = 26.16 \times 10^{-1}$ W m$^{-2}$) and to barotropic conversion of $K_Z$ in $K_E$. This decreases occurred considering that the boundary transport was high and positive ($BK_Z = 20.90 \times 10^{-1}$ W m$^{-2}$) and the baroclinic conversion direction was from $A_Z$ to $K_Z$. It is noted that local variation of $K_E$ also decreased, solely due to strong boundary transport, which was removing $9.02 \times 10^{-1}$ W m$^{-2}$ of the system, since all the other terms were providing energy to ASL.

Comparing the two events, the ASL presented higher values of local tendency of the energy and conversion than the SCL, which was related to higher convective activity and larger velocities in ASL compared to CSL.

## 4.4. KINETIC ENERGY BUDGET

From Lorenz energy it was shown the high values of the kinetic energy. Therefore, in this part of the study the kinetic energy equation in isobaric coordinates (referred as KE_Eq),

described in the section 2.6, was applied to the CSL and ASL events using only Eulerian scheme. Figure 4.35 presents the terms of the volume-integrated of KE_Eq and the Figures 4.36 and 4.37 their vertical profiles.

The principal characteristics of volume-integrated values of the KE_Eq terms (Fig. 4.35) were the following. a) The horizontal flux divergence of kinetic energy (bKE=$\vec{\nabla}_P.k\vec{V}$) decreased with the time and remained negative (convergence) during all CSL life cycle. b) The horizontal flux divergence of kinetic energy was positive and both the local change ($\partial K/\partial t$) as the kinetic energy generation (aKE=$-\vec{V}.\vec{\nabla}_P\emptyset$) increased during the ASL event. Finally, c) since the term of dissipation (dKE= $\vec{V}.\vec{F}$) is obtained as a residual of the KE_Eq (equation 3.34), this term had the same tendency and signal of the bKE in both SL events.
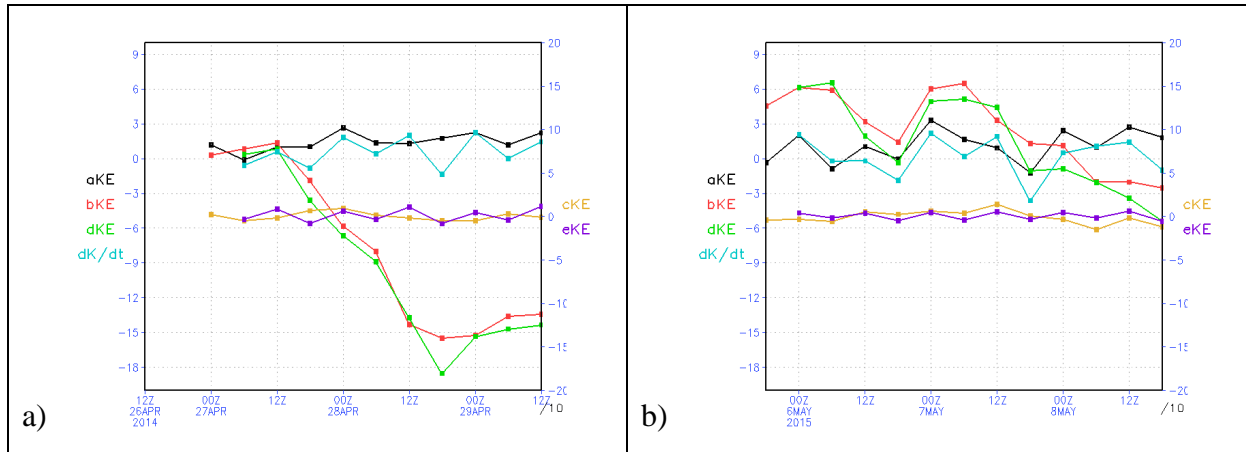


Figure 4.35 - Time series of volume-integrated of KE_Eq terms ($\partial K/\partial t$, aKE=$-\vec{V}.\vec{\nabla}_P\emptyset$, bKE=$\vec{\nabla}_P.k\vec{V}$, cKE=$\partial\omega k/\partial p$, dKE= $\vec{V}.\vec{F}$ and eKE=$k_o\partial p_o/\partial t$ ) for (a) CSL → 27-28 Abril 2014 and (b) ASL → 06-07 May 2015. Values in W m$^{-2}$ x10$^{-1}$ for cKE and eKE and in W m$^{-2}$ for the aKE, bKE, dKE and $\partial K/\partial t$.

The vertical profiles of the aKE, bKE, cKE and $\partial K/\partial t$ terms are presented in Figures 4.36 and 4.37. According the Figure 4.36a the CSL had generation of kinetic energy by cross-contour flow (aKE) at all levels, with a maximum near the level of the jet stream and a secondary maximum near the ground; this is according to Fuelberg and Scoggins (1978) that obtained similar results for a SL on 25 April 1975 occurred in central part of USA. This term (aKE) was the principal source of the increment with time of $\partial K/\partial t$ in all levels, principally from the maximum development time (00:00 UTC 28 April) to the end of CSL (Fig. 4.36d). Otherwise, there was horizontal flux convergence of kinetic energy (bKE<0) in all levels with maximums at 300-400 hPa and 100-200 hPa layers (Fig. 4.36b), which is an important source of kinetic energy in CSL at these levels. The vertical flux divergence of kinetic energy was

small through most of the atmosphere, except at 200-300 hPa layer, when was negative.
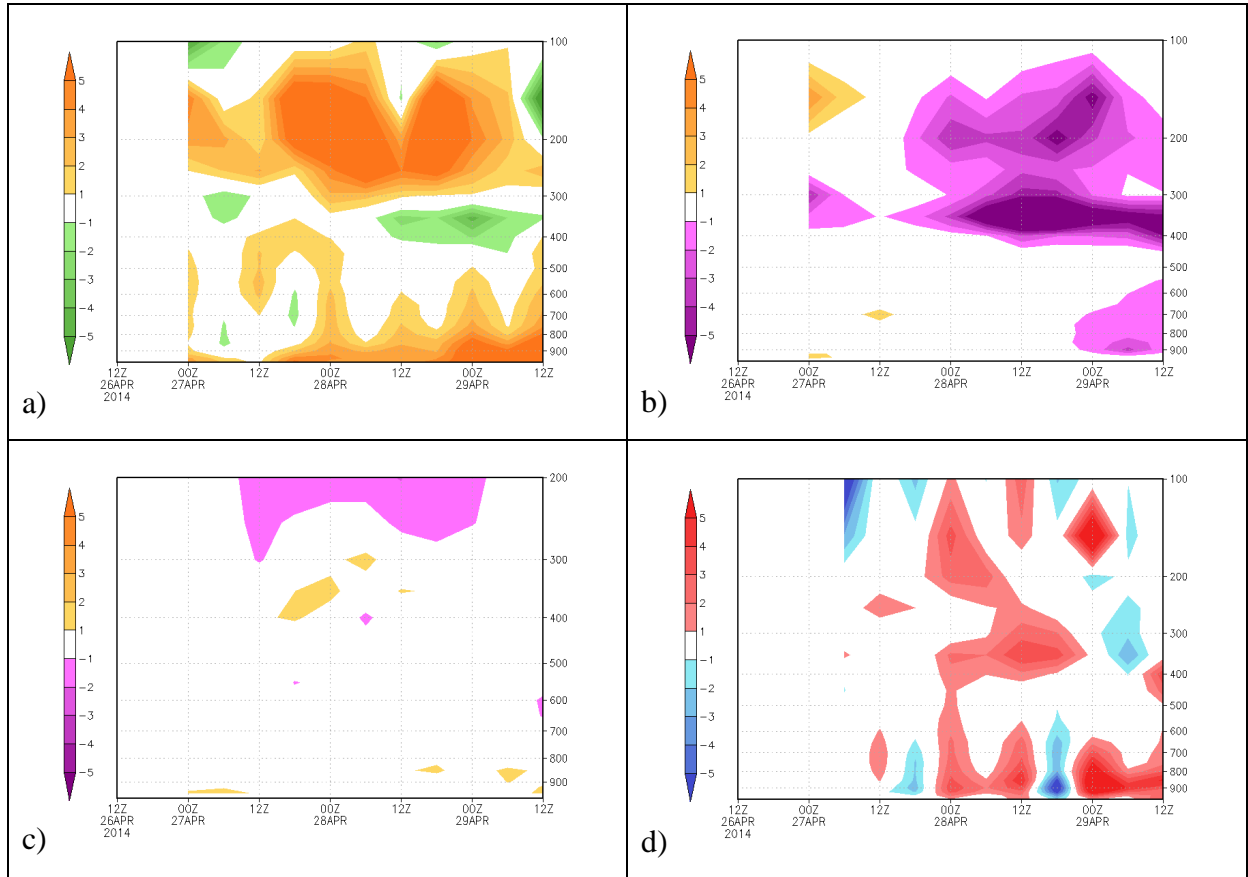


Figure 4.36 - Time series of vertical profiles of (a) aKE$=-\vec{V}.\vec{\nabla}_P\emptyset$, (b) bKE$=\vec{\nabla}_P.k\vec{V}$, (c) cKE$=\partial\omega k/\partial p$, and (d) $\partial K/\partial t$ for CSL→ 27-28 Abril 2014. Values in W m$^{-2}$x10$^{-4}$ for bKE and $\partial K/\partial t$ and in W m$^{-2}$x10$^{-5}$ for aKE and cKE.

During most part of ASL life cycle, generated kinetic energy by cross-contour flow (aKE>0) at all vertical levels, but destructed kinetic energy (aKE<0) at the final of event (12:00 UTC and 18:00 UTC 07 May) (Fig. 4.37a). These values are responsible for the increment of $\partial K/\partial t$ at the beginning of ASL (from 18:00 UTC 06 May to 12:00 UTC 07 May) and the decrease of $\partial K/\partial t$ at the final (Fig. 4.37d). In Figure 4.37b ASL was characterized by flux divergence of kinetic energy at low-levels (below 600 hPa) and at upper levels (100-200 hPa layer), and flux convergence at mid-levels (250-400 hPa) from 00:00 UTC to 12:00 UTC 07 May (maximum development time). This distribution of horizontal flux divergence (bKE) represent the convection in the maximum development of ASL, since the positive value at upper levels indicates energy transported out of the area by horizontal flux divergence. Regarding to vertical flux divergence of kinetic energy, ASL presents flux divergence at low-levels and flux convergence at upper levels (Figs. 4.37c). This indicates upward transport of

kinetic energy from the lower atmosphere to the level of the jet stream (cKE<0 indicates a concentration of energy) by rising air associated with the widespread convection.
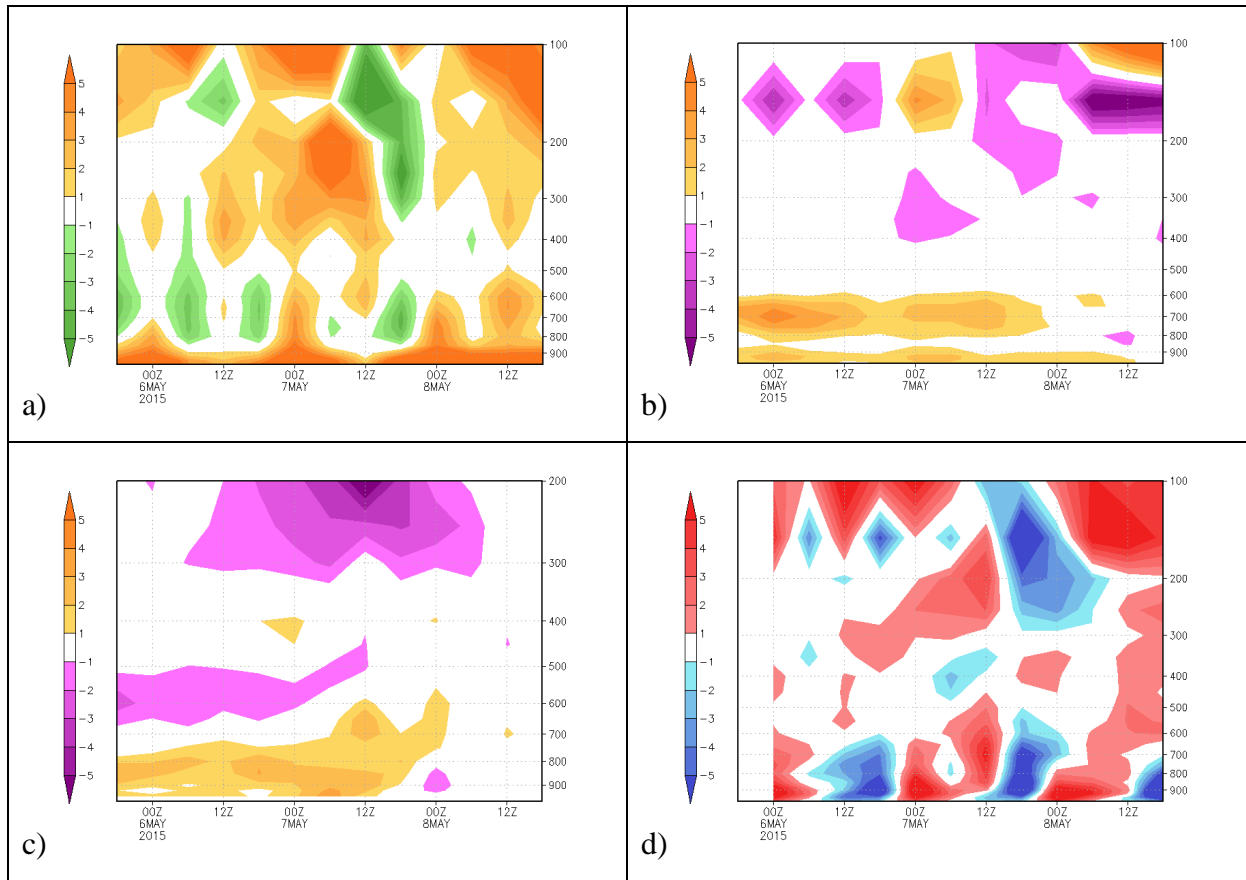


Figure 4.37 - Time series of vertical profiles of (a) aKE$=-\vec{V}.\vec{\nabla}_P\emptyset$, (b) bKE$=\vec{\nabla}_P.k\vec{V}$, (c) cKE$=\partial\omega k/\partial p$, and (d) $\partial K/\partial t$ for ASL$\rightarrow$ 06-07 May 2015. Values in W m$^{-2}$x10$^{-4}$ for bKE and $\partial K/\partial t$ and in W m$^{-2}$x10$^{-5}$ for aKE and cKE.

In general, in volume-integrated calculations, the more important term of the KE_Eq was the horizontal divergence of the flux of kinetic energy (bKE), which was negative for CSL and positive for ASL. In vertical profiles, the term with high values was $\partial K/\partial t$, which had the same tendency of the generation of kinetic energy by cross-contour flow ($-\vec{V}.\vec{\nabla}_P\emptyset$). This later term increased in all troposphere at the time of maximum development of the systems (00:00 UTC to 12:00 UTC), and decreased at the final, principally in ASL, indicating the life cycle of the SLs (generation at beginning and destruction at the last), as found by Fuelberg and Scoggins (1978) in the squall line of 24-25 April 1975.

## 4.5. THERMODYNAMIC BALANCE

According to Dias Pinto (2011) the terms $\Delta G_z$ and $\Delta G_E$ of the Lorenz cycle energy are well represented by the diabatic term of the thermodynamic equation of section 3.2.5. Therefore, to analyze the vertical profile of potential energy generation, the thermodynamic equation in the budget form was applied using the Eulerian approach. In this calculation, the areas were the same presented in Figure 4.18. Figures 4.38 and 4.39 show the vertical profiles of the mean values of the terms of the thermodynamic balance for CSL and ASL events. The local variation with time was obtained using values of 6 hours before, and the term $\frac{Q}{c_p}$ (diabatic heating) was obtained as a residual (Sinclair, 1993).



a)                                          b)
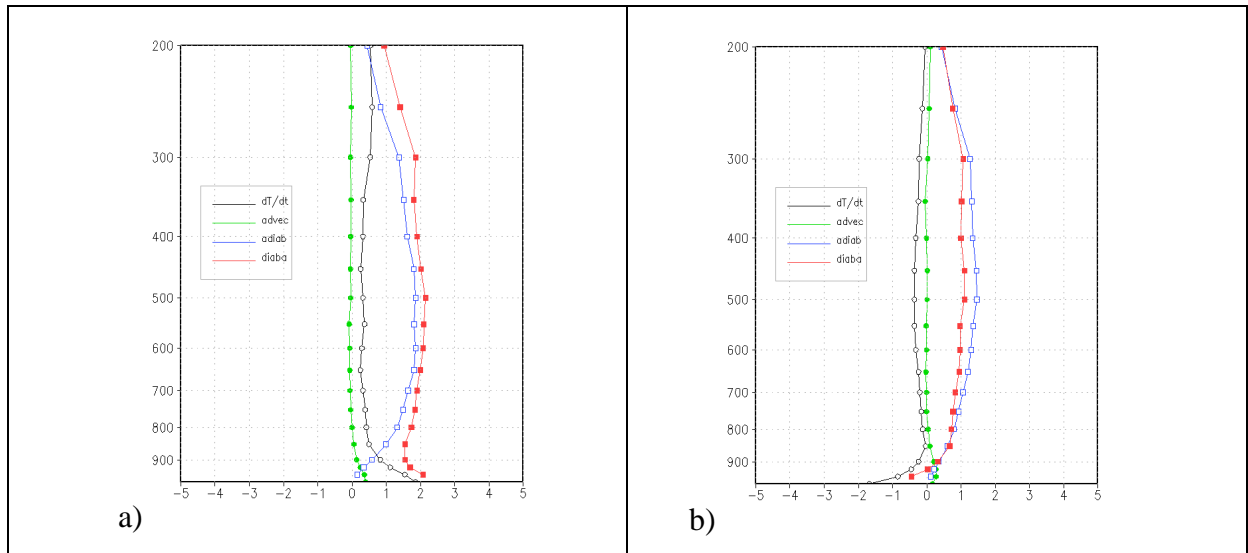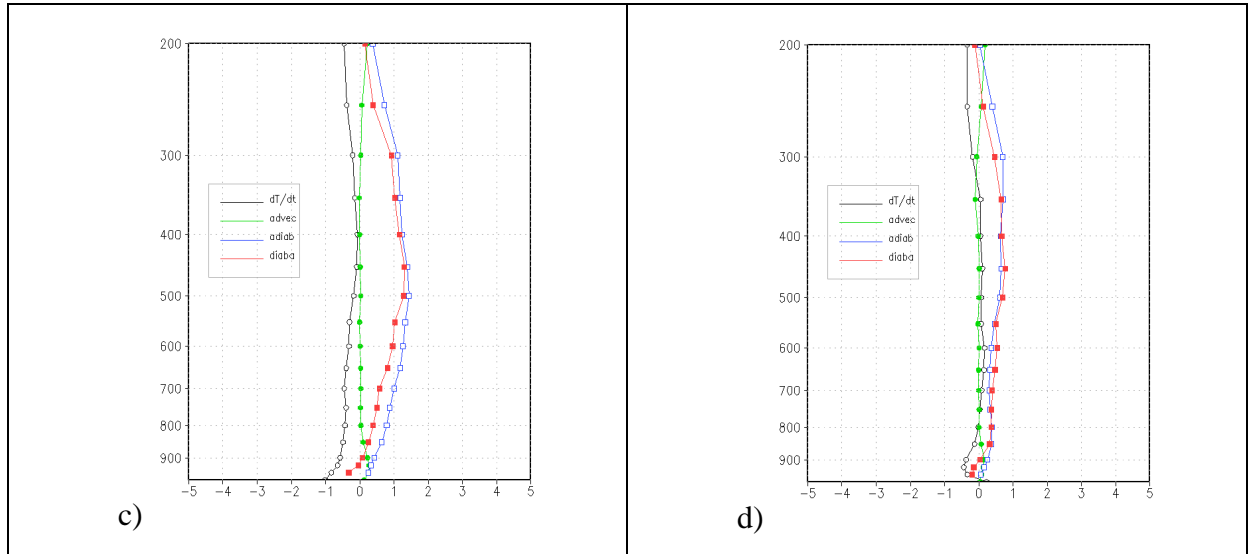
Figure 4.38 - Vertical profiles of the terms of thermodynamic equation [$\frac{\partial T}{\partial t}$, $\left(\frac{u}{a\,cos\varphi}\frac{\partial T}{\partial \lambda} + \frac{v}{a}\frac{\partial T}{\partial \varphi}\right)$ (advec), $\omega\left(\frac{\partial T}{\partial p} - \frac{\alpha}{c_p}\right)$ (adiabatic heating) and $\frac{Q}{c_p}$ (diabatic heating)] for CSL at: a) 18:00 UTC 27 April, b) 00:00 UTC, c) 06:00 UTC and d) 12:00 UTC 28 April 2014. Values in °C/6h.

From 18:00 UTC 27 April until 06:00 UTC 28 April, for CSL the leading terms were diabatic and adiabatic heating terms with maximum value of 2°C/6h at 18:00 UTC 27 April 2014 near the 500 hPa level (Figs. 4.38a – 4.38c). The other terms were near the zero and only $\frac{\partial T}{\partial t}$ and diabatic heating presented diurnal cycle near the surface.

For the ASL (Fig. 4.39), the diabatic and adiabatic heating were also the leading terms, with maximum values of 3.5°C/6h between the 400 and 500 hPa at 06:00 UTC 07 May 2015, which is the time of maximum development of ASL (Fig. 4.39b). The diurnal cycle of the local variation of temperature ($\frac{\partial T}{\partial t}$) and diabatic heating was also observed in ASL event (Fig. 4.39a-d).
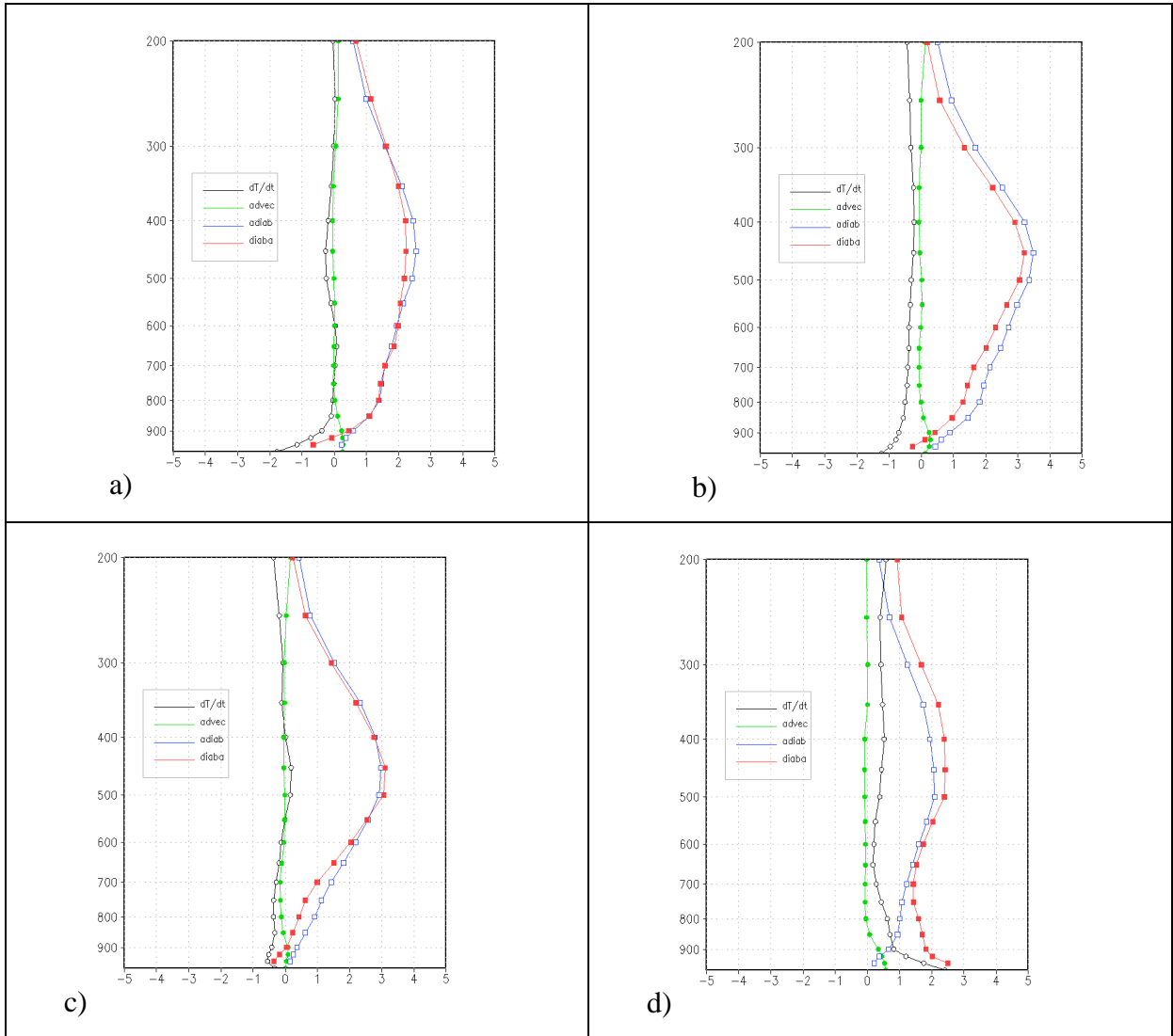
Figure 4.39 - Vertical profiles of the terms of Thermodynamic Equation $[\frac{\partial T}{\partial t}, \left(\frac{u}{a\,cos\varphi}\frac{\partial T}{\partial \lambda} + \frac{v}{a}\frac{\partial T}{\partial \varphi}\right)$ (advec), $\omega\left(\frac{\partial T}{\partial p} - \frac{\alpha}{c_p}\right)$ (adiabatic heating) and $\frac{Q}{c_p}$ (diabatic heating)] for ASL at: a) 00:00 UTC, b) 06:00 UTC, c) 12:00 UTC and d) 18:00 UTC 07 May 2015. Values in °C/6h.

Comparing the two SL events, diabatic and adiabatic heating presented higher values in ASL than in CSL and the peak of heating was found at mid-levels in both SLs. This is according to Greco et al. (1994) who found the maximum heating in 500–550 hPa layer for other Amazon SL event of May 1987.

# 5. CHAPTER 5: CONCLUSIONS

This work analyzed the energy related to the propagation of Amazon squall lines (SL) using the Lorenz Energy Cycle (LEC). To characterize the energy of the environment during SLs with small and long propagation distance, the LEC was applied in two SL events. The first event was named Coastal Squall Line (CSL) and it formed on the northeast coast of South America and presented small inland propagation (less than 10° to the west from its starting point), and the second, named Amazonian Squall Line (ASL), had a longer inland propagation over the Amazon basin (advanced more than 10° westward). Therefore, it was possible to characterize the energetic of the SLs according to their inland propagation. The synoptic analysis of these two events were performed to understand the environmental conditions during SLs occurrence. The kinetic energy equation and the thermodynamic balance were also applied to every SL event.

For the period between April and August 2014 - 2015, 21 SL events were identified, being 15 classified as CSL and 6 as ASL. The mean features of these CSLs (ASLs) were 12 (18) m s$^{-1}$ of propagation speed, 15 (23) hours of lifetime, 626 (1393) km of inland propagation, and in its maximum development 1450 (1975) km of length and 174 (249) km of width. Therefore, the ASLs were faster, more lasting, propagating larger distances, wider and longer than the CSLs. The majority of CSLs and ASLs started at early afternoon (15-18:00 UTC). For both SLs, as time progressed (from April to August), they tend to form northward, following the north-south migration of the ITCZ.

The synoptic analysis showed at upper levels more intense easterly winds near the Equator in ASL than in CSL, associated with the presence of two anticyclonic systems, one in each hemisphere. The relationship between upper-levels divergence and low-levels convergence was higher in ASL than in CSL, since in ASL the convergence and the wind confluence at 850 hPa is more intense than in CSL, while the divergence at upper levels is similar in both events. At mid-levels, the occurrence of both SLs was related to the presence of an inverted trough, which accompanies the event displacement. At low-levels, during the CSL occurrence, a cold system approached from the south and imposed southerly winds that converged with the northeasterly winds, while in ASL only easterly winds were observed. The moisture convergence flux at 850 hPa and the vertical wind speed shear in 700-850 hPa layer were higher in ASL than in CSL. Vertical wind profiles in the points of maximum

convection showed predominance of easterly winds in all troposphere in ASL, with two maxima of intensity one at upper levels and the other at low-levels, forming a duct for ASL propagation. In addition, the low-level jet at 700 hPa was more intense in ASL than in CSL. The vertical wind shear was directional at upper levels during the CSL occurrence, which obstructed the CSL westward displacement. During the ASL occurrence, wind speed shear existed at low-levels favoring the regeneration of new convective cells and the ASL displacement over Amazon basin.

Regarding the LEC terms, with slight differences between quasi-Lagrangian and Eulerian approaches, the zonal kinetic energy ($K_Z$) presented the highest values in both SL events. The vertical profile showed the maximums of $K_Z$ occurring in two layers: 100-300 hPa and 600-1000 hPa. The eddy kinetic energetic ($K_E$) was the second term of importance, with higher values in ASL than in CSL, and it grew abruptly during the ASL, but not in CSL. The maximum values of $K_E$ were located in the entire vertical troposphere in ASL but only above 500 hPa in CSL. Since the horizontal gradients of temperature in the Amazon basin are very small, the zonal and eddy available potential energies ($A_Z$ and $A_E$) were also small, presenting only diurnal variations (maxima at 18:00 UTC) below 900 hPa as function of their temperature dependence. About the energy conversion terms, in both approaches, the baroclinic terms $C_E$ ($A_E$, $K_E$) and $C_Z$ ($K_Z$, $A_Z$) increased when SLs reached the maximum development. This increment was more abrupt in ASL than in CSL, reaching maximum values in the 200-500 hPa layer. For both events, the baroclinic term $C_A$ ($A_Z$, $A_E$) was one order of magnitude smaller than the other terms, since the $A_Z$ and $A_E$ values were small. Although the barotropic term $C_K$ ($K_E$, $K_Z$) was almost constant with time it presented the same order of magnitude as the $C_E$ and $C_Z$, highlighting the importance of barotropic instability in the development of Amazon SLs. The boundary energy transports varied between the quasi-Lagrangian and the Eulerian scheme, since changing the edges the flow energy also varies by those edges. The boundary zonal kinetic and eddy kinetic energy transports ($BK_Z$ and $BK_E$, respectively) had the highest values in both SLs, and in quasi-Lagrangian scheme, they increased only at the end of the ASL. The vertical profiles of $BK_Z$ and $BK_E$ in both SLs showed, predominantly, positive values from 100 hPa to 350 hPa, indicating flux of kinetic energy from the surroundings into the SL area, and negative values from 350 to 900 hPa, indicating kinetic energy leaving the SL area.

During initial and final stages of CSL, LEC showed generation of available potential energy by thermal gradient and transport from the environment to the system area, which was

converted in kinetic energy by baroclinic process. The barotropic conversion of zonal in eddy kinetic energy were processes where the perturbation extracted kinetic energy from the zonal flow. At initial-phase, the environment provided zonal kinetic energy to the system and the system transferred eddy kinetic energy to its environment, while the opposite process happened at final-phase.

During ASL initial-phase, although the thermal variation did not allow generation of available potential energy, the environment transferred eddy available potential energy to the system that was converted to eddy kinetic energy by baroclinic conversion of convective motions in the same latitude (upward motions of warm air and downward motions of cold air). Then part of the eddy kinetic energy was transported to its environment. At ASL final-phase, there was generation and transport of available potential energy from the environment to the area that was converted in kinetic energy by baroclinic processes. The zonal friction removed this kinetic energy from the system and transferred to the environment as eddy flux. All the terms of LEC in ASL were higher than in CSL, representing the large activity of the convective processes in ASL.

The horizontal flux convergence (divergence) of kinetic energy in CSL (ASL), as well as the vertical flux convergence (divergence) of kinetic energy at upper levels (low-levels) higher in ASL than in CSL, were the most representative results of the application of the kinetic energy equation in the SL events. These results represented the higher convection in ASL than in CSL, since upward transport of kinetic energy from the lower atmosphere to the level of the jet stream by rising air associated with convection generates horizontal flux divergence and vertical flux convergence at upper levels, and the opposite at low-levels. The thermodynamic balance resulted in a higher diabatic and adiabatic heating in ASL than in CSL, with peaks of heating at mid-levels in both SLs.

Based in these analysis, ASL presents an abrupt variation of eddy kinetic energy (KE) and baroclinic conversion from available potential energy into kinetic energy during its maximum development. This does not occur for CSL. Therefore, the values of conversions and local variations of energy are higher in ASL than in CSL. These characteristics, in addition to the specific synoptic conditions for each SL (mainly, maximum wind at upper levels, larger convergence of winds and moisture flux, and higher vertical wind speed shear at low-levels in ASL than in CSL) would help to forecast with greater accuracy a propagating SL.

# 6. CHAPTER 6: SUGGESTIONS

Within the present work some questions emerged that were left unanswered. The first one concerns to the ENSO influence in the energy of Amazon SLs, which it is suggested to increase the period of analysis. Possibly working from 2002 to the present day, since infrared satellite imagery is available on the CPTEC website for this period. The second, is the use of different data sets. In the initial phase of this study, the comparisons of ERA-Interim and GFS analysis  showed large differences in the energy of the events, which was related to each model resolution. As such, it would be recommendable to find how the energy of SLs varies using mesoescale models since resolution is an important factor in the value of energy as found by Fuelberg and Scogging (1978) in a SL.

# 7. REFERENCES

7.1.   American Meteorology Society. Glossary of Meteorology: Squall Line. [Internet]. [Cited 2016 November 17]. Available at: http://glossary.ametsoc.org/wiki/Squall_line

7.2.   ALCÂNTARA C. Linha de Instabilidade da Amazônia: Estudo de caso e importância das características do perfil do vento na sua formação e desenvolvimento. Universidade Federal de Campina Grande. Ciência e Natura. 2011; 33 (2): 197-226.

7.3.   ALCÂNTARA C., PEREIRA DE SOUZA E., SILVA DIAS M.A.F. and BIAZETO B. Influência dos Jatos em Médios e Baixos Níveis nos processos de nuvem: Estudo Numérico de uma Linha de Instabilidade Amazônica. Revista Brasileira de Meteorologia. 2014; 29 (1): 29-46.

7.4.   ALCÂNTARA C., SILVA DIAS M.A.F., PEREIRA DE SOUZA, E. and COHEN J.C.P. Verification of the role of the low level jets in Amazon Squall Lines.  Atmospheric Research. 2011; 100: 36-44.

7.5.   ASNANI G.C. Tropical Meteorology. Volume 1. Pashan, Pune – India: Noble Printers Pvt, Ltd. Indian Institute of Tropical Meteorology; 1993. Chap 2, Climatology of the Tropics; p.157 – 166.

7.6.   _____. Tropical Meteorology. Volume 1. Pune – India: Praveen Printing Press. Indian Institute of Tropical Meteorology; 2005. Chap 2 (8), Climatology of the Tropics: Energy; p. 2-166 – 2-186.

7.7.   _____. Tropical Meteorology. Volume 2. Pune – India: Praveen Printers Pvt, Ltd. Indian Institute of Tropical Meteorology; 2005. Chap 10 (3), Meso-scale Systems of the Tropics: Squall - Lines; p. 10.44 – 10.71.

7.8.   BARRY R.G. and CHORLEY R.J. Atmosphere, Weather and Climate. Eight Edition. London. Routledge; 2003. Chap 3, Solar Radiation and the Global Energy Budget; p. 59.

7.9.   BERRISFORD P., DEE D., POLI P., FIELDING K., FUENTES M., KALBERG P., KOBAYASHI S., UPPALA S. and SIMMONS A. Era Report Series: The ERA-Interim

archive. Version 2.0. p. 1-27.

7.10. BRAUN S.A. and HOUZE R.A. Jr. The Heat Budget of a Midlatitude Squall Line and ImpCASLtions for Potential Vorticity Production. Journal of the Atmospheric Sciences. 1996 May; 53 (9): 1217-1240.

7.11. BRENNAN F.E. and VINCENT D.G. Zonal and Eddy Components of the Synoptic-Scale Energy Budget during Intensification of Hurricane Carmen (1974). Monthly Weather Review. 1980 Jul; 108(7): 954-965.

7.12. CARLSON T.N. Mid-Latitude Weather Systems. Boston, EEUU. The American Meteorological Society, 1998. Chap 5, Quasi-geostrophic energetics: The energy cycle; eddy and zonal energy exchanges, p. 120-126.

7.13. CAVALCANTI I.F. de A. Um estudo sobre interações entre sistemas de circulação de escala sinótica e circulações locais. Dissertação de Mestrado em Meteorologia. INPE. São José dos Campos: 1982. 139 p.

7.14. CAVALCANTI I.F. de A., FERREIRA N.J., Da SILVA M.G.A.J., SILVA DIAS M.A.F. Tempo e Clima no Brasil. São Paulo, Brasil. Oficina de Textos; 2009. Chap 5, Linhas de Instabilidade na costa N-NE da América do Sul, p. 75-93.

7.15. COHEN J.C.P. Um estudo observacional de linhas de instabilidade na Amazônia. Dissertação de Mestrado em Meteorologia. INPE. São José dos Campos: 1989. 160 p.

7.16. COHEN J.C.P., GANDU A.W., CHIBA C.Y.B., BRAGA R.H.M. Linhas de instabilidade formadas ao longo da costa Atlântica e no interior do continente: Estudo de casos com o modelo de alta resolução. XIII Congresso Brasileiro de Meteorologia. 2004, Fortaleza (CE). Anais 2004.

7.17. COHEN J.C.P., SILVA DIAS M.A.F., NOBRE C. Environmental conditions associated with Amazonian squall lines: A case study. Monthly Weather Review. 1995 Nov; 123(11): 3163-3174.

7.18. DA SILVA L.G. and SATYAMURTY P. Evolution of the Lorenz Energy Cycle in the

Intertropical Convergence Zone in the South American Sector of the Atlantic Ocean. Journal of Climate. 2013 May; 26: 3466-3481.


7.19. DIAS PINTO J. Estudo da Estrutura e Energia dos Distúrbios de Escala Sinótica na Costa Leste da América do Sul. Dissertação de Mestrado em Meteorologia. Universidade de São Paulo. São Paulo: 2010. 106 p.


7.20. DIAS PINTO J and DA ROCHA R. The energy cycle and structural evolution of cyclones over southeastern South America in three cases studies. Journal of Geophysical Research. 2011 Jul; 116: 1 – 17. D141112.


7.21. FUELBERG H.E. and SCOGGINS J.R. Kinetic Energy Budgets During the Life Cycle of Intense Convective Activity. Monthly Weather Review. 1978 May; 106: 637-653.


7.22. FUJITA T. Results of Detailed Synoptic Studies of Squall Lines. Tellus VII. 1955; 4: 405-436.


7.23. GARSTANG M., MASSIE H.L.Jr., HALVERSON J., GRECO S. and SCALA J. Amazon Coastal Squall Lines. Part I: Structure and Kinematics.  Monthly Weather Review. 1994 Apr; 122: 608-622.


7.24. GRECO S., SCALA J., HALVERSON J., MASSIE H.L.Jr., TAO W-K and GARSTANG M. Amazon Coastal Squall Lines. Part II: Heat and Moisture Transport. Monthly Weather Review. 1994 Apr; 122: 623-635.


7.25. GRECO S., SWAP R., GARSTANG M., ULANSKI S., SHIPAM M., HARRIS R.C., TALBOT R., ANDREAE M.O. and ARTAXO P. Rainfall and surface kinematic conditions over central Amazonia during ABLE 2B. J. Geophys. Res. 1990; 95:17001-17017.


7.26. HOLTON J.R. An Introduction to Dynamic Meteorology. Fourth Edition. Seattle, Washington, USA. Department of Atmospheric Sciences, University of Washington. Elsevier Academic Press; 2004. Chap 2, Basic Conservation Laws: The Thermodynamic Energy Equation and Thermodynamics of the Dry Atmosphere, p. 46-54.


7.27. HOUZE R.A. Jr. Structure and Dynamics of a Tropical Squall-Line System. Monthly

Weather Review. 1977 Dec; 105: 1540-1567.


7.28. HSIEH J, COOK K. A study of the Energetics of African Easterly Waves Using a Regional Climate Model. Journal of the Atmospheric Sciences. 2007 Feb; 64: 421-440.


7.29. KOUSKY VE. Diurnal rainfall variation in the northeast Brazil. Monthly Weather Review. 1980 Apr; 108: 488-498.


7.30. KUNG E.C. Kinetic Energy Generation and Dissipation in the Large-Scale Atmospheric Circulation. Monthly Weather Review. 1966 Feb; 94 (2): 67-82.


7.31. LEMONE M.A., ZIPSER E.J. and TRIER S.B. The Role of Environmental Shear and Thermodynamic Conditions in Determining the Structure and Evolution of Mesoscale Convective Systems during TOGA COARE. J Atmospheric Sciences. 1998 Dec; 55: 3493-3518.


7.32. LORENZ E.N. Available potential energy and the maintenance of the general circulation. Tellus VII. 1955; 2: 157-167.


7.33. LORENZ E.N. The Nature and Theory of the General Circulation of the Atmosphere. World Meteorological Organization; 1967. Chap 5, The Energetics of the Atmosphere; p.97 – 113.


7.34. _____. The Nature and Theory of the General Circulation of the Atmosphere. WMO. 1967. 161 p.


7.35. MARKOWSKI P. and RICHARDSON Y. Mesoescale Meteorology in Midlatitudes. Penn State University, University Park, USA: Wiley-Blackwell; 2010. Chap 9, Mesoescale Convective Systems; p. 245-260.


7.36. MICHAELIDES S.C. Limited Area Energetics of Genoa Cyclogenesis. Monthly Weather Review. 1987 Jan; 115: 13-26.


7.37. MICHAELIDES S.C., PREZERAKOS N.G and FLOCAS H.A. Quasi-Lagrangian

energetics of an intense Mediterranean cyclone. Q. J. R. Meteorol. Soc. 1999; 125: 139-168.

7.38. MUENCH HS. On the dynamics of the wintertime stratosphere circulation. J Atmospheric Sciences. 1965 Jul; 22: 349-360.

7.39. National Centers for Environmental Information. NOAA. Home: Data Access: Model: Datasets: Global Forecast System (GFS) [Internet]. [Cited 2016 October 25]. Available at: https://www.ncdc.noaa.gov/data-access/model-data/model-datasets/global-forcast-system-gfs.

7.40. NORQUIST DC, RECKEER EE, REED RJ. The Energetics of African Wave Disturbances as Observed During Phase III of GATE. Monthly Weather Review. 1965 Mar; 105: 334-342.

7.41. OGURA Y. and LIOU M. The Structure of a Midlatitude Squall Line: A Case Study. Journal of the Atmospheric Sciences. 1980 Mar; 37: 553-567.

7.42. OLIVEIRA G.B., ALCÂNTARA C.R. and DE SOUZA E.P. Caracterização de perfis de vento no ambiente de formação das linhas de instabilidade amazônicas. Ciência e Natura. Revista do Centro de Ciências Naturais e Exatas – UFSM. 2016 Jan; 38 (1): 393-403.

7.43. OORT A.H. On Estimates of the Atmospheric Energy Cycle. Monthly Weather Review. 1964 Nov; 92 (11): 483-493.

7.44. PARKER M. D. and JOHNSON R. H. Organizational Models of Midlatitude Mesoescale Convective Systems. Monthly Weather Review. 2000 Oct; 128: 3413-3435.

7.45. RAMIREZ G.E., SILVA DIAS P.L., VEIGA J.A., CAMAYO R. and DOS SANTOS A. Multivariate Analysis of the Energy Cycle of the South American rainy season. International Journal of Climatology. 2009 Feb; 29: 2256-2269.

7.46. RICKENBACH T.M. Nocturnal Cloud Systems and the Diurnal Variation of Clouds and Rainfall in Southwestern Amazonia. Monthly Weather Review. 2004 May; 132: 1201-1219.

7.47. ROTUNNO R., KLEMP J. B. and WEISMAN M. L. A Theory for Strong, Long-lived Squall Lines. Journal of the Atmospheric Sciences. 1988 Feb; 45 (3): 463-485.


7.48. SINCLAIR M.P. Synoptic-Scale Diagnosis of the Extratropical Transition of a Southwest Pacific Tropical Cyclone. Monthly Weather Review. 1993 Apr; 121: 941-960.


7.49. SMITH P.J. On the contribution of a limited region to the global energy budget. Tellus XXI; 1969 (2): 202-207.


7.50. SMITH P.J. A Note on Energy Conversions in Open Atmospheric Systems. Journal of the Atmospheric Sciences. 1970 May; 27: 518-521.


7.51. THORPE A.J., MILLER M.J. and MONCRIEFF M.W. Two-dimensional convection in non-constant shear: a model of mid -latitude squall lines. Quarterly Journal of the Royal Meteorological Society. 1982 Oct; 108: 739-762.


7.52. VEIGA J, PEZZA A, AMBRIZZI T, RAO B, FRANCHITO S, YOSHIDA M. The Energy Cycle Associated to the Pacific Walker Circulation and Its Relationship to ENSO. Atmospheric and Climate Sciences. Scientific Research. 2013 Oct; 3: 627-642.**APPENDIX**


7.53. ZIPSER E.J. Mesoescale and Convective-Scale Downdrafts as Distinct Components of Squall-Line Structure. Monthly Weather Review. 1977 Dec; 105: 1568-1589.

# 8. APPENDIX

Tables 8.1-8.3 presents the average in a quasi-Lagrangian scheme of the LEC terms every 6 hours of the 4 ASL and the 5 CSL obtained from GFS analysis.

Table 8.1 – Averages of LEC energies at every 6 hours. Values in J m$^{-2}$.

| TIME UTC | $K_Z$ x $10^5$ | | $K_E$ x $10^4$ | | $A_Z$ x $10^3$ | | $A_E$ x $10^3$ | |
|---|---|---|---|---|---|---|---|---|
| | CSL | ASL | CSL | ASL | CSL | ASL | CSL | ASL |
| 00:00 | 3.00 | 3.09 | 2.55 | 4.55 | 5.51 | 4.74 | 8.63 | 15.21 |
| 06:00 | 3.01 | 2.71 | 3.16 | 5.53 | 4.61 | 4.54 | 7.82 | 16.11 |
| 12:00 | 2.39 | 2.84 | 3.69 | 5.62 | 3.72 | 4.68 | 10.67 | 13.21 |
| 18:00 | 2.69 | 2.60 | 2.49 | 4.31 | 16.54 | 27.10 | 37.93 | 33.57 |

From Table 8.1, it is noted that $K_Z$ values are similar (close to 3x105 J m$^{-2}$) for the two SL types and it also does not present a diurnal cycle. In contrast, $K_E$ had higher values in ASL than in CSL, as shown in Fig. 4.19 and these values are higher at 06:00 and 12:00 UTC, which are the hours near to the time of maximum SLs development. $A_Z$ and $A_E$ showed maximum values at 18:00 UTC as result of the temperature increasing along the day, coinciding with what was observed in Fig. 4.19. Comparatively $A_E$ presented larger values in ASL than in CSL at 00:00 UTC, 06:00 UTC and 12:00 UTC.

Table 8.2 – Averages of energy conversions at every 6 hours. Values in W m$^{-2}$.

| TIME UTC | $C(A_Z,A_E)$x$10^{-3}$ | | $C(A_E,K_E)$x$10^{-2}$ | | $C(K_E,K_Z)$x$10^{-3}$ | | $C(K_Z,A_Z)$x$10^{-2}$ | |
|---|---|---|---|---|---|---|---|---|
| | CSL | ASL | CSL | ASL | CSL | ASL | CSL | ASL |
| 00:00 | -6.33 | -8.93 | 13.82 | 16.13 | -6.86 | 18.66 | -12.95 | 8.25 |
| 06:00 | 10.61 | -7.21 | 25.50 | 41.36 | -66.69 | -14.17 | 0.17 | 19.51 |
| 12:00 | -24.53 | -14.97 | -1.33 | -1.73 | -51.94 | 1.99 | 1.20 | -11.85 |
| 18:00 | 41.66 | 0.42 | -0.68 | 30.24 | -50.75 | -4.97 | -6.67 | -13.34 |

The high values of $K_E$ in Table 8.1 are explained by the conversion of $A_E$ in $K_E$ in both types of events, with higher values in ASL than in CSL (Table 8.2). The conversion of $K_E$ in $K_Z$ was negative in CSL, which means that $K_E$ existed at the expenses of $K_Z$ at all times. In ASL, that direction of the conversion was manifested at 06:00 and 18:00 UTC, while in the other times $K_Z$ existed at the expenses of $K_E$ (positive values). The other conversion terms did not show a clear behavior in any event, which also was observed in Figure 4.24.

Table 8.3 – Averaged of boundary energy transports at every 6 hours. Values in W m$^{-2}$.

| TIME | $BK_Z$ | | $BK_E$ x $10^{-1}$ | | $BA_Z$ x $10^{-2}$ | | $BA_E$ x $10^{-2}$ | |
|------|------|------|------|------|------|------|------|------|
| UTC | CSL | ASL | CSL | ASL | CSL | ASL | CSL | ASL |
| 00:00 | 0.10 | 2.27 | 1.08 | 1.16 | 24.60 | 17.67 | -0.32 | 3.71 |
| 06:00 | -1.26 | 3.53 | 0.45 | 2.84 | 7.99 | 8.56 | 5.72 | -12.12 |
| 12:00 | 1.41 | 3.37 | -5.03 | 7.22 | 6.52 | 5.70 | 2.26 | -16.04 |
| 18:00 | -0.48 | 0.37 | -2.20 | -0.77 | 66.24 | 125.26 | 126.73 | 52.87 |

The boundary $K_Z$ transport was greater and always positive in ASL than in CSL, which means that in ASL the area of study received $K_Z$ from the surroundings, while in CSL at 06:00 and 18:00 UTC the transport of $K_Z$ was from the area to the surroundings (negative values in Table 8.3). $BK_E$ presented a behavior similar to $BK_Z$ with values higher in ASL than in CSL. In ASL, from 00:00 to 12:00 UTC, $K_E$ was transferred from the surroundings to the system area (positive values) and at 18:00 UTC the direction was opposite. In CSL, at 00:00 and 06:00 UTC $K_E$ was transported from the surroundings to the interior of the area of study, but at 12:00 and 18:00 UTC the direction of transport was reversed.

Like $A_Z$ and $A_E$, the boundary transport of these energy terms present similar trends in ASL and CSL, only show higher values at 18:00 UTC associated with their temperature dependence.